Fall 2014

Electronic, optical, mechanical and thermoelectric properties of graphene

Sarang Vilas Muley
New Jersey Institute of Technology

ABSTRACT

ELECTRONIC, OPTICAL, MECHANICAL AND THERMOELECTRIC PROPERTIES OF GRAPHENE

by

Sarang Vilas Muley

Graphene, a two-dimensional allotrope of graphite with sp^2 bonded carbon atoms, is arranged in honeycomb structure. Its quasi one-dimensional form is graphene nanoribbon (GNR). Graphene related materials have been found to display excellent electronic, chemical, mechanical properties along with uniquely high thermal conductivity, electrical conductivity and high optical transparency. With excellent electrical characteristics such as high carrier transport properties, quantum Hall effect at room temperature and unusual magnetic properties, graphene has applications in optoelectronic devices.

Electronically, graphene is a zero bandgap semiconductor making it essential to tailor its structure for obtaining specific band structure. Narrow GNRs are known to open up bandgap and found to exhibit variations for different chiralities i.e., armchair and zigzag. Doping graphene, with p- or n- type elements, is shown to exhibit bandgap in contrast to pristine graphene.

In this study, optical properties including dielectric functions, absorption coefficient, transmittance, and reflectance, as a function of wavelength and incident energy, are studied. Refractive index and extinction coefficient of pristine graphene are presented. A key optical property in the infrared region, emissivity, is studied as a function of wavelength for various multilayered configurations having graphene as one of the constituent layers. Application of such a structure is in the fabrication of a Hot

Electron Bolometer (a sensor that operates on the basis of temperature-dependent electrical resistance).

Graphene is found to have very high elastic modulus and intrinsic strength. Nanoindentation of graphene sheet is simulated to study the force versus displacement curves. Effects of variation of diameter of indenter, speed of indentation and number of layers of graphene on the mechanical properties are presented.

Shrinking size of electronic devices has led to an acute need for thermal management. This prompted the study of thermoelectric (TE) effects in graphene based systems. TE devices are finding applications in power generation and solid state refrigeration. This study involves analyzing the electronic, thermal and electrical transport properties of these systems. Electronic thermal conductivity, of graphene based systems (κ_e), is found to be negligible as compared to its phonon-induced lattice thermal conduction (κ_p). Variations in κ_p of graphene and GNRs are evaluated as a function of their width and length of their edges, chiralities, temperature, and number of layers. The interdependence of transport parameters, i.e., electrical conductivity (σ), thermoelectric power (TEP) or Seebeck coefficient (S), and κ of graphene are discussed. The thermoelectric performance of these materials is determined mainly by a parameter called Figure-of-Merit. Effective methods to optimize the value of Figure-of-Merit are explored. Reducing the thermal conductivity and increasing the power factor of these systems are found to improve the Figure-of-Merit significantly. This involves correlation of structure and transport properties. Effects of doping on σ, κ and Hall coefficient are discussed.

ELECTRONIC, OPTICAL, MECHANICAL AND THERMOELECTRIC PROPERTIES OF GRAPHENE

by
Sarang Vilas Muley

A Dissertation
Submitted to the Faculty of
New Jersey Institute of Technology
in Partial Fulfillment of the Requirements for the Degree of
Doctor of Philosophy in Materials Science and Engineering

Interdisciplinary Program in Materials Science and Engineering

January 2015

APPROVAL PAGE

ELECTRONIC, OPTICAL, MECHANICAL AND THERMOELECTRIC PROPERTIES OF GRAPHENE

Sarang Vilas Muley

Dr. Nuggehalli M. Ravindra, Dissertation Advisor — Date
Professor and Director of Materials Science and Engineering Program, NJIT

Dr. Ken Ahn, Committee Member — Date
Associate Professor of Physics, NJIT

Dr. Michael Booty, Committee Member — Date
Professor of Mathematical Sciences, NJIT

Dr. Michael Jaffe, Committee Member — Date
Research Professor of Biomedical Engineering and Chemistry, NJIT

Dr. Anthony T. Fiory, Committee Member — Date
Consultant (Formerly Research Professor), Department of Physics, NJIT

BIOGRAPHICAL SKETCH

Author: Sarang Vilas Muley

Degree: Doctor of Philosophy

Date: January 2015

Undergraduate and Graduate Education:

- Doctor of Philosophy in Materials Science & Engineering,
  New Jersey Institute of Technology, Newark, NJ, 2015

- Master of Technology in Metallurgical & Materials Engineering,
  Indian Institute of Technology, Kharagpur, W.B., India, 2008

- Bachelor of Engineering in Metallurgical & Materials Engineering,
  The Maharaja Sayajirao University of Baroda, Vadodara, Gujarat, India, 2006

Major: Materials Science and Engineering

Presentations and Publications:

Sarang Muley & N. M. Ravindra, Effect of doping and chirality on Electronic, Optical and Thermoelectric properties of Graphene nanosheets and nanoribbons, to be submitted, 2014.

Sarang Muley & N. M. Ravindra, Electronic, Optical and Thermoelectric properties of pristine and doped graphene nanosheets, nanoribbons and graphene oxide, Materials Science & Technology (MS & T) 2014, Pittsburgh, PA, USA.

Sarang Muley & N. M. Ravindra, Graphene – Environmental and Sensor Applications In Nanotechnology for water treatment and purification (A. Hu and A. Apblett eds.), Lecture Notes in Nanoscale Science and Technology 22, Springer International Publishing Switzerland, 159-224, 2014.

Sarang Muley & N. M. Ravindra, Emissivity of Electronic Materials, Coatings & Structures, Journal of Materials 66(4), pp. 616-636, 2014.

Sarang Muley & N. M. Ravindra, Study of Thermoelectric, Electronic and Optical Properties of Suspended Graphene Nanosheets and Nanoribbons, TMS 2014 Annual Meeting & Exhibition, San Diego.

Sarang Muley & N. M. Ravindra, Modeling and Simulation of Optical Properties of Carbon Related Materials and Structures, Materials Science & Technology (MS & T) 2013, Montreal QC, Canada.

I would like to dedicate this work to

my Parents (Mr. Vilas P. Muley and Mrs. Seema V. Muley),

my Spouse (Mrs. Radhika S. Muley)

and family (Sachin V. Muley, Prachi S. Muley, Neel S. Muley and Krish S. Muley)

for their continuous support and motivation all the way !

ACKNOWLEDGMENTS

It is with immense gratitude that I acknowledge the continuous support, constructive suggestions and encouragement of my thesis advisor, Prof. N. M. Ravindra, during my entire course of research. Without his excellent advice and guidance on this topic, this work could not have been accomplished.

I thank my dissertation committee members Dr. Ken Ahn, Dr. Michael Booty, Dr. Michael Jaffe and Dr. Anthony T. Fiory for serving as my committee members as well as their helpful comments and discussions. I felt deeply privileged to work with them.

I thank the MTSE Program and Mr. Tony Howell, Director, Educational Opportunity Program at NJIT for the financial support that enabled me to focus on my research. I acknowledge with thanks the input from Ms. Clarisa Gonzalez-Lenahan, Associate Director of Graduate Studies in formatting and improving the presentation in this doctoral thesis.

I am thankful to the developers of the Open-Source software codes namely Quantum Espresso, Boltztrap, LAMMPS, and VMD, which made it easier to model materials at the nanoscale. I would like to express my sincere thanks to all my lab mates and friends, especially, Chiranjivi Lamsal and El Mostafa Benchafia, for their support and technical discussions.

A special thanks to my parents and spouse, Radhika, for their continuous support, motivation and love. I would also like to thank my elder brother, Sachin, sister-in-law Prachi, and nephews, Neel and Krish, for their support.

TABLE OF CONTENTS

TABLE OF CONTENTS
(Continued)

Chapter **Page**

TABLE OF CONTENTS
(Continued)

Chapter **Page**

TABLE OF CONTENTS
(Continued)

Chapter **Page**

LIST OF TABLES

LIST OF FIGURES

LIST OF FIGURES
(Continued)

Figure **Page**

LIST OF FIGURES
(Continued)

LIST OF FIGURES
(Continued)

Figure **Page**

LIST OF FIGURES
(Continued)

Figure **Page**

LIST OF FIGURES
(Continued)

Figure **Page**

LIST OF FIGURES
(Continued)

Figure **Page**

LIST OF FIGURES
(Continued)

Figure **Page**

LIST OF FIGURES
(Continued)

Figure **Page**

LIST OF FIGURES
(Continued)

Figure **Page**

LIST OF FIGURES
(Continued)

Figure **Page**

LIST OF FIGURES
(Continued)

Figure **Page**

LIST OF SYMBOLS

Γ	Gamma point in irreducible Brillouin zone
K, K’	Points in irreducible Brillouin zone
Π	Pie (3.1415)
C_{60}	Fullerene
CNT	Carbon Nano Tube
FLG	Few Layer Graphene
OPV	Organic Photovoltaics
GO	Graphene Oxide
FET	Field Effect Transistor
GNR	Graphene Nano Ribbon
LCAO	Linear Combination of Atomic Orbitals
EG	Energy Gap
BNC	Boron and Nitrogen Doped Graphene
EO	Electro Optic
Ψ	Psi (Wave Function)
χ	Response Function
ρ	Density Operator
σ(ω)	Cross Section for Optical Absorption
Γ(q,ω)	Energy Loss Function
RTP	Rapid Thermal Processing
MWIP	Multi-wavelength imaging pyrometers

IR	Infrared
HEB	Hot Electron Bolometer
FFM	Force Friction Microscopy
TEP	Thermoelectric Power
SLG	Single Layer Graphene
BLG	Bilayer Graphene
S	Seebeck Coefficient
DFT	Density Functional Theory
LDA	Local Density Approximation
HEG	Homogeneous Electron Gas
PWSCF	Plane Wave Self Consistent Field
NVE	Microcanonical Ensemble
NPT	Isothermal Isobaric Ensemble
NVT	Constant Volume Canonical Ensemble
NEMD	Non Equilibrium Molecular Dynamics
LAMMPS	Large-scale Atomic/Molecular Massively Parallel Simulator
GPL	GNU General Public License
VMD	Visual Molecular Dynamics
MFP	Mean Free Path
DOS	Density of States
AGNR	Armchair Graphene Nanoribbon
ZGNR	Zigzag Graphene Nanoribbon

DGBLG	Dual Gated Bilayer Graphene
©	Copyright
∫	Integration
Å	Angstrom (10^{-10} meters)
®	Registered
≈	Approximately
∂	Partial Differential
#	Number Sign
IBZ	Irreducible Brillouin Zone

CHAPTER 1

INTRODUCTION

1.1 Objective

The objective of this dissertation is to study and analyze the electronic, optical and thermoelectric properties of graphene and graphene nanoribbons, as a function of number of layers, doping, chirality, temperature, and lattice defects.

1.2 Background Information

Coal, a form of carbon, has been the driving force for the industrial revolution. In recent times, nanostructured form of carbon has become a significant part of another technological and scientific revolution in the field of nanotechnology. The field of nanoscale science has been significantly molded by research on carbon nanostructures. Different structures of sp^2 hybridized carbon have been worked upon and most important ones are the soccer ball structure called fullerene (C_{60}), the single atom thick planar form of carbon called graphene, the "rolled up" tubular sheets of graphene termed as carbon nanotubes (as shown in Figure 1.1) [1].

Graphene can be considered as the building block for the other carbon allotropes such as fullerenes and carbon nanotubes. The research on the different nanostructures of carbon has been shown to be 'self-enhancing' as this field is highly interconnected and many research groups are working together with a view to bridge the gap between laboratory and industry as well as to use the significant properties of the novel materials in a vast variety of applications. Discovery of fullerenes in 1985 [2, 3] paved the way for

the incidental discovery of carbon nanotubes in 1990s [4] and experimental feasibility of graphene in 2004 [5].

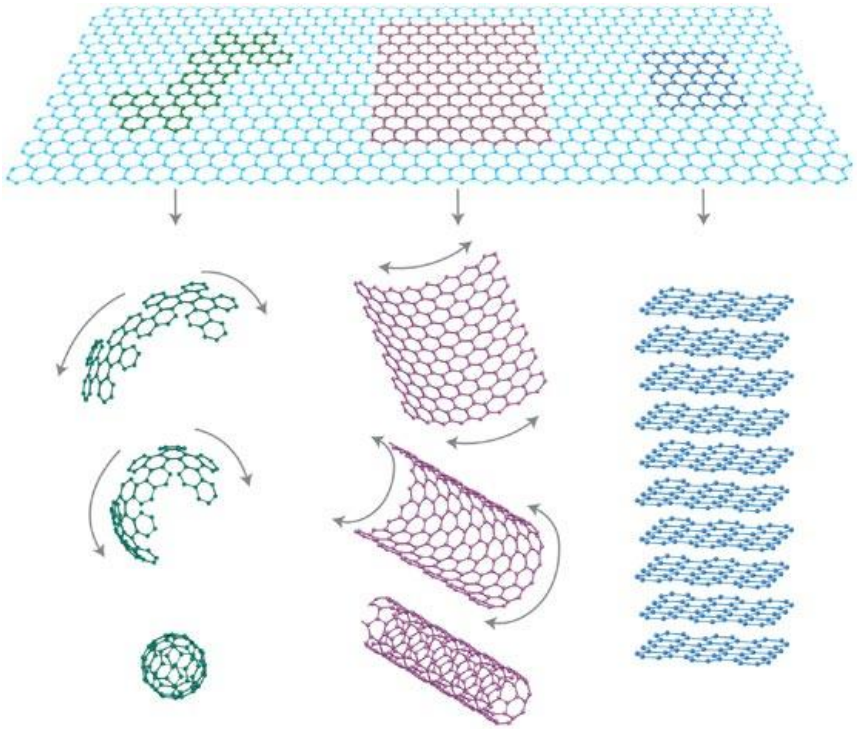

Figure 1.1 Graphene is a 2D building material for carbon materials of all other dimensionalities. It can be wrapped up into 0D buckyballs, rolled into 1D nanotubes or stacked into 3D graphite [6].

Fibrous carbon materials with uniquely high strength to weight ratio such as carbon fiber reinforced composites and graphene have been applied in various equipment for sports (such as tennis rackets) as well as orthopedics [7, 8]. These nanostructures are reported to exhibit exceptional mechanical properties, such as, Young's modulus higher than 1 TPa in case of CNTs [9] as well as in graphene [10] and fullerene. Advances in the knowledge of the various properties of these nanostructures provide motivation for further research and exploring possibilities for practical applications and production of these materials in industries.

Theoretically, the electronic and optical absorption properties of graphene have been published in 1947 by Wallace [11]. However, in October 2004, monocrystalline and highly stable graphitic films were successfully fabricated using the mechanical exfoliation of graphite with a scotch tape, under ambient conditions [5, 12]. Films were found to be semi-metallic with a small overlap of the valence and conduction bands and shown to have strong ambipolar electric field effect. Scientists, who isolated the graphene, Andre Geim and Konstantin Novoselov, were awarded the Nobel Prize in Physics in 2010 [13]. Earlier, graphene was considered to be inseparable and thermodynamically unstable to exist as a single layer [14]. Stability of graphene is attributed to its strong covalent planar bonds [6]. As shown in Figure 1.2, graphene is about 0.34 nm thick and it is composed of carbon atoms arranged hexagonally in a honeycomb structure, with sp^2 bonds, which are about 0.14 nm long [15, 16]. Carbon atoms have a total of 6 electrons; 2 electrons in the inner shell and 4 electrons in the outer shell. The four outer shell electrons, in an individual carbon atom, take part in chemical bonding; but it is known that each carbon atom in planar structure of graphene is bonded to three carbon atoms on the two dimensional plane, so that one electron is free for electronic conduction in third dimension. These free electrons are called pi (π) electrons. They are located above and below the graphene sheet and are highly mobile. In graphene, these pi orbitals are known to overlap and help in enhancing the carbon- carbon bonds. Multilayer graphene with less than 10 layers is sometimes referred as Few Layer Graphene (FLG). The properties of graphene with more than 10 layers are the same as bulk graphite [6, 17]. Carbon atoms in a layer of graphene are covalently bonded and Van der Waals interaction exists between the neighboring layers of graphene.

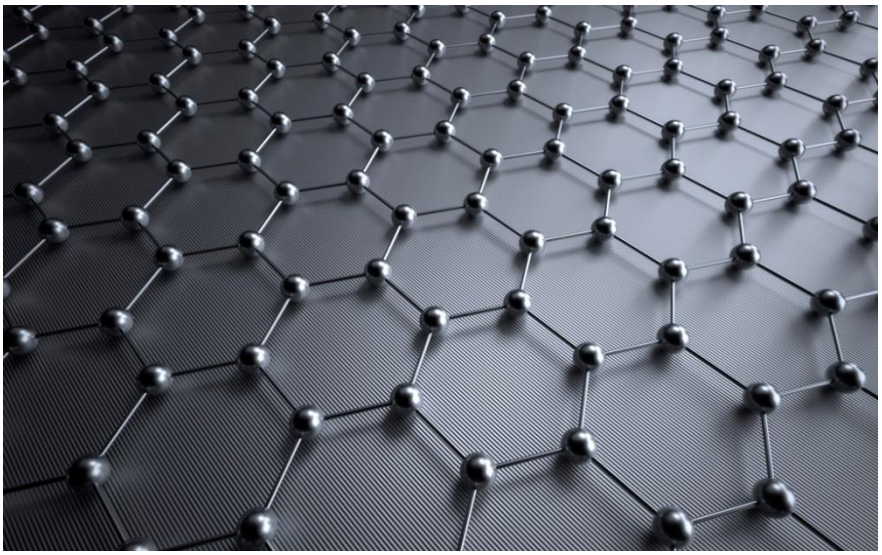

Figure 1.2 Graphene's honeycomb lattice [16].

Graphene is known to be optically transparent, between 70% – 90%, the transparency being dependent on the thickness. It has high electronic and thermal conductivities as well as transport properties [18]. With these extraordinary properties, it has been reported to be used for applications such as sensors [19, 20], solar cells [21], supercapacitors [22], nanocomposites, wear resistant films, organic photovoltaics (OPV) as well as transparent displays and flexible electronics [23-26].

The main obstacle has been to commercially produce graphene. Key challenge is synthesizing and processing of bulk quantities of graphene sheets. Graphene is known to form irreversible agglomerates or even re-stacking to form graphite through interlayer Van der Waals interaction, unless they are well separated from each other. It is not commercially viable in making OPVs with tiny flakes of graphene using scotch tape; therefore, alternative techniques such as epitaxial growth and copper foil technique have been developed [27, 28]. With advances in these techniques, it is important to completely understand and study the structure and properties of graphene and its derivatives.

Graphene has been studied with condensed physics phenomena [29, 30], and it is a material suggested to replace silicon due to its excellent electron mobility (about 100 times greater than silicon), large mean-free-path [5], as well as the ability to modify its electrical properties by doping and chirality [31]. There has been plethora of theoretical and experimental research in investigating the electronic, optical, mechanical, chemical and thermoelectric properties of graphene. Scientifically important phenomena such as half integer quantum Hall effect and Berry's phase [32], the breakdown of the Born–Oppenheimer approximation [33], and confirmation of the existence of massless Dirac Fermions [32], have been observed in graphene.

In making attempts for fabricating single layer graphene, various top-down approaches have been utilized such as mechanical exfoliation [5, 6] [6, 34], liquid phase exfoliation of graphene [35] as well as bottom-up approaches such as epitaxial growth of graphene on SiC substrate [36] or metal substrates [37-39], chemical vapor deposition [40], and substrate free gas synthesis [41]. All these approaches have paved way for further research on graphene.

As a thin film, graphene has been grown on metallic substrates and the growth phenomenon is studied since the 1970s. Single layer graphite growth was also reported on various transition-metal substrates [42-44]. Even before these experiments, the separation of the graphene layers in graphite, in the form of graphite intercalation compounds, exfoliated graphite and so called graphene oxide (GO), has been studied [45]. Recently, Nina et al. [46] have reported that intercalated graphite can be readily exfoliated in dimethylformamide to obtain suspensions of crystalline single- and few-layer graphene sheets. Concept of reversible intercalation of graphite by using non-

oxidizing bronsted acids can narrow the path for the commercialization of graphene. This research has revisited decades old belief that graphite intercalation must involve host-guest charge transfer, resulting in partial oxidation, reduction or covalent modification of graphene sheets.

The term “graphene” was proposed by Boehm et al. in 1986, to describe a single atomic sheet of graphite [47]. Mechanical exfoliation route enables one to obtain very high crystallinity and purity samples, which have been used to explore the transport properties of graphene. Following this route of making graphene, various papers have reported unique properties of graphene, in contrast to bulk graphite. Novoselov et al. [6, 12, 34, 48], Nair et al. [18, 49, 50] and Berger et al. [51] are some of the scientists who have reported the same.

In this view of the feasibility of making graphene commercially and the possibility to tailor its electronic properties, it is a promising material for the electronic industry. It is known that the optical and thermoelectric properties are a function of electronic and structural properties of a material. This led to the research on improving these properties by various techniques, especially chemical doping, isotopic substitution, isoelectronic impurities and hydrogen adsorption [52]. Effects of layers and edges of graphene on its properties have been explored to understand their significance in applications as a layer in the multilayered configuration of the devices. The need for thermal management of devices in the view of their nano-sizes is the driving force for such a material with enhanced thermoelectric properties.

CHAPTER 2

LITERATURE REVIEW

In this chapter, a brief theoretical background of the electronic, optical, mechanical and thermoelectric properties of graphene, along with the relevant research in scientific literature, is presented. Table 2.1 presents the properties of graphene and its comparison with other materials.

Table 2.1 Properties of Graphene and Comparison with other Materials

Property	Value	Comparison with other materials	Ref.
Breaking strength	42 N/m	More than 200 times greater than steel	[53]
Elastic limit	~ 20%	<1% for steel	[24]
Carrier mobility at room temperature	200,000 $cm^2V^{-1}s^{-1}$	More than 100 times higher than Si	[54]
Thermal conductivity	~ 5000 W/mK	More than 10 times higher than copper	[55]
Maximum current density	> 10^8 A/cm	~ 100 times larger than Cu	[56]
Optical absorption coefficient	2.30%	~ 50 times higher than GaAs	[18]

2.1 Electronic Properties

One of the most important applications of graphene is in electronics. As discussed in Chapter 1, the studies of electronic structure of graphene date back to year 1947. Most of the major manufacturers in the field of semiconductor fabrication have vested huge

interests in analyzing the properties of graphene for its application in electronic circuits. This is because of the fact that silicon is approaching its fundamental size limits in device miniaturization.

A linked and important property that differentiates graphene is the high mobility of charge carriers in excess of 2,00,000 cm^2/Vs. This shows that nearly ballistic transport is observed in the sub-micron regime. The challenging fact is that this value of mobility is true only for large scale graphene, which is a gapless material. Due to zero bandgap, it is not possible to turn off the device completely without high leakage current. This hampers the prospects of using graphene in making Field Effect Transistors (FETs) for applications in logic circuits. Various techniques used by researchers in order to open up the band gap in graphene include quantum confinement in one direction giving rise to graphene nanoribbons (GNRs) (as shown in Figure 2.1) [57-59], application of strain [60, 61] and use of bilayer graphene (BLG) [62, 63]. Graphene nanoribbons have been found to possess two achiral structures: armchair and zigzag nanoribbons. Both armchair and zigzag GNRs are known to demonstrate bandgaps above 200 meV for widths less than 10 nm [64]. Zigzag GNRs belong to middle-gap semiconductors, and antiferromagnetic configuration which is possible to make experimentally. Armchair GNRs possess non-magnetic configurations which have width-dependent energy gaps [65]. Recent experiments have shown the fabrication of flat and curved GNRs by various techniques such as unzipping carbon nanotubes, e.g., wet chemical technique using acid reactions, a catalytic approach using metal nano-clusters as scalpels, as well as a physico-chemical method using argon plasma treatment [66].

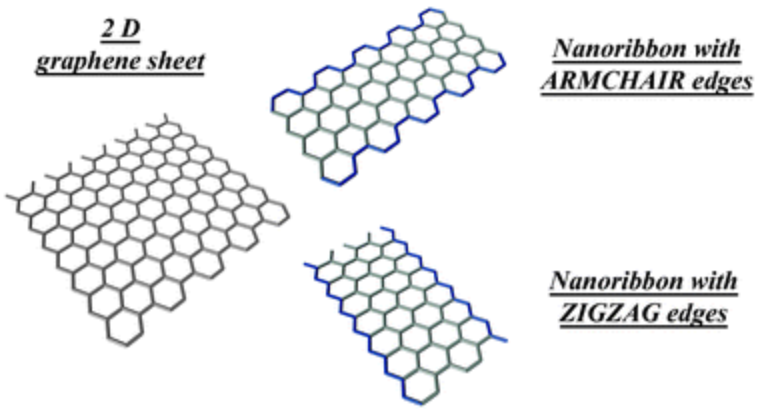

Figure 2.1 Zigzag and armchair edges in monolayer graphene nanoribbons. The edge structure and the number of atomic rows of carbon atoms normal to the ribbon axis determine the electronic structure and ribbon properties [59].

Band gaps, to the extent of few hundreds of milli-electron volts, have been achieved with BLG by application of a perpendicular electric field to the bilayer [67]. The gap in the stacked bilayer graphene arises due to formation of pseudospins between the layers, and hence making it possible to electrically induce a band gap [68].

However, the predicted high mobility could not be achieved for large area graphene. This is explained by the fact that as the band gap opens up, it becomes more parabolic, and so the effective mass increases and mobility decreases. Thus, the bandgap leads to reduced mobility of GNRs. Apart from this; GNRs have rough edges which wipe out the band gap opening, thus raising further challenges in fabricating them. Since the band gap is inversely proportional to the width of GNRs, a band gap of 0.5 eV is required for room temperature operation of transistors and this will require the width of the GNR to be less than 5 nm which is difficult to fabricate with much accuracy.

As discussed earlier, carbon atoms in graphene are arranged in a honeycomb lattice with two atoms per unit cell, as shown in Figure 1.2. The electronic band structure of graphene can either be described using tight binding approximation (TBA) or the

similar Linear-Combination of Atomic Orbitals (LCAO), which is used more commonly in chemistry. The two atoms in graphene which make up two non-equivalent sub-lattices are bonded by trigonal σ bonds. These σ bonding sp^2 orbitals are formed by the superposition of the *s*, p_x and p_y orbitals of atomic carbon, whereas the p_z orbital remains non-hybridized. The hybridized orbital is geometrically trigonal and planar. This is the reason why each carbon atom within graphite has three nearest neighbors in the graphite sheet. There is an overlap of p_z-orbitals of neighboring carbon atoms and distributed π-bonds are formed above and below each graphite sheet. This leads to the presence of delocalized electron π bands, similar to the case of benzene, naphthalene, anthracene and other aromatic molecules. In this regard, graphene can be considered to have an extreme size of planar aromatic molecules.

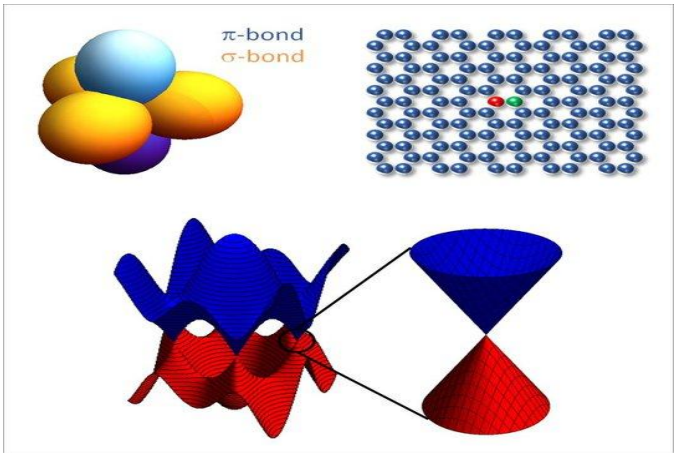

Figure 2.2 Geometry of sp^2 hybridized carbon atom. Each of the two equivalent carbon atoms within one unit cell (red and green) contributes one cosine-shaped band to the electronic structure. These bands cross exactly at the Fermi level, where they form a Dirac cone with a linear electronic dispersion. Valence and conduction band are shown in red and blue, respectively [69].

The geometry of sp^2 hybridized carbon is shown in Figure 2.2 [69]. The covalently bonded in-plane σ bonds are found to be primarily responsible for the

mechanical strength of graphene and other sp^2 carbon allotropes. The σ electronic bands are completely filled and they have an energy separation larger than the π bands and hence the effects of σ bands on graphene's electronic behavior can be neglected in a first approximation. The out-of-plane π-bond is primarily responsible for its peculiar electronic and optical properties. It should be understood that, in a real sample of graphene, the layer is not strictly a 2D crystal; it is found to be rippled when suspended [70] or it adheres to the corrugation of its supporting substrate [71]. In these cases, a mixing of the σ and π orbitals occurs, which needs to be taken into consideration when calculating the electronic properties of graphene [72]. One of the simplest known evaluations of the band structure and, therefore, its electronic properties is obtained by examination of the π bands in a tight binding approximation. The first reference to the band structure calculation was published by Wallace in 1947 [11]. The 2D nature of graphene allows plotting the relationship in the entire first Brillouin zone (as shown in Figure 2.3).

In the case of graphene, the bottom of the conduction band and the top of the valence band is not at the Γ point as in the case of most of the metals and semiconductors, but it is present at another high symmetry point at the boundary of the first Brillouin zone, at the so called K points, as shown in Figure 2.3. The valence and conduction bands meet but they do not overlap. Density of states is null at the K points themselves. This is the reason for graphene being known as a zero band gap semiconductor or semimetal. The first Brillouin zone contains two non-equivalent K points called K and K'.

The most interesting aspect of graphene physics is that the band structure and physical properties of this material can be influenced by nanostructuring, functionalizing,

mechanically straining, etc., yielding new physics to be studied and further explored. The Dirac points, K and K' are most important points in the structure of graphene. They are located at the corners of the Irreducible Brillouin Zone (IBZ) and one can define their positions in momentum space [73].

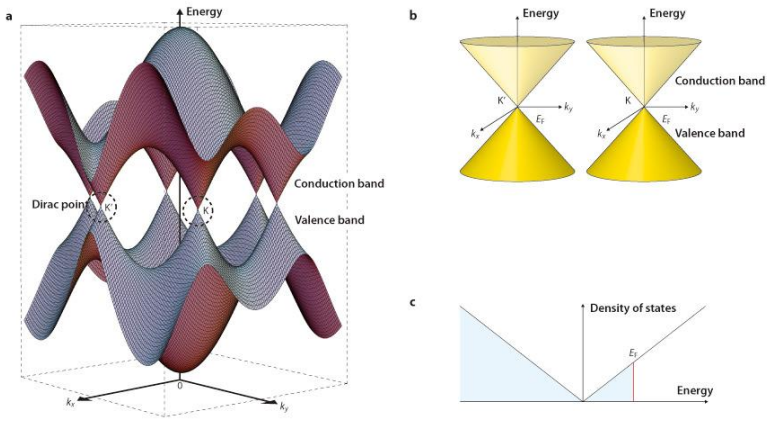

Figure 2.3 (a) Energy bands near the Fermi level in graphene. The conduction and valence bands cross at points K and K′. (b) Conical energy bands in the vicinity of the K and K′ points. (c) Density of states near the Fermi level with Fermi energy E_F [74].

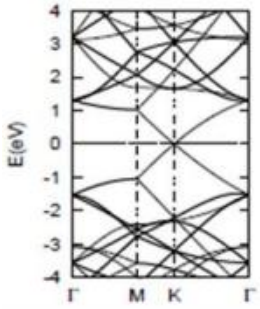

Figure 2.4 Band structure of pure graphene sheet [75].

Figure 2.4 shows the bandstructure of pure graphene sheet [75]. It can be found that the bandgap location of graphene is different from a typical semiconductor. In graphene, the conduction and valence bands coincide at a conical point, known as a Dirac

point. The energy-momentum plot shows the quasi-particles in the material behaving like massless Dirac Fermions [76].

The unique bandstructure of graphene allows higher mobility of electrons than in other materials. Electronic transport in a medium with negligible electrical resistivity is called ballistic transport, which is possible in very pure and defect free graphene. Multichannel ballistic transport has also been reported in the case of multi-walled carbon nanotubes [77]. Electrons are capable of ballistic movement over long distances in graphene [76]. The velocity of electrons in graphene is a maximum at the Fermi velocity, which is about 1/300 of the speed of light. This allows graphene to be an excellent conductor. Doping enables changing the position of the Fermi levels in the band structure of graphene at room temperature [78].

2.1.1 Electronic Density of States (DOS) of Graphene

Figure 2.5 shows the theoretical DOS of graphene [73] indicating its semi-metallic nature. Zero bandgap in graphene is completely different than in case of diamond, which is a wide bandgap semiconductor.

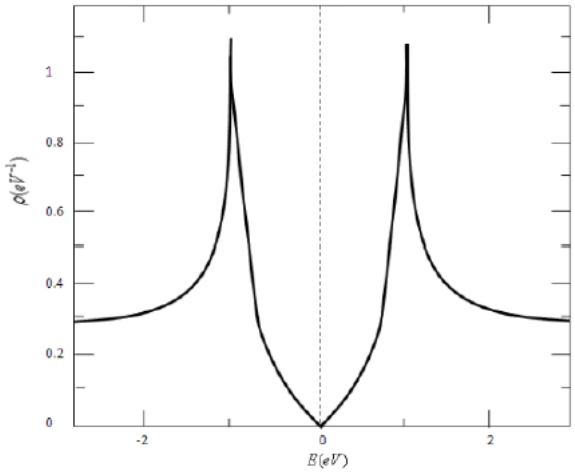

Figure 2.5 Electronic Density of States (DOS) of graphene [73].

2.1.2 Effects of Doping on Electronic Structure in Graphene

Recently, there have been numerous attempts to fabricate graphene based devices by engineering its band gap by doping. Investigations on doped graphene nano-ribbons [79, 80] indicate that doping with nitrogen or boron can make it possible to obtain n-type or p-type semiconducting graphene. It is shown experimentally that nitrogen doping of graphene [79] tends to move the Dirac point in the band structure of graphene below the E_F and an energy gap is found to appear at high-symmetric K-point.

Ci et al. [81] synthesized a novel two-dimensional nano material where a few carbon atoms on a graphene sheet are replaced by equal number of boron and nitrogen atoms. The concentration of the dopant atoms was controlled by keeping same B/N ratio. This novel nanomaterial was found to be semiconducting with a very small band gap. Synthesis of similar BNC materials have been reported by Panchakarla et al. [82]. The electronic properties of nitrogen and boron doped armchair edged graphene nanoribbons (AGNR) is also reported [83]. Nitrogen is found to introduce an impurity level above the donor level, while boron introduces an impurity level below that of the acceptor level. This is different from single wall carbon nanotubes (CNTs), in which, the impurity level is neither donor nor acceptor in their systems. In CNTs, the donor and acceptor levels are derived mainly from the lowest unoccupied orbital and the highest occupied orbital.

Theoretically, introduction of gap in graphene is shown by oxidation of mono-vacancies in graphene [84], hetero-bilayers of graphene/boron nitride [85, 86], F-intercalated graphene on SiC substrate [87], and bilayer graphene-BN heterostructures [88]. Experimentally, the substitutional doping in carbon of boron nitride nanosheets, nanoribbons, and nanotubes has been reported [89]. It is reported experimentally that the

sp^2 hybridized BNC nano-structure, with equal number of boron and nitrogen atoms, can also open finite bandgap. The bandstructure of bilayer graphene is as shown in Figure 2.6 [90].

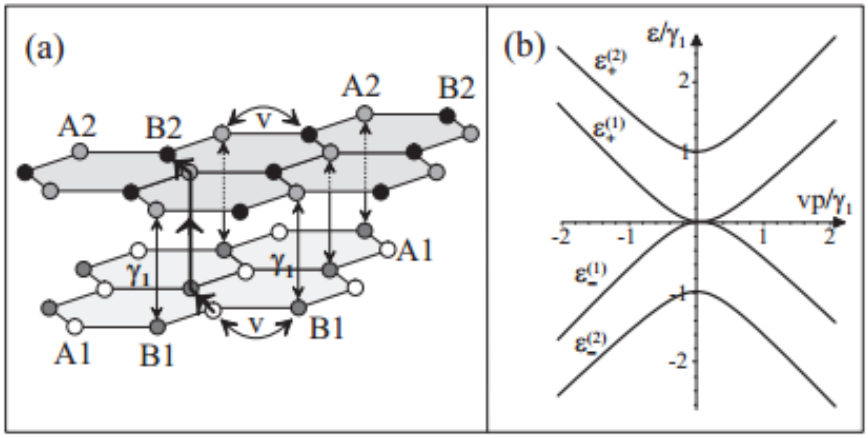

Figure 2.6 (a) Schematic figure of bilayer graphene containing four sites of unit cell, (b) Electronic band structure of bilayer graphene [90].

Fujii et al. [91] studied the role of edge geometry and chemistry in the electronic properties of graphene nanostructures. This paper has presented scanning probe microscopic as well as first principles characterization of graphene nanostructures. It is clear that the challenges in making chemically doped graphene and different edge geometries, experimentally, have been overcome to a large extent. One of the challenges of experimentally grown graphene is the grain boundaries which are known to affect the electronic and optoelectronic properties of graphene [92]. In fact, grain boundaries present localized states, which have been proven to be crucial in regard to the electronic, magnetic and mechanical properties that depend on the atomic line junctions. These localized states allow for decoration of line defects with adsorbates, hence opening a novel route for nanosensor applications [93].

Chang et al. [65] have investigated the geometric and electronic properties of edge decorated graphene nanoribbons using DFT. Three stable geometric structures have been demonstrated as shown in Figure 2.7. These structures have been found to have high free carrier densities, whereas a few are semiconductors due to zigzag-edge-induced anti-ferromagnetism.

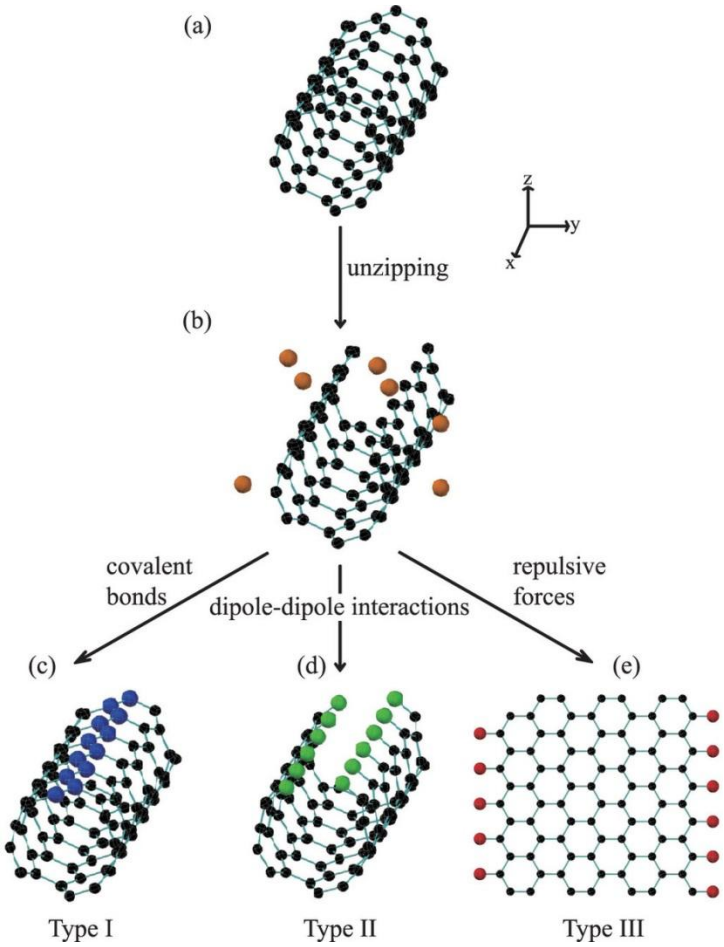

Figure 2.7 (a) A single wall carbon nanotube is used as starting material. (b) The unzipped nanotube is put in an environment of decorating atoms. (c)–(e) Three possible geometric structures are formed by three types of decorating atoms with different edge-edge interactions [65].

Sanjuan et al. [94] have presented the correlation of geometry of graphene with its mechanical, electronic, and chemical properties. Chen et al. [95] have presented the

electronic properties of graphene supported on (0001) SiO_2 surface, using DFT. Electronic properties have been shown to be dependent on the underlying substrate surface properties as well as percentage of hydrogen passivation. By application of methyl for passivation of oxygen-terminated SiO_2, it is possible to improve the charge carrier mobility of graphene by further reducing the interaction of graphene sheet with oxygen-terminated SiO_2. External electric field can also aid in modulating the charge transfer between the graphene and the SiO_2 surface. Hexagonal BN (hBN) is a widely used substrate for graphene devices. Kretinin et al. [96] have reported the electronic properties of graphene encapsulated with different two-dimensional atomic crystals such as, molybdenum, tungsten disulphides, hBN, mica, bismuth strontium calcium copper oxide, and vanadium pentoxide. They have noted that devices made by encapsulating graphene with molybdenum or tungsten disulphides are found to have high carrier mobilities of ~ 60,000 $cm^2V^{-1}s^{-1}$. Encapsulation with other substrates (such as mica, bismuth strontium calcium copper oxide, and vanadium pentoxide) results in exceptionally bad quality of graphene devices with carrier mobilities ~ 1,000 $cm^2V^{-1}s^{-1}$. The differences have been attributed to the self-cleansing occurring at the interfaces of graphene, hBN, and transition metal dichalcogenides. This cleansing process is not found to take place on atomically flat oxide surfaces.

Motivated by the current experimental and theoretical reports, we have investigated the effect of doping of boron and nitrogen on the electronic properties of the graphene systems using first-principles electronic structure calculations based on density functional theory.

2.2 Optical Properties of Graphene

Research on graphene has shown the unique optical properties [97], including its strong coupling with light [18], high-speed operation [98], and gate-variable optical conductivity [99], are extremely useful for addressing the future needs of the electro-optic (EO) modulators. It is found that, in the optical range, graphene has a constant index of refraction of 2.6 in an ultra-wide band of wavelengths ranging from ultraviolet up to near-infrared and it shows constant absorption of 2.3%.

The rise in interest of graphene in photonics and optoelectronics is clear from its applications ranging from solar cells and light-emitting devices as well as in touch screens, photo-detectors and ultrafast lasers. These applications in nano-photonics are explored due to the unique combination of its optical and electronic properties [100].

Due to its visual transparency, graphene has immense potential as transparent coatings. Optical absorption of graphene is anisotropic for light polarization being parallel/perpendicular to the axis normal to the sheet. Experimentally, it is reported that as compared to graphite, the optical and energy loss spectra of graphene show a redshift of absorption bands and $\pi+\sigma$ electron plasmon and disappearance of bulk plasmons [101, 102]. Optical properties are the prominent characteristics that differentiate graphene from graphite. Ebernil et al. [103] have reported that π and $\pi+\sigma$ surface plasmon modes in free-standing single sheets of graphene are present at 4.7 and 14.6 eV, respectively, which are found to be present at 7 eV and 25 eV in case of bulk graphite. This red shift is reported to decrease as the number of layers of graphite reduces.

Among the many areas in which graphene has prominent applications, an important one is for making sensors due to the sensitivity of its electronic structure to

adsorbates [19]. Low energy loss electron spectroscopy provides a way of detecting changes in the electronic structure that are highly spatially resolved.

2.2.1 Linear Response: The Kubo Formula

An entirely interacting electronic system is considered. It is described by the Hamiltonian H, as per Equation (2.1), under the action of an external time-dependent field [104]:

$$H_{tot} = H + H_{ext}(t) = H + \sum_i \emptyset^{ext}(r_i, t) = H + \int dr\, \rho(r)\emptyset^{ext}(r, t) \quad (2.1)$$

The density operator is defined as per Equation (2.2):

$$\rho(r) = \sum_i \delta\,(r - r_i) \quad (2.2)$$

The induced density is defined as per Equation (2.3):

$$\rho^{ind}(r, t) = <\psi\,(t)|\,\rho\,(r)|\,\psi(t)> - <\rho> \quad (2.3)$$

In the linear response regime, the external field is assumed to be weak, so that one can expand the exact time-dependent ground state in the field, at the first order, as per Equation (2.4) with external Hamiltonian in the picture.

$$|\,\psi\,(t)> \equiv e^{-iHt}|\psi_I(t)> \approx |\,\psi> + i \int_{-\infty}^{t} dt' H_I^{ext}\,(t')|\,\psi> \quad (2.4)$$

As per the Kubo formula:

$$\rho^{ind}(r,t) = \int_{-\infty}^{t} dt' \int_{-\infty}^{\infty} dr' \chi\,(rr', t-t')\emptyset^{ext}(r',t') \tag{2.5}$$

Where, the response function is defined as:

$$\chi_{\rho\rho}(\mathrm{rr}',\mathrm{t}) \equiv\ -\mathrm{i} < [\rho_{\mathrm{I}}(\mathrm{r},\mathrm{t}), \rho_{\mathrm{I}}(\mathrm{r}')] > =\ -i < \left[\delta_{\rho_{\mathrm{I}}(\mathrm{r},\mathrm{t})}, \delta_{\rho_{\mathrm{I}}(\mathrm{r}')}\right] > \tag{2.6}$$

2.2.2 Dielectric Function and Energy Loss Spectra

In determining the optical properties, a calculation of the dielectric function, ε(q,ω) is generally reported, as a function of the frequency, ω, and the momentum transfer, q. If one assumes that the light polarization is parallel to the electric field momentum q, the cross section for optical absorption, σ(ω), i.e., the optical absorption spectrum, is then proportional to the imaginary part of the macroscopic dielectric function, as shown in Equation (2.7).

$$\sigma(\omega) \propto \mathrm{Im}(\in_{\mathrm{M}}\ (\mathrm{q}\ \rightarrow 0, \omega)) \tag{2.7}$$

Where,

$$\in_{M}^{-1}\ (\omega) \equiv 1 +\ \lim_{q\,\rightarrow 0} \frac{4\pi}{|q|^2} \ll \chi\,(q,\omega) \gg \tag{2.8}$$

The limit q→0 is taken because the momentum carried by a photon is vanishingly small compared to the crystal momenta of a bulk material.

One of the important quantities, which can be measured experimentally, is the energy loss function. The loss function, Γ(q,ω), is related to the imaginary part of the inverse dielectric function:

$$\Gamma(q,\omega) \propto \mathrm{Im}\left(\frac{1}{\varepsilon(q,\omega)}\right) \tag{2.9}$$

Contrary to the absorption cross section, the loss function is defined for finite momentum transfer q. One can measure the momentum transfer in the Electron Energy Loss Spectroscopy (EELS) through the deflection of the electron beam. Equation (2.9) is only valid for angular resolved EELS on bulk materials and not for spatially resolved EELS on isolated nano objects.

2.2.3 Literature Review of Graphene and Doped Graphene

It is known that graphene is optically transparent in the visible spectrum. Hence, in order to use it in optoelectronic applications, it needs to be tailored in order to absorb specific wavelength region of the spectra.

Optical properties of graphite and graphene have been studied by Sedelnikova et al. [105] and Marinopoulos et al. [106, 107]. Marinopoulos et al. reported the absorption spectrum for different values of c/a ratio of graphite and compared it with BN sheet. Eberlein at al. [103] performed the plasmon spectroscopy of graphene in conjunction with ab-initio calculations of the low loss function. Numerous reports have been published regarding the surface plasmons in graphite and carbon nanotubes. The studies about SWCNTs (Single Wall CNTs) for radius r → ∞ can be applicable for free

standing single graphene sheets. The E field of a fast moving particle is elongated along its direction of travel; therefore, when it passes perpendicular through a foil of graphene, mainly, the out-of plane mode with momentum ħq parallel to E should be excited. These modes are reported to be forbidden in a single layer graphene, while they have a weak intensity in graphite. Although, momentum transfer is close to zero, q is known to have considerable in-plane component. Sedelnikova et al. [105] have reported the effects of ripples on the optical properties of graphene.

It can be observed that the peaks at 4 eV in single boron doped and nitrogen doped graphene is lesser in intensity and there are well-defined peak changes in the broader plateau. Since individual boron or nitrogen doping does not induce band gap in graphene, it is found that the peak at 4 eV is not changed. However, it is found that by increasing doping of boron or nitrogen in graphene, the high intensity peak at 4 eV decreases in intensity, indicating the reduction in absorption. The peak intensity and position are not found to change for out-of-plane polarization. Hence, one can note that the 4 eV peak is of principal importance while considering tailoring of optical properties of graphene. However, this is not the case for in-plane modes in bilayer graphene with AB stacking and graphite. Thus, any loss below 10 eV due to these plasmons can be attributed to the presence of adsorbates on graphene. This characteristic of graphene makes it highly sensitive to adsorbates.

Figure 2.8 shows the imaginary part of dielectric function of graphene, both pristine and doped graphene for E⊥c and E||c [100].

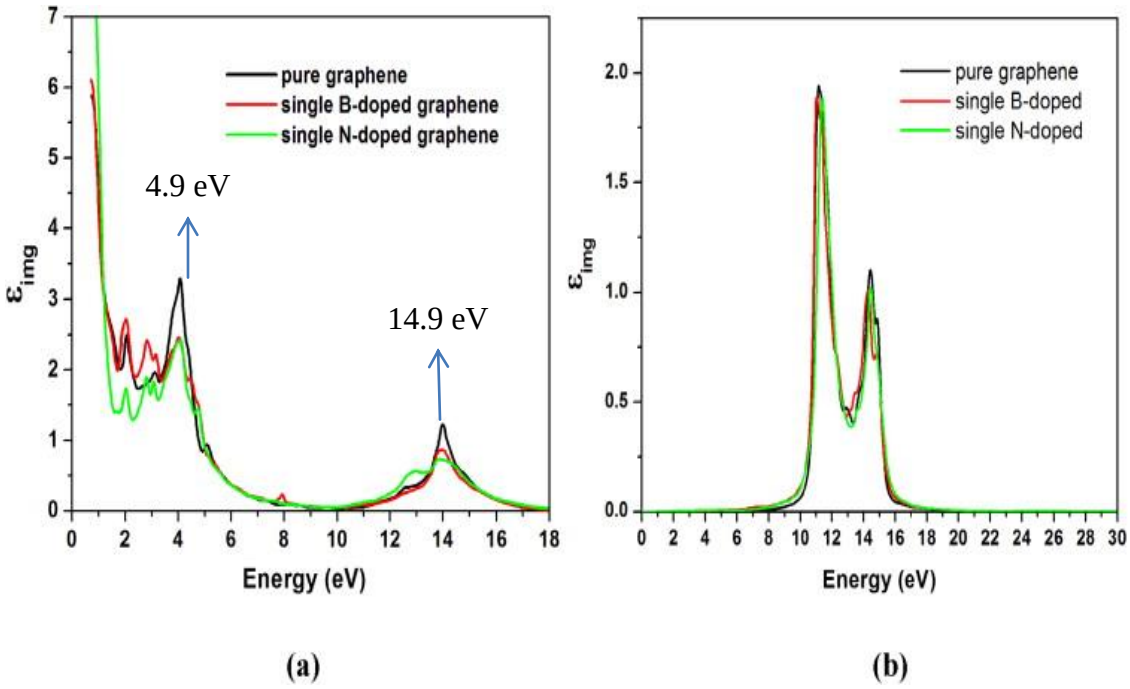

Figure 2.8 Comparison of imaginary part of dielectric function of pure graphene with that of single boron and nitrogen atom doped graphene sheet for E⊥c (a) and E||c (b), based on simulations. Peaks observed at 4.9 eV and 14.9 eV originate from π →π* and σ →σ* interband transitions, respectively [100].

The absorption spectrum for E⊥c in graphene shows a significant peak at energies up to 5 eV and another peak structure of broader energy range which starts at about 10 eV and has a weak intensity peak at 14 eV. These peaks originate from $\pi \rightarrow \pi^*$ and $\sigma \rightarrow \sigma^*$ interband transitions, respectively, in accordance with previous interpretations by Marinopoulos et al. [100]. The experimental value of the high intensity peak is at 4.6 eV, as reported by Eberlein et al. [103]. The imaginary part of the dielectric function shows a singularity at zero frequency for E⊥c. This makes graphene to exhibit optically metallic property for E⊥c, while for E||c, graphene shows semiconductor properties. Electron energy loss function, reflectivity, refractive index and extinction coefficient are presented in Figure 2.9. For parallel polarization of light with respect to the plane of graphene sheet, reflectivity is more and transition is less at this energy range.

In the energy range of 10 to 15 eV, for light polarization perpendicular to graphene sheet, the reflectivity is on the higher side.

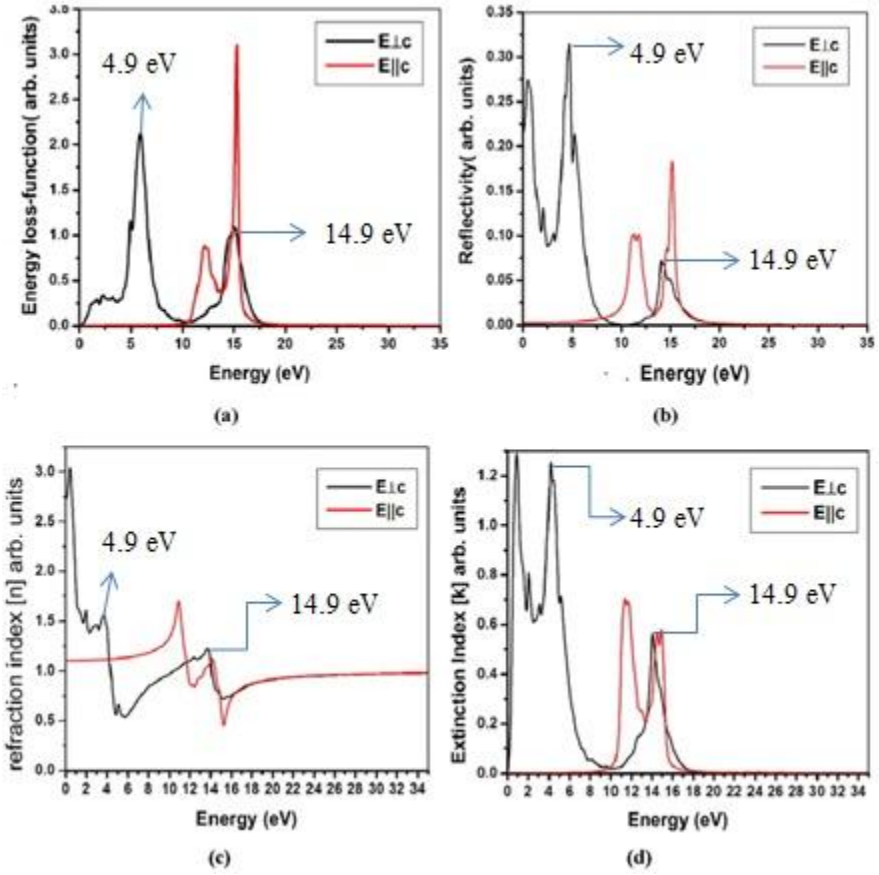

Figure 2.9 Simulation of the electron energy loss function (a), reflectivity (b), refractive index (c) and extinction coefficient (d) of pure graphene for E⊥c and E||c [100]. Peaks observed at 4.9 eV and 14.9 eV originate from $\pi \rightarrow \pi^*$ and $\sigma \rightarrow \sigma^*$ interband transitions, respectively [100].

The imaginary part of the dielectric constant of single layer graphene, for out of plane polarization (E||c) consists of two prominent peaks, at about 11 and 14 eV, as presented by Marniopoulos et al. [100]. This polarization spectrum varies with respect to graphite. Graphite has a weak intensity peak in the energy range of 0–4 eV. This peak is absent in the case of single layer graphene. The real part of the dielectric function of pure

graphene is plotted in Figure 2.10. The value of static dielectric constant (value of dielectric function at zero energy), in case of E⊥c, is reported to be 7.6, while it is 1.25 in the case of E||c.

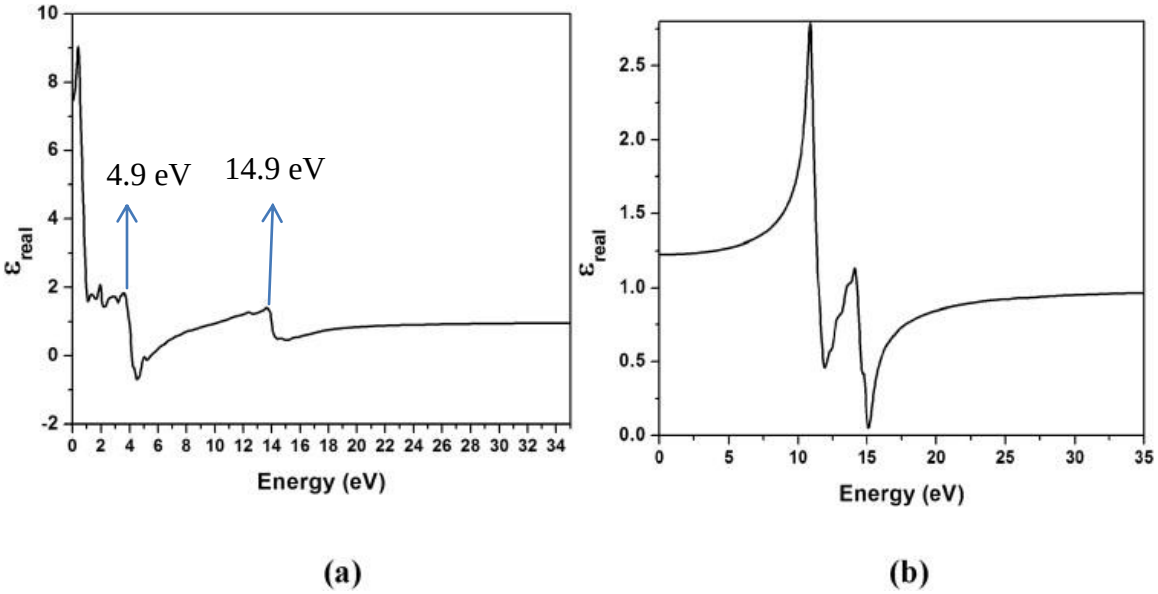

Figure 2.10 Simulated real part of the dielectric function of pure graphene for E⊥c (a) and E||c (b). Peaks observed at 4.9 eV and 14.9 eV originate from π →π* and σ →σ* interband transitions, respectively [100].

Corato et al. [108] presented the optical properties of bilayer graphene nanoflakes theoretically, in order to explore the role of π – π interactions. They considered two different types of π-stacking with varying electronic gap or ionization potential. Their results indicate a red shift and broadening of lowest excitations. Thus, one can expect overall broadening of the optical absorption in ensemble of flakes. In heterogeneous ensemble of flakes, there is a possibility of presence of low-energy excitations with considerable charge transfer character, which can be demonstrated by proper exploitation of chemical edge functional.

Chernov et al. [109] have discussed the optical properties of graphene nanoribbons encapsulated in single-walled carbon nanotubes and reported the photoluminescence in both visible and infrared spectral range. These photoluminescent peaks are found to be resonant and their position is dependent on the geometrical structure of the ribbon.

Hong et al. [110] have reported thermal and optical properties of free standing flat and stacked single-layer graphene in aqueous media. They demonstrated that stacked graphene structures thermalize rapidly than flat graphene and display non-equilibrated electron and phonon temperatures upon excitation. Hot electron luminescence characteristic of graphene is found to depend on Fermi energy and the morphology of graphene. Thus, it has been interpreted that the morphology of graphene structure could affect its optical and thermal properties.

Graphene is also known to be an extraordinary material for THz devices as its THz properties have an origin in the band structure [111]. In the low THz regime, graphene is found to exhibit linear response, where its optical conductivity follows Drude-like behavior and is mainly governed by its Fermi level. Based on this phenomenon, many THz devices have been proposed. In the high THz regime, graphene is found to exhibit third-order non-linear response which can be orders of magnitude larger than what can be achieved in other frequency ranges such as IR or visible.

The experimental measurements of the optical properties of graphene, in the long wavelength range, are very limited in the literature.

2.2.4 Emissivity (An Infrared Optical Property): Significance and Basics

Rapid thermal processing (RTP) is a widely used processing technique for the manufacture of silicon and other semiconductor devices. The short process times, high temperature ramp rates and very high temperatures are essential in RTP [112]. During RTP, factors such as the temperature uniformity across the surface of the wafer, process reproducibility and accuracy are core requirements to its successful operation. Temperature uniformity across the wafer is affected by design parameters such as wafer patterning, temperature accuracy, and uniformity of irradiation. Temperature accuracy depends on the technique used for the measurement. The use of thermocouples in temperature measurement is highly intrusive and the delicate thermocouple wires make handling of wafers especially difficult and pose problems in sealing vacuum chambers [113].

In this regard, pyrometers are the most suitable choice of temperature measurement techniques [114]. Pyrometers are used to measure the amount of radiation emitted within narrow window of wavelength. However, for obtaining accurate temperature measurements using these devices, the knowledge of some key optical properties of the material being analyzed, is essential. Spectral emissivity is defined as the ratio of the radiation emitted by a given substrate to that of a blackbody under the same conditions of temperature, wavelength, angle of incidence, and direction of polarization [115]. Emissivity is a number between 0 and 1. The wavelength, transmittance, absorptivity, absorption coefficient, reflectivity, etc. of the materials are taken into consideration [116] in designing pyrometers. Ratio pyrometry is a technique of radiometric method which can eliminate the like terms from ratios of measured signals.

Multi-wavelength imaging pyrometers (MWIP) are designed to obtain profiles of temperature, remotely, of targets of unknown wavelength-dependent emissivity [115]. MWIP incorporates least-squares fit of the signal taken from the radiometric model of an infrared (IR) camera and is based on the simultaneous measurement of emissivity and temperature. The selection of the emissivity model is a decisive factor for the accuracy of the least-squares based MWIP technique for measurement of temperature [117, 118].

The significant interest of radiative properties of materials is in applications such as process monitoring and control of materials, non-contact temperature sensors, pyrometry, infrared detectors including bolometers, night vision etc. [116]. However, these properties are not readily available in the literature and the results presented in this study can be helpful in various applications including thermal management of high power electronic devices. The need for thermal management in electronics has led to the development of alternate materials, techniques of manufacturing, and designs, in order to have a higher lifecycle of the electronic devices; cost factor is also an important consideration.

Radiative properties of graphene are of significant interest in applications such as process monitoring and control, non-contact temperature sensors, pyrometry and infrared detectors. These require knowledge of spectral emissivity. Knowledge of emissivity as well as the relation of resistance as a function of temperature for multilayered configuration, with graphene as one of the layers, can be used to make non-contact sensing devices such as Hot Electron Bolometer (HEB). We have studied various configurations of graphene based bolometers and proposed alternative configurations for

achieving better ratio of change in resistance with respect to temperature i.e., for improving sensitivity.

2.2.5 Significance of Multilayered Structures and Their Optical Properties

In industrial scenario, one needs to control or reduce friction, wear and corrosion of components, in order to extend the life of the device. This also leads to conservation of scarce material resources, saving of energy as well as improvising safety in engineering applications. Nano-coatings such as thin films and engineered surfaces have been developed and applied in industry for decades. Nano-coatings can be used to enhance surface-related characteristics such as optical, magnetic, electronic and catalytic properties.

In phenomenon of reflection of light in a thin film, both the top and bottom boundaries have to be taken into consideration. In a thin layer, the incident light will be reflected back at the secondary boundary, followed by the transmission through the first boundary. This leads to a path difference between the two waves (incident light wave and reflected wave from the inner surface). This phase difference results in interference of the waves. Therefore, the reflectance is a function of the thickness of the films and the wavelength of light.

2.2.6 Device Studies

A bolometer is a device which responds to increase in temperature (on interaction with the incident thermal radiation) by changing its resistance [115, 119]. When an electron system is coupled to power, electrons as well as phonons are driven out of thermal equilibrium, leading to creation of hot electrons. Hence, such a bolometer is called Hot

Electron Bolometer (HEB) [120]. It is essentially a sensitive thermometer. It can be used in conjunction with a spectroscope to measure the ability of some chemical compounds to absorb wavelengths of infrared radiation. One can obtain important information about the structure of the compounds with this technique.

Graphene has the ability to absorb light from mid-infrared to ultraviolet with nearly equal strengths. Hence, it has found applications in optical detectors. Graphene is particularly well suited for HEBs due to its small electron heat capacity and weak coupling of electrons and phonons, which causes large induction of light with small changes in electron temperature. Small value of electronic specific heat makes it possible for faster response times, higher sensitivity and low noise equivalent power [115]. At low temperatures, usually in the cryogenic range, electron-phonon coupling in metals is very weak. Usual operating range of operation of HEBs is cryogenic. Graphene based HEBs can be used at higher operating temperatures due to lower electron-phonon scattering even at room temperature along with the highest known mobilities of charge carriers at room temperature [48, 119, 121].

2.3 Mechanical Properties

The past few decades have witnessed an exponential increase in research on nanomaterials; examples include two-dimensional structures and carbon nanotubes. Nanomaterials are materials with a characteristic length less than 100 nm. At the nanoscale, increased ratio of surface area to volume can drastically change the mechanical behavior and properties of a material. This phenomenon in novel nanomaterials has been unexplored at large in view of a large number of innovations in

materials science. Mechanical characterization of nanomaterials is performed by indentation testing on nanoscale thin films. In a traditional indentation test, such as the Vickers hardness test, the hardness is evaluated by division of the force applied by a pyramidal tip by the projected indentation area after unloading. This approach is easier at the macroscale. However, at the nanoscale, it requires significantly more accurate equipment. The measured area is known to have errors from effects such as elastic recovery and pile-up [122].

In 1986, Doerner and Nix proposed a methodology to determine the hardness and elastic modulus from load-displacement curves as obtained by nanoindentation technique [123]. This method was further refined in 1992 by Oliver and Pharr in order to determine the elastic modulus of thin films from the linear portion of the force-displacement unloading curve [122, 124]. The reduced elastic modulus, E_r, contact stiffness, S, and area are shown to be related by the Equation (2.10).

$$S = \frac{2\sqrt{A_c}}{\sqrt{\pi}} * E_r \qquad (2.10)$$

S can be calculated from the linear portion of the load-displacement unloading curve, as shown in Figure 2.11 [122].

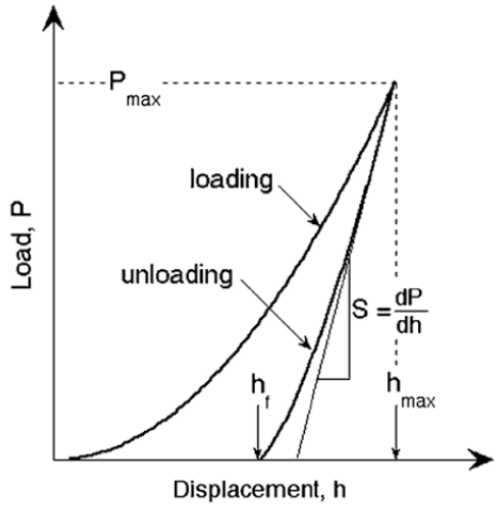

Figure 2.11 Typical load-displacement curve. Notice the linear portion of the unloading curve, where S is found [122].

Reduced modulus can be easily calculated by knowing the area. Hardness is related to force and indented area as per the following equation:

$$H = \frac{F}{A_c} \tag{2.11}$$

Where, H is hardness, F is maximum force applied, and A_c is the contact area at the maximum load. Nanohardness machines record the force applied, but the contact area is difficult to determine at the nanoscale [122]. The elastic modulus and hardness require determination of the accurate contact area. The Oliver-Pharr technique includes creation of an "area function" for the indenter. This area function is characteristic of each indenter, and it relates the contact area to the depth of penetration of the tip. The accurate indentation area corresponds to the projected contact area at maximum load, as shown in

Figure 2.12**.** This aspect is a variation from the classical approach of hardness testing, where the projected area of the residual indentation is considered, after unloading.

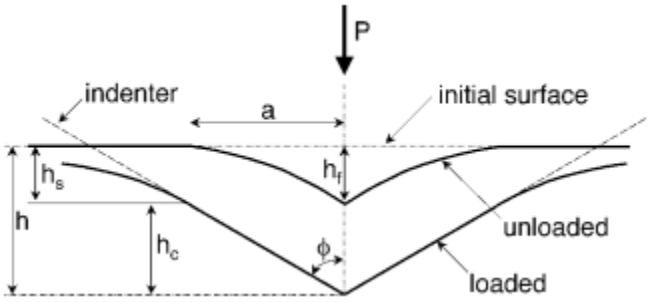

Figure 2.12 Schematic of indentation with sink-in deformation. The schematic shows multiple indentation depths at maximum loading and after unloading. The correct contact area is related to the depth h_c [122].

2.3.1 Literature Review

Graphene is reported to have an elastic modulus of the order of 1 TPa and intrinsic strength (130 GPa) [125]. However, the mechanical properties of graphene need to be fully understood in view of its proposed applications in nano devices (sensors, resonators, etc). For graphene, being a two dimensional material, its in-plane tensile behavior is the most important mechanical behavior. The elastic modulus E, the Poisson's ratio ν, and the intrinsic strength are the most fundamental mechanical properties. The values of elastic modulus and intrinsic strength have been employed using free standing indentation based on Atomic Force Microscope (AFM). Lee et al. [53] used instrumented indentation and reported the value of elastic modulus as 1.0 TPa for single layer graphene, while Frank et al. [126] have measured the value of E as ~ 0.5 TPa for stack of graphene nanosheets (n<5). Zhang and Pan [127] reported the elastic modulus of monolayer of graphene as 0.5 TPa, bilayer graphene as 0.89 TPa, and observed reduction

in the values with increasing number of layers of graphene. Lee et al. [128], using Raman spectroscopy, reported the values of elastic modulus of monolayer and bilayer graphene as 2.4 and 2.0 TPa, respectively.

Force friction microscopy (FFM) showed that there is monotonical decrease in the monolayer graphene's frictional force with increasing thickness. It is reported that the graphene's frictional force is roughly twice that of bulk graphite, and the tip-graphene adhesion is found to be constant [129-131]. Interlayer shear strength of graphene has been determined by performing AFM on a corrugated substrate and it is determined to be greater than or equal to 5.6 MPa, which is orders of magnitude less than its tensile yield stress [132]. This research prompted the application of graphene as a thin film and led to the determination of mechanical properties of graphene as suspended sheet and in polymer composites [23]. However, its out-of-plane mechanical properties, such as hardness, are relatively less explored. In the applications using graphene as an electrode, it is important to understand and quantify the load and impact that graphene can withstand. A protocol was developed recently in the Sansoz lab to evaluate the mechanical properties, especially the hardness, of thin films by using atomic force microscopy (AFM) nanoindentations [133].

Cao [125] has discussed the recent advances in the atomistic studies of mechanical properties of graphene, with a focus on the in-plane tensile stress response, geometric characteristics, and free-standing indentation response of graphene. Numerical analysis can offer link between scientific research and engineering applications such as nano sensors, nanotransistors, and others. Three basic tensile loading modes, such as uniaxial tensile stress / strain and biaxial tension are applied based on displacement

control. Graphene has a six fold symmetric lattice. The in-plane orientation of graphene has been typically stated using chirality angle θ. θ varies from 0 to 30˚, where θ = 0˚ and 30˚ correspond to zigzag and armchair directions, respectively. It is reported that, irrespective of the magnitude of tensile deformation, graphene is isotropic with regards to elastic modulus and the Poisson's ratio [125].

The intrinsic stress on graphene cannot be measured directly using AFM; it can be evaluated by performing inverse analysis of experimental data using Finite Element Modeling (FEM). Breaking indentation force from FEM needs to be compared to the experimental counterpart. Based on this approach, Lee et al. [53] reported the Piola-Kirchoff (2^{nd} PK) Stress as 42 ± 4 N/m and the Lagrange strain as 0.25. However, in this approach, it is assumed that the bending stiffness of graphene is to be neglected and the difference between mechanical behavior (calculated by considering the second and third order non-linear terms of elastic modulus) and the true behavior in free standing indentation is neglected.

DFT studies can also help to determine the values of the 2^{nd} PK stress and Lagrange strain. Liu et al. [134] have determined the phonon spectrum of monolayer graphene under uniaxial tensile stress with DFT simulation, and it was proposed that the maximum stress will correspond to the first occurrence of phonon instability. Based on this, they reported the values of 2^{nd} PK stress and Lagrange strain to be 31.03 N/m and 0.3 for zigzag direction, while for armchair direction; the values are 30.3 N/m and 0.21, respectively. Wei et al. [135] used DFT simulations and predicted ductile nature of graphene by plotting the stress-strain behaviour. In the case where the tensile strain is

larger than Lagrange strain, graphene is still found to support a stress which is lower than the tensile stress, especially in the zigzag direction.

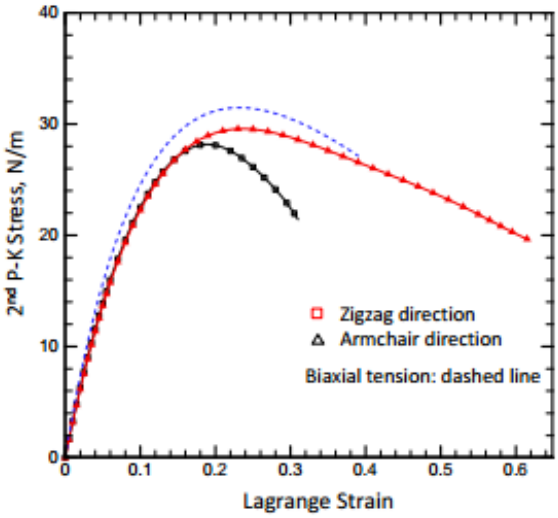

Figure 2.13 Simulation based relationship between the second P-K stress and Lagrange strain of graphene determined under uniaxial/biaxial stress tension [125].

Figure 2.13 shows that the failure strain of graphene is much higher than the Lagrange strain along zigzag and armchair directions [125]. Thus, graphene is found to be anisotropic with regards to the fracture resistance. Graphene exhibits much stronger failure strain along zigzag direction than the armchair direction.

The literature reports variations in the failure strains in graphene using DFT simulations and MD (Molecular Dynamics) methods. This is attributed to different C-C bond behaviour. The C-C bond behavior, in DFT simulations, is dependent on the behavior of electrons explicitly calculated in the simulations. This type of behavior is a superposition of both the electrostatic attraction between the nucleus and electrons, as well as, repulsion between the electrons. Thus, the bonds show non-linear behavior without cutoff feature, which is the typical characteristic of the bonds in MD methods.

It is reported that the elastic modulus is highly over-estimated in the free standing indentation test mainly due to vdW (Van der Waals) interaction between indenter tip and graphene, known as the vdW effect. The vdW force between graphene and side wall is not large enough to maintain a clamped boundary condition of graphene in free standing indentation tests.

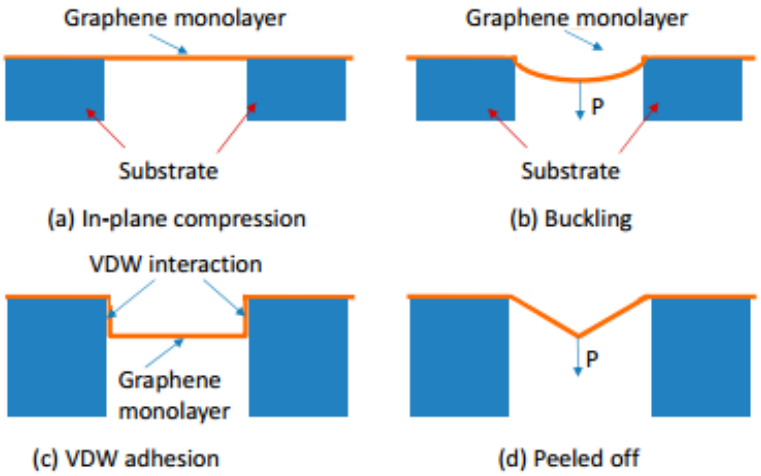

Figure 2.14 Schematic of the creating mechanism of the true boundary condition of graphene in free standing indentation: (a) In-plane compression; (b) Buckling; (c) Adhesion by the vdW interaction between substrate wall and graphene; and (d) Peeled off by the indentation load [125].

Figure 2.14 shows the reported mechanism for large size suspended graphene in free standing indentation [125]. One can find that, for a 2D material, the mechanical properties are a function of a thickness, vdW interaction with indenter tip, substrate and / or within graphene layers, geometric defects (vacancies). These factors affect the mechanical deformation of graphene under different loading conditions / modes. Using the conventional continuum theory, the measured mechanical properties of graphene will be different, as the factors mentioned earlier, are not accounted properly. Hence,

numerical simulations, at atomistic scale, play a significant role in the understanding of mechanical properties of 2D materials.

2.4 Thermoelectric Properties

Transforming energy from one form to another has always been an integral step in technological advances. Driving force of water or wind can be used to run mills; nuclear energy can be used to produce electricity. In the context of environmental concerns, that becoming increasingly prevalent in today's society, it is essential to find novel, clean and efficient ways to produce energy as well as using it more efficiently. Identifying new ways to reuse waste heat energy in a processing industry is a challenge.

Till date, most energy resources are consumed as thermal energy. The average yield in these processes is around 30%. The remaining 70% of thermal energy is wasted and the major part of this residual energy is rejected in the environment in the form of thermal energy. It is extremely difficult to recycle the waste heat energy using traditional conversion methods, since it is typically associated with temperature ranges below 700 K. There are strong variations of power density in the residual heat and it is stored within various environments. Over the past decade, there has been a growing interest in thermoelectric materials, which have the peculiar property, by which they can convert heat into electricity, and vice-versa. This conversion is interesting due to the fact that electricity can be stored and used for various applications. Moreover, thermoelectric conversion presents numerous advantages, such as the absence of maintenance, independence from the type of heat source, the ease of setup and the longevity of this technology (due to the absence of moving parts). Thermoelectric generators consist of

different modules containing many couples of p-type and n-type semiconducting materials (as can be seen in Figure 2.15) [136]. The heat diffusion changes with the diffusion of charge carriers in the same direction, producing a voltage.

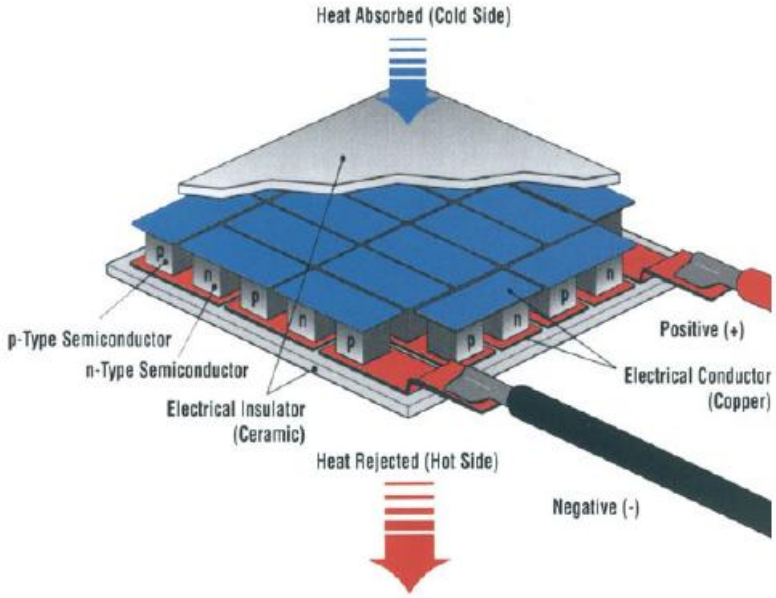

Figure 2.15 A Seebeck power module which generates electrical power [136].

Thermoelectrics are also used for cooling applications. These coolers are most widely used and known as Peltier coolers. They are used to cool electronic components, and are also used for many consumer products, such as camping/car coolers. They can be used as precise temperature regulators (error around 0.01 K) with essential electronic feedback.

The thermoelectric (TE) effect is a phenomenon in which either a temperature difference creates an electric potential or an electric potential creates a temperature difference. An interesting transport property, thermoelectric power (TEP) has been a source of information to physicists for over a century [137]. TE devices are used as generators and coolers to convert thermal energy into electrical energy or vice versa. The

potential of a material for TE applications — solid state refrigeration and power generation is determined by a measure of the material's TE figure of merit, $ZT=S^2\sigma T/\kappa$, where, S is the thermoelectric power (also called Seebeck coefficient), σ the electrical conductivity, and κ is the thermal conductivity of the material. Efficient TE energy conversion, therefore, requires materials that have an enhanced power factor $S^2\sigma$ and reduced κ [137, 138]. The state of the art TE materials possess a value ZT ~ 1, at room temperature. There is no well-defined theoretical value of ZT. Values of ZT ~ 2-3 make TE refrigeration competitive with vapor compression refrigeration systems. Even a modest increase in value of ZT would, therefore, provide important opportunities for applications.

Thermoelectrics could play an important role in the future. Presently, thermoelectric applications use compounds of Si, Te, Pb, Bi or Se, such as bismuth chalcogenides, lead tellurides, silicides, tin selenide, and others. However, they are not adapted for large scale applications due to many reasons such as high production costs, toxicity of some compounds, high temperature stability, etc. Future research is focused on developing alternate materials to circumvent the aforementioned challenges. This is expected to raise yield by having massive production of cheap, non-toxic and less restrictive thermoelectric device for a larger spectrum of applications. The aim of our study is to model from first-principles calculations the thermoelectric properties of one of the most promising thermoelectric material: Graphene.

2.4.1 Graphene - A Thermoelectric Material

The last decade has witnessed a considerable interest in the electronic properties of graphene [73, 139]. Graphene, a single-atom-thick sheet of carbon atoms arranged in a

honeycomb crystal, exhibits unique properties such as high thermal conductivity, high electron mobility and optical transparency, and has potential applications in nano-electronic and optoelectronic devices. With the integration of these devices, by shrinking their dimensions, thermal management has become a high priority. This has prompted the study of thermoelectric effects in graphene based systems. Recent studies have indicated that ZT could be increased nearly fourfold, by optimizing the potential of graphene systems [140].

The interest in the TEP of a material system is understood not only from its value of ZT but also its sensitivity to the composition, structure of the system as well as its behavior in external fields. The TE effect has made it essential to focus attention of researchers on the interaction of electrons and phonons, impurities and other defects. It is known that the transport parameters S, σ and κ are not independent of each other. The Seebeck coefficient is related partially to the electrical conductivity. This has created a challenge for theorists and experimentalists to search ways to increase the value of ZT. An optimization of one of the parameters, such as Seebeck coefficient, for any material will involve understanding and appropriate modification of the electronic properties. Conventional thermocouples, made of metal or metallic alloys, can generate Seebeck voltages typically tens of microvolts per Kelvin [141, 142]. The thermocouples made from semiconductors, with tailored material properties and geometry [143], can generate voltages of a few hundreds of microvolts per Kelvin. One of the objectives in studies of thermoelectrics has been to search for materials with optimized electronic band structures and thermal properties [144]. The recent interest in thermoelectrics has been stimulated by the prospect of using graphene with improved Figure-of-Merit, due to its unique

combination of electrical and thermal properties and their possible modification.

Graphene exhibits interesting TE properties compared to elemental semiconductors. It has higher TEP and can be made to change sign by varying the gate bias [145-147]. The unique properties of graphene include high mechanical stiffness and strength, coupled with high electrical and thermal conductivity. These properties make graphene an exciting host for future applications in nanoelectronics, thermal management and energy storage devices. Technical advances have now been made possible by the realization of tailor-made 2D graphene systems, such as single-layer graphene (SLG), bilayer graphene (BLG), graphene nanoribbon (GNR), graphene dots, graphene superlattices as well as defected graphene. Most of the experimental and theoretical work has been concerning modification of the electrical and thermal conductivity of such systems. A review on the progress in research in graphene has been presented by Novoselov et al.[148] as well as Sankeshwar et al. [149].

The present work addresses an important component of thermoelectric transport in graphene, namely, TEP, also referred as thermopower. TEP has been a powerful tool for probing carrier transport in metals and semiconductors [143].

2.4.2 Literature Review

Fundamentally related to the electrical conductivity of a material, the thermoelectric transport coefficients are determined by the band structure and operating scattering mechanisms. These coefficients can offer unique information complementary to the electrical transport coefficients. The minimal conductivity at the Dirac point is characteristic of graphene [73, 139]. Away from the Dirac point, the dependence of electron concentration on conductivity is a function of nature of the scatterers. At low

temperatures, the conductivity of graphene is limited by scattering of the impurities and disorder, which in turn, depend on the sample preparation. In the absence of extrinsic scattering sources, phonons are the major intrinsic source of scattering [139].

The thermoelectric effect of Dirac electrons has been initially experimentally investigated in mechanically exfoliated samples of graphene on ~300 nm SiO_2/Si substrates [145-147]. The number of layers in graphene samples can be identified by optical contrast of the samples with scanning probe studies and Raman spectroscopy. A controlled temperature difference, ΔT, is applied to the sample by a heater and the resulting voltage which is thermally induced, ΔV, is measured by the voltage probes to obtain the TEP, $S = -\Delta V/\Delta T$.

The TEP of graphene can be modulated by varying the gate voltage, V_g. The nonexistence of a gap in the carrier dispersion in graphene, as in SLG, results in a direct transition between electron-like transport to hole-like transport as the gate voltage is tuned through the charge neutrality point (Dirac point).

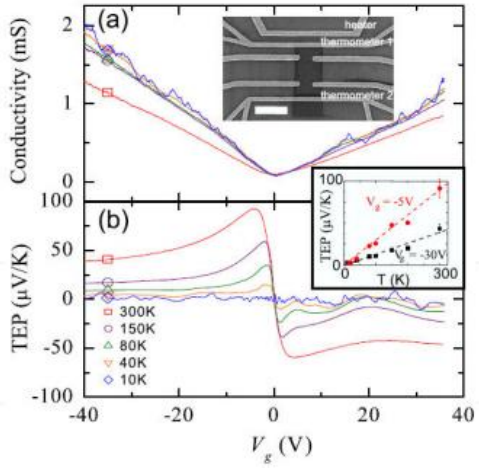

Figure 2.16 Experimentally reported (a) Conductivity and (b) TEP of a graphene sample as function of V_g for T=300 K (square), 150 K (circle), 80 K (up triangle), 40 K (down triangle), and 10 K (diamond). Upper inset: SEM image of a typical device, the scale bar is 2 μm. Lower inset: TEP values taken at V_g = - 30 V (square) and -5 V (circle). Dashed lines are linear fits to the data [145].

Zuev et al. [145] measured, simultaneously, the conductance and TEP of different SLG samples. Figure 2.16 shows conductivity and TEP trends for graphene sample as a function of applied gate voltage over a temperature range of 10-300 K. The conductivity becomes minimum at the charge neutrality point (CNP), corresponding to $V_g=V_D$, where the Dirac point $V_D= 0$ V for the device. They observed a change in sign of the TEP across the CNP ($V_D=0$ V) as the majority carrier density changed from electrons to holes. The linear temperature dependence of TEP is shown in the inset for two values of V_g, far away from the CNP. This nature of temperature dependence suggests that the mechanism for thermoelectric generation is diffusive, with the absence of phonon-drag component.

Wei et al. [146] reported, experimentally, that the thermoelectric transport is uniquely sensitive to the electronic band structure. Checkelsky and Ong [147] have reported measurements of TEP, S, and Nernst, S_{yx}, signals in graphene in non-zero and zero magnetic fields. In the absence of a magnetic field, they observed nominally linear-in-T dependence of the peak value S_m from ~20 K to 300 K (as shown in Figure 2.17) [147]. This observation was in addition to the change in sign of S with V_g. Seol et al. [150], in their study of the thermal properties of graphene, have reported measurements of electrical conductivity, TEP and thermal conductivity of SLG flakes. They reported the room temperature values ~ - 80 μV/K for the Seebeck coefficient (S).

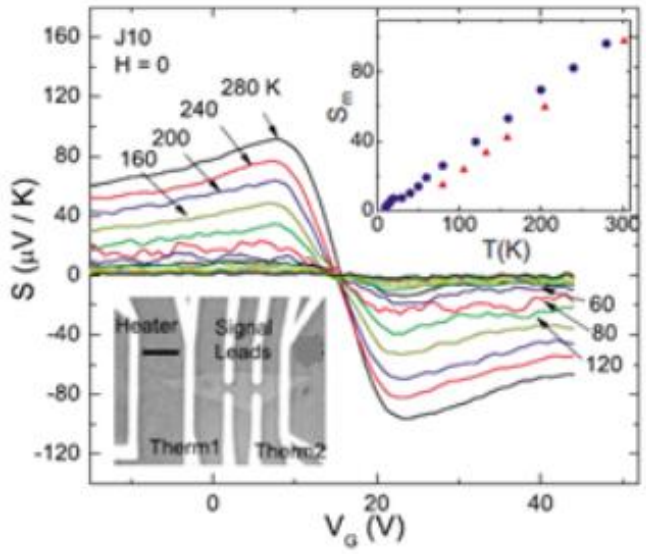

Figure 2.17 Curves of TEP based on experiments, $S=-S_{xx}$ vs V_g in sample J10 (left inset) in zero magnetic field at selected T. The curves are anti-symmetric about the Dirac point which occurs at the offset voltage V_0=15.5 V. The peak value S_m (right inset) is nominally linear in T from 25 to 300 K [147].

In recent experiments, Shi et al. [151] have investigated the carrier mobility-dependence of thermoelectric transport properties of SLG in zero and non-zero magnetic fields, as shown in Figure 2.18. It is reported that, in the absence of magnetic field, with increase in mobility, the maximum value of S_{xx} increases, and exhibits an increasingly diverging trend accompanied by a sharper peak- to-dip transition around the Dirac point [151]. It is also noted that the peak-to-dip width is related to the width of the minimum conductivity plateau, which is broader for the low mobility state. This behavior is associated with disorder in graphene. Also, it is found that S_{xx} converges to the same values at high gate voltages on either side of CNP, even for high values of gate voltage for all values of mobility. This phenomenon refers to the fact that the effective charge density is much greater than the fluctuations in the charge density induced by charge impurities near the Dirac point [149].

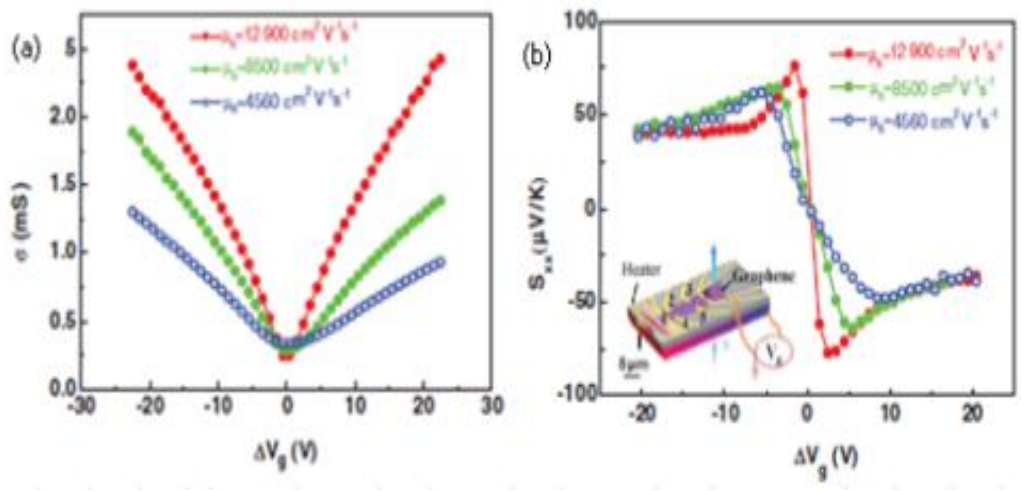

Figure 2.18 Experimental gate voltage dependence of (a) Electrical conductivity, σ, and (b) Seebeck coefficient, S_{xx}, of device A at 150 K with three hole mobility values 12900, 8500 and 4560 $cm^2V^{-1}s^{-1}$. Inset of (b) shows SEM image of the device [151].

Samples of graphene have been grown by different techniques. The main graphene production techniques include wet and dry exfoliation, photo-exfoliation, Chemical Vapor Deposition (CVD), Molecular Beam Epitaxy (MBE) and chemical synthesis (using Sol-Gel Technique). Also, there have been experiments with deposition of graphene on various substrates, mainly SiC [149].

Wu et al. [152] reported the thermoelectric response of relatively high-mobility (~ 20 x 10^3 $cm^2V^{-1}s^{-1}$) single layer graphene epitaxially grown on SiC substrate. For carrier (hole) density away from the Dirac point, it is found to show deviation from the Mott relation. The data shows quadratic dependence instead of linear dependence, reflecting the importance of the screening effect. Hwang et al. [153] have shown that a quadratic correction to TEP appears when the effect of screening and its temperature dependence are taken into account.

Kim et al. [154] have reported measurements of TEP on graphene samples deposited on hexagonal BN substrates. In this case, drastic suppression is achieved for

the disorder. It is shown that, at high temperatures, the measured TEP is found to exhibit enhancement with respect to the TEP predicted from Mott relation. This is attributed to the fact that, at higher temperatures, the inelastic scattering rate is many orders higher than the elastic scattering rate.

Graphene structures have been shown to be grown on metal substrates upto micron thickness with a very few defects. Also, SiC substrates have been shown to be used to grow good quality graphene with a number of layers. C-terminated surface can produce some layers with lower mobility, whereas, Si-terminated surface can form layers with higher mobility [149, 155].

TEP of CVD-grown graphene has also been demonstrated [149, 156]. This concept has been used to apply graphene as a sensitive probe to surface charge doping from the environment to detect gas/chemical. Initially, degassed n-type graphene sample was found to become p-type doped by exposure to gases [157]. These variations are dependent on the nature of the ambient gases in contact and can be interpreted by monotonic change in sign of TEP. In graphene sample, the substrate on which graphene layer is exfoliated and its purity affect the morphology of graphene. In suspended graphene, the substrate is etched away. This makes it possible to suspend graphene over a 100 nm deep trench. In this case, the impurities are stuck to the graphene layer.

Nam et al. [158] have reported measurements of TEP, S_{xx}, for BLG in the temperature range of 30-250 K and for varying charge carrier densities. Similar to the observation in case of single layer graphene, one can observe ambipolar nature of charge carriers by the change of sign at the CNP, in case of BLG, as shown in the Figure 2.19 [158]. The low temperature result of TEP is consistent with the semi-classical Mott

formula. For high charge carrier densities, TEP follows the linear temperature dependence. This implies a weak electron-phonon interaction and negligible phonon-drag effects in case of BLG.

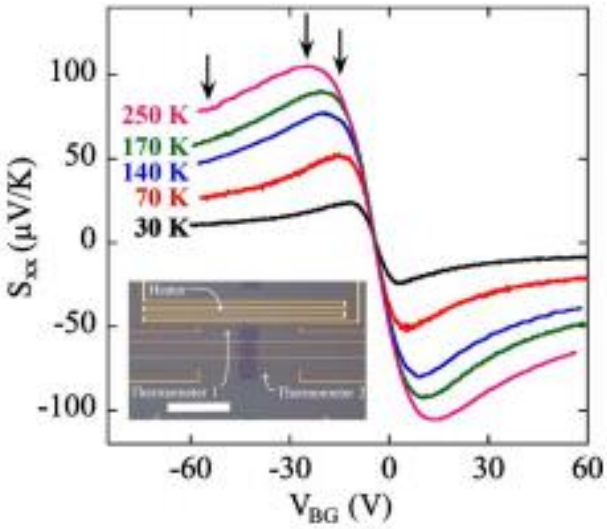

Figure 2.19 Experimental TEP as a function of the backgate voltage V_{BG} in zero magnetic fields and at various temperatures: T= 30, 50, 70, 140, 170, and 250 K. Inset: optical image of a typical device. Size of the scale is 30 μm [158].

To date, there have not been reports on the measurement of TEP of graphene nanoribbons. However, there have been reports using non-equilibrium Green's function, showing enhanced thermoelectric properties of graphene nanoribbons by resonant tunneling of electrons by Mazzamuto et al. [159]. Chen et al. [160] studied the thermoelectric properties of graphene nanoribbons, junctions and superlattices. The role of interfaces in the thermoelectric response of GNR across single junctions as well as periodic superlattices has been discussed. It is observed that increasing the number of interfaces in single GNR system increases the peak ZT values. Thus, the ZT values are maximized in a periodic superlattice. Also, it is reported that the thermoelectric behavior

is controlled by width of narrower component of the junction. It is noted that synthesized chevron-type GNRs should display better thermoelectric properties.

CHAPTER 3

COMPUTATIONAL METHODS

In this section, various computational techniques used to model the electronic, optical, mechanical and thermoelectric properties are discussed.

3.1 Density Functional Theory (DFT)

The main principle of the ab-initio techniques is to solve Schrodinger's equation. This single equation is sufficient to describe arbitrary systems accurately. When applied to many-body problems, the analytical solution is highly impractical. Hence, there is an intense need to look for approximations.

In a short span of time, after Schrodinger's equation was published, the first rudimentary predecessor of DFT was developed by Thomas and Fermi [161]. In this approach, a multi-electronic system based on Fermi-Dirac statistics, assuming the behavior of the system as a homogeneous electron gas, is modeled. The model considers interacting electrons moving in an external potential and provides a highly over-simplified relation between the potential and its electronic density. This theory is quite useful for describing some qualitative trends, such as total energy of atoms. However, there is a major drawback of not being able to predict chemical bonding of atoms in the system.

Another most successful attempt for dealing with many-electron systems is the Hartree-Fock (HF) hypothesis, developed in 1930 by Hartree, Fock and Slater [162]. In this approximation, a multi-electron wave function HF can be calculated as an anti-

symmetric combination (known as the Slater determinant) of wavefunctions i of N electrons (known as spin-orbitals) composing it, including the Pauli Exclusion Principle.

The HF theory is only an approximation by definition, since it is assumed that all-electron wavefunction have a particular shape. Hence, in cases where accuracy is a concern or when there are strong electron-electron interactions, it is inferior as compared to other methods. However, at present, it is widely used in case of periodic systems.

Over the past few decades, DFT has been the most successful and widely used method in the field of Computational Condensed Matter Physics [163]. The DFT describes a many-body interacting system via its particle density and not via its many-body wavefunction. This reduces the 3N degrees of freedom of the N-body system to only three spatial coordinates through its particle density. Hohenberg and Kohn tried to formulate the DFT as an exact theory for many body systems [164]. DFT is based on the Hohenberg-Kohn theorems. These theorems basically state that the properties of the ground-state of a many-electron system are determined uniquely by the electron density (first theorem) and that this quantity can be calculated by using a variational principle (second theorem). The ground-state energy is, hence, a functional of the density. Along with the energy, all the physical properties of the system are also a functional of the density. This enormously simplifies the problem of a many-electron system.

The Hohenberg-Kohn formulation applies to a system of interacting particles in an external potential $V_{ext}(r)$, including any problem of electrons and fixed nuclei, where the Hamiltonian is given by Equation (3.1) [165],

$$\hat{H} = -\frac{\hbar^2}{2m_e} + \sum \nabla_{i^2} + \sum V_{ext}(r_i) + \frac{1}{2} \sum_{i \neq j} \frac{e^2}{(\check{r}_i - \check{r}_j)} \qquad (3.1)$$

The Hohenberg-Kohn theorems are as given below:

a) **Theorem I:** For any system of interacting particles, in an external potential $V_{ext}(r)$, the potential $V_{ext}(r)$ is uniquely determined, except for a constant, by the ground state particle density $n_0(r)$.

b) **Theorem II:** A universal functional for the energy E[n] in terms of the density n(r) can be defined. This is valid for any external potential $V_{ext}(r)$. For any given external potential $V_{ext}(r)$, exact ground state energy of the system is the global minimum value of this functional, and the density n(r) that minimizes the functional is the exact ground state density $n_0(r)$.

Hohenberg-Kohn theorem has made it possible to use the ground state density to calculate the electronic properties of the system. But it does not provide a way of finding the ground state energy. Kohn-Sham (KS) equations provide a method to determine the ground state energy. To derive the KS equations, one needs to consider the ground state energy as the functional of charge density. Kohn-Sham derived a set of single particle Schrodinger equations given by [166],

$$\left[\frac{-\hbar^2}{2m}\nabla^2 - V_{eff}(r)\right]\Psi_i(r) = \varepsilon_i\Psi_i(r) \tag{3.2}$$

Where, εi are Kohn-Sham eigenvalues, $\psi_i(r)$ are Kohn-Sham single particle orbitals.

The effective potential is given by [167],

$$V_{eff}(r) = V_{ext}(r) + V_{Hartree}(r) + V_{xc}(r) \tag{3.3}$$

Where, $V_{eff}(r)$ represents the electron-ion interaction [165]. $V_{Hartree}(r)$ represents the Hartree potential, i.e., the classical electrostatic interaction. $V_{xc}(r)$ is the exchange-correlation potential.

$V_{Hartree}(r)$ and $V_{xc}(r)$ are given as per Equation (3.4) and (3.5), respectively.

$$V_{Hartree}(r) = \int \frac{n(r')}{|r-r'|} dr' \tag{3.4}$$

$$V_{xc}(r) = \frac{\delta E_{xc}}{\delta n(r)} \tag{3.5}$$

Where, E_{xc} is the exchange-correlation energy. $V_{xc}(r)$ represents the many body effect. Approximation for the E_{xc} [165] is stated as per Equation (3.6) in Section 3.1.1.

3.1.1 LDA (Local Density Approximation)

LDA are a class of approximations to exchange-correlation energy functionals (E_{xc}) in DFT. For spin-unpolarized systems, LDA for E_{xc} is given as per Equation (3.6):

$$E_{xc}^{LDA}[\rho] = \int \rho(r) \in_{xc} (r) dr \tag{3.6}$$

Where, ρ is the electronic density and $\in_{xc}$ is the exchange-correlation energy per particle of a homogeneous electron gas of charge density ρ. In LDA, the functional depends only on the electronic density at the coordinates, where the functional is evaluated. This approximation can be used to find Eigen function and eigenvalues of the

Hamiltonian. It is commonly used along with plane wave basis set. LDA considers a functional whose functional derivative is taken with respect to density at that point only. It is an approximation to the exchange-correlation, which depends on the value of the electronic density at each point. Local approximations to the exchange correlation energy are derived from the homogeneous electron gas model (such as the Jellium model). The exchange functional can also be expressed as the energy of interaction between the electron density and the Fermi coulomb-hole charge distribution. LDA is synonymous with functionals based on the HEG approximations, which are applied to realistic systems such as large molecules and solids. The expression for energy and potential is given below [165]:

$$E_{xc}(n) = \int E_{xc}[n]n\big((\check{r})\big)d^3r \tag{3.7}$$

Where, E_{xc}=exchange-correlation energy per electron. The exchange-correlation energy is composed of two terms: exchange term and the correlation term, linearly as in Equation (3.8).

$$E_{xc}[n] = E_x + E_c \tag{3.8}$$

Where, E_x is the exchange term and E_c is the correlation term. The exchange term takes a simple analytical form for the HEG, while only limiting terms are precisely known for the correlation density. This leads to various approximations for E_c.

The exchange-correlation potential, corresponding to the exchange-correlation energy, is stated in Equation (3.9).

$$V_{xc}(r) = \frac{\delta E_{xc}(r)}{\delta n} \tag{3.9}$$

In finite systems, the LDA potential is known to decay asymptotically with exponential form. This is slightly erroneous. The true exchange-correlation potential decays much slower in a Coulombic way. The LDA potential cannot support the Rydberg series and such states are too high in energy. LDA does not provide accurate description of electron-rich anions. Therefore, LDA is unable to bind an additional electron and predicts the anionic species to be stable erroneously [168].

3.1.2 LDA+U

This approximation is an improved form of LDA. In case of transition metal or rare earth metal ions which have strongly correlated system, the LDA approximation is not sufficient to describe the electronic properties of the system. If one applies LDA to a transition metal compound, it will provide the metallic electronic structure with partial d-band, which is erroneous. Several approaches have been worked out for improving LDA to include the differences in the strongly correlated electron-electron interaction. The Hamiltonian of LDA for the case, described in Section 3.1.1, can be improved by use of the calculated self-energy in a consistent procedure.

The orbital dependent potential, taking LDA+U approximation, exhibits both the upper and lower Hubbard bands with difference of coulomb parameter U. LDA+U

approximation shows that the information obtained is not sensitive to a particular form of localized orbitals. LDA+U theory can be described as the Hartee Fock theory for localized states (orbital of rare earth metal). By using the Hubbard U term, a correction term to Hamiltonian of LDA, there is a large increase in the number of calculations for the electronic structure. The Hubbard parameter term U relates the single particle potential to the magnetic order parameter. For impurity systems, high T_c superconductors, Mott insulators, transition metals, the LDA +U approach is highly accurate. Delocalized s, p electrons can be described by using an independent one-electron potential. For localized d and f electrons, LDA, including Hubbard like term, can be used instead of averaged coulomb energy [165].

3.1.3 Quantum Espresso

It is an integrated suite of computer codes, including the plane-wave pseudo potential DFT code PWSCF. This suite is used for electronic-structure calculations and materials modeling at the nanoscale [165]. The software is released under the GNU General Public License. The full Quantum ESPRESSO distribution contains the following core packages for the calculation of electronic-structure properties within Density-Functional Theory (DFT), using a Plane-Wave basis set and pseudopotentials:

- PWSCF (PW) : Plane-Wave Self-Consistent Field,
- CP (CPV): Car-Parrinello Molecular Dynamics.

It is based on Density Functional Theory (electron-ion interaction), plane waves, and pseudo potentials (both norm-conserving and ultrasoft for electron-electron interactions). In DFT, for a given periodic system, by determining the electronic states, one can

evaluate the thermal, optical and magnetic properties of solids, equations of state, electron density distributions and cohesive energies of the system.

DFT has become a very widely-used method in computational physics and computational chemistry research for determining the electronic structures of many-body systems, such as atoms and molecules. It has been particularly applied in the condensed state. PWSCF is a method used to calculate bandstructures by expanding wavefunctions into plane waves. Various auxiliary packages are also included along with the codes. PWgui is Graphical User Interface, which produces input data files for PWSCF. Several additional packages which can use the PWSCF data as input for post-processing have been included.

3.1.4 Pseudopotential

It is a modified effective potential term instead of coulombic potential term in Schrödingers' equation for core electrons. The information about the type of exchange correlational functional and the type of pseudopotential can be found from the literature [167]. Pseudopotential is an effective potential constructed in order to replace the atomic all-electron potential such that the core states are eliminated and valence electrons are described by pseudo-wavefunctions with significantly lesser nodes. In pseudopotential, the Kohn Sham's radial equation is considered. It contains the contribution from valence electrons.

Pseudopotentials with larger cut-off radius are considered to be softer. However, they are found to be less accurate in different environments. Thus, the motivation in using pseudopotentials is to reduce the size of basis sets, reduce the number of electrons, and include relativistic (and other) effects. There are two types of pseudopotentials i.e.,

ultrasoft pseudopotential and norm-conserving pseudopotential used in modern plane-wave electronic structure codes. These methods make it possible to consider basis sets with significantly lower cut-off (the frequency of the highest Fourier mode). These basis sets can be used to describe the electron wavefunctions. Thus, proper numerical convergence can be achieved with less computing resources [169].

3.1.5 Xcrysden

It is a molecular and crystalline-structure visualization program for input and output files generated by PWSCF. Its principle function is to serve as a property analyzer program. It can run on most UNIX platforms, without any specific hardware or software requirements. Special efforts have been made to allow appropriate display of 3D iso-surfaces and 2D contours. XCrysDen is also a graphical user interface for some other software codes such as CRYSTAL. It can perform real-time operations such as rotation and translation. It can be used for measuring distances, angles, dihedrals for a given crystal lattice.

3.2 Emissivity Calculations

Multi-Rad software is the modeling tool which has been used in our simulations of the radiative properties of thin-film stacks. In Multi-Rad, the thin film optics is implemented in the form of the matrix method of multilayers. The model assumes the following: (a) the layers are optically smooth and parallel, as well as the materials are isotropic; and (b) constancy of the properties in azimuthal direction. For a given multilayer stack, it is possible to calculate the radiative properties as a function of wavelength and angle of incidence, at a specific temperature [170]. In Multi-Rad, a material can be defined using

its refractive indices, n, and extinction coefficients, k. Most of the parameters in this study have been based on data from references [171-173].

The matrix method of multilayers can predict the reflectance and transmittance of a multilayer stack for a specific wavelength and angle of incidence. For a specific wavelength, the coherent radiation is considered. This enables consideration of the interference effects. Most important assumptions of this theory is that the surface area on which the radiation is incident is much larger than the wavelength of the incident radiation i.e., there are no edge effects [174]. The detailed description of the matrix method of multilayers can be obtained in reference [170].

The spectral absorptance is a directional property and it can be calculated by subtracting the reflectance and transmittance from unity, and the spectral emittance can be calculated by assuming Kirchhoff's law on a spectral basis:

$$\alpha_{\lambda,\theta} = \varepsilon_{\lambda,\theta} = 1 - R_{\lambda,\theta} - T_{\lambda,\theta} \tag{3.10}$$

Where, the subscripts are introduced to indicate spectral and directional properties, respectively. Spectral directional reflectance and transmittance are denoted respectively as $R_{\lambda,\theta}$ and $T_{\lambda,\theta}$. They are calculated from the average of *s* and *p* wave properties. If it is assumed that a given emitter is in local thermodynamic equilibrium, Kirchhoff's law can be considered as valid on a spectral basis. It is characterized by a single temperature. In cases where there are high gradients of temperature across the emitting wafer, or where the electrons and phonons are not in local thermal equilibrium, Kirchhoff's law is not valid.

3.3 Theory of Atomistic Simulation

Atomistic simulation refers to a suite of computational techniques which are used to model the interaction and configuration of a system of atoms. In this work, the term 'atomistic simulation' will pertain to molecular dynamics. Detailed and comprehensive reviews of 'atomistic simulation' can be found in books by Allen and Tildesley [175] and Haile [176].

Atomistic simulations are commonly classified into two categories: equilibrium and non-equilibrium [176]. In equilibrium atomistic simulations, the system is completely isolated from its surroundings with a fixed number of atoms, volume and constant total energy. These boundary conditions are considered to be corresponding to the microcanonical (NVE) ensemble in statistical mechanics [177]. In non-equilibrium atomistic simulations, the system is allowed to interact with the surrounding environment through either thermal or physical constraints (such as a thermostat or an applied force). Depending on the equations of motion which describe the system of atoms, these calculations may correspond to the canonical, either NVT (Ensemble with a constant number of particles (N) of the system, Volume (V) and Temperature (T)) or NPT (Ensemble with a constant number of particles (N) of the system, Pressure (P) and Temperature (T)), in statistical mechanics. Many different methods exist to specify the interaction between the atomic system and the environment. All of them are considered as non-equilibrium MD methods.

In the atomistic framework, each atom is represented as a point mass in space while the interatomic potential provides a model for the potential energy of a system of atoms. Commonly, the total potential energy of the system is written solely as a function

of the positions of the atomic nuclei. This simplification avoids having to specifically account for the motion and interaction of the individual electrons. Since interatomic forces are conserved, the force on a given atom, F^i , is related to the interatomic potential, U , through the gradient operator, i.e.,

$$F^i = -\frac{\partial U(r_N)}{\partial r^i} \tag{3.11}$$

Where, 'r' is the atomic position vector. In this work, superscripts denote variables assigned to individual atoms, while subscripts denote variables associated with sets of atoms, directions or at specific time steps. Thus, $\boldsymbol{r_N}$ represents the position vectors for the system of N atoms while 'r^i' is the atomic position vector for the i^{th} atom. One of the inherent limitations of the atomistic method is extremely high expense of computational resources. This makes it essential to limit the systems to relatively small numbers of atoms. The studies of nanoscale surface effects that are related to length scale are extremely important. The goal of this work is to examine atomic scale behavior which can represent a bulk sample with micro or nanoscale grain structure. Thus, periodic boundary conditions are used in many of these calculations for eliminating the influence of free surface effects. As shown in Figure 3.1, we consider a two-dimensional example of using periodic boundary conditions in the atomistic framework. The primary cell is outlined with solid lines and it represents a small portion of the material. The atoms which lie within this cell are explicitly modeled using atomistic methods. The bordering 'image' cells, which are shown with dashed lines in Figure 3.1, represent the infinite

repetition of the primary cell in two dimensions. With this method, it is possible to model an infinite amount of material in each direction.

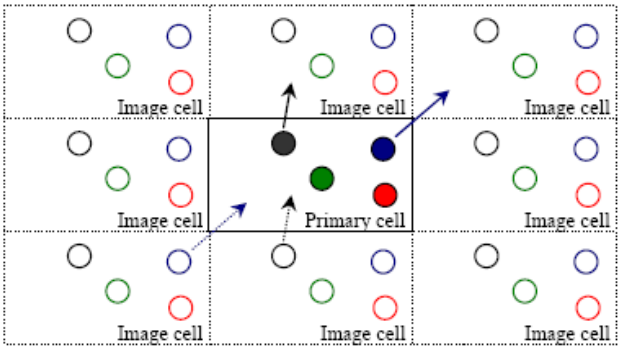

Figure 3.1: Two-dimensional illustration of periodic boundary conditions in the atomistic framework.

Suppose blue atom in the primary cell moves to a point outside of this region during the simulation, as shown with a solid blue arrow in Figure 3.1. The image of this atom will be reflected back into the primary cell on the opposite side with the same momentum, as shown with the dashed blue arrow. Note that the atoms that lie near the borders of the primary computational cell can interact with neighbor atoms across the periodic boundary. While periodic boundary conditions remove the effects of free surfaces, they are imparting image constraints on the system which must be taken into consideration when simulating defect behavior with long-range interactions.

The atomistic code, used in this thesis, is classical molecular dynamics code LAMMPS, which stands for Large-scale Atomic/Molecular Massively Parallel Simulator. LAMMPS was written by Steve Plimpton at Sandia National Laboratories / Albuquerque, NM. LAMMPS has potentials for soft materials (biomolecules, polymers) and solid-state materials (metals, semiconductors) as well as coarse-grained systems. It can be used to

model atoms or, more generically, as a parallel particle simulator at the mesoscale or even upto the continuum levels [178].

LAMMPS runs on single processor or in parallel using message-passing techniques. It performs a spatial-decomposition of the simulation domain. The code is designed to be easy to modify or extend for better functionalities. LAMMPS is distributed as an open source code under the terms of the GPL. LAMMPS is distributed by Sandia National Laboratories, a US Department of Energy laboratory. The code is written in C++. This MD code is capable of performing molecular dynamics simulations in the microcanonical (NVE), constant volume canonical (NVT) ensembles and also the isothermal-isobaric ensemble NPT. The latest stable version of LAMMPS is 28 June 2014 and has been used in simulations performed in this thesis.

3.3.1 Molecular Dynamics

In the molecular dynamics method, the evolution of atomic positions is described using Newton's second law of motion,

$$p^i = F^i = mv^i \tag{3.12}$$

$$r^i = \frac{dr^i}{dt} = \frac{p^i}{m} \tag{3.13}$$

Where, m denotes the mass, p^i is the momentum and v^i is the velocity of the i^{th} atom. The most widely used method to solve the above equations in molecular dynamics is the "Velocity-Verlet finite-difference" algorithm [179]. This algorithm has been applied because its form is exactly time reversible. This allows the equations of motion to

be propagated forward in time without iteration and symplectic, i.e., the volume in phase space is conserved. Thus, one can ensure stability and convergence of simulation for a bigger atomic system.

While the study of material behavior in isolated systems has merit, the vast majority of problems in mechanics and materials science require consideration of interaction of the system with the surrounding environment (non-equilibrium molecular dynamics). One way to accomplish this, in molecular dynamics, is to introduce the concept of an extended system [180]. Essentially, Newton's equations of motion are augmented and coupled to additional differential equations which can describe the relationship between the system and the environment. Commonly, molecular dynamics calculations are performed at a constant temperature or pressure (or both).

Of course, accurate evaluation of the thermodynamic quantities makes it essential to consider the size of the atomistic system. The use of periodic boundary conditions in the atomistic framework serves as an effective way to approximate the thermodynamic limit.

3.3.2 Input File Parameters in MD Simulation Using LAMMPS

a) Initialization

One has to define the initial configuration of the system as per literature. The dimensionality, boundary condition (periodic or fixed), atomic positions, timesteps, unit cells and simulation box size are the parameters that need to be set for the material being analyzed.

b) Force Field Implementation

Interactive potential needs to be defined in a system. A suitable empirical potential has been chosen as a function of time. Tersoff potential has been chosen to model graphene. This potential has been shown to be successful in describing atomic interactions for Carbon.

c) Prescribing Ensemble and Running Simulation

Before running an actual simulation, a thermalization process needs to be performed so that the system is in thermal equilibrium – the system is in thermal equilibrium at minimum energy. The ensemble is essential to perform this operation. In order to equilibrate the system, microcanonical ensemble (NVT) is designed using Nose-Hoover thermostat. It performs time integration on Nose-Hoover style and is based on non-Hamiltonian equations of motion which are designed to generate positions and velocities. This is achieved by adding some dynamic variables which are coupled to the particle velocities (thermostatting). When used correctly, the time-averaged temperature of the particles will match the target values specified.

3.3.3 Thermal Transport in Graphene

In recent years, electronic devices are becoming smaller. The interface of materials is becoming increasingly important in the determination of their thermal properties. This is especially true in case of nanoscale materials where the interface thermal resistance significantly affects their overall thermal conductivity. As the thermal management in electronic devices is a prime concern, the role of materials which are widely used in electronic devices such as carbon nanostructures, silicon based materials and the interface between these materials is becoming increasingly important. In this thesis, the method of

molecular dynamics simulations is used for calculations of thermal conductivity of graphene and its derivatives.

The thermal conductivity of graphene is very hard to be determined experimentally [6]. Hence, its thermal conductivity has been mostly predicted from theoretical methods. Experiments performed by Alexander et al. [144] show the thermal conductivity of graphene to be in the range of ~4,840 W/mK to ~5,300 W/mK. It is even higher than CNT. Several models have been successfully tested to investigate the thermal conductivity of graphene and graphite. Nika et al. [181] determined the thermal conductivity through phonon dispersion and they found the values to be in the range of 2,000 W/mK to 5,000 W/mK with varying flake size of graphite. Lan et al. [182] determined the thermal conductivity through Green-Kubo function and found the values of ~ 3,410 W/mK. Baladin et al. [183] performed experiments to calculate the thermal conductivity of single layer graphene as ~4,200 W/mK, while graphite has thermal conductivity of ~2000 W/mK. NEMD technique is applied in this simulation of thermal conductivity.

NEMD simulation has been implemented in this thesis to obtain the temperature gradient resulting from the swapping of kinetic energy. The thermal conductivity, κ, is then calculated from the Fourier law:

$$\kappa = \frac{-J}{(\Delta T.\ \lambda)} \tag{3.14}$$

Where, ΔT is the gradient of the temperature, J is the heat flux from the heat bath to the system and λ is the total kinetic energy transfer between slabs. λ is defined as:

$$\lambda = \frac{\sum transfers \frac{m}{2}(v_h^2 - v_c^2)}{2tL_xL_y < {}^{\partial T}/_{\partial z} >} \tag{3.15}$$

The subscript ‘h’ refers to the hot particles and subscript ‘c’ refers to the cold particles of identical mass ‘m’. The velocities of these particles are interchanged. L_x and L_y are cross sectional area of simulation box. The factor of two in denominator is used to denote heat flow in two directions of the slabs, effectively doubling the area of heat flux. The term T/z is the temperature gradient obtained from the average of the ensemble.

Equation (3.15) is used to find the thermal conductivity of graphene and its derivatives. This Müller-Plathe technique is used to apply heat to the system. This is different from the Green-Kubo method [184]. This technique is sometimes called as reverse non-equilibrium molecular dynamics (R-NEMD). This is because the usual NEMD approach is to impose a temperature gradient on the system and measure the response as the resulting heat flux. In the Müller-Plathe method, the heat flux is imposed, and the temperature gradient is the system's response. The schematic diagram of the Müller-Plathe method is shown in Figure 3.2.

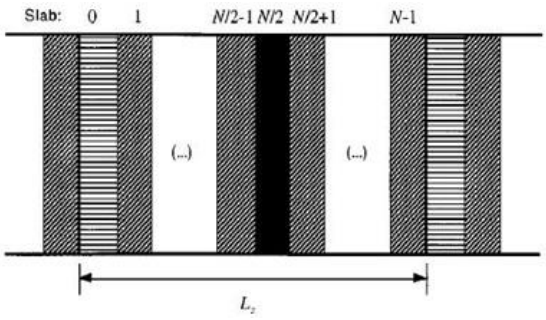

Figure 3.2 Müller-Plathe method, SWNT has been differentiated into several slabs [184].

The basic principle of the Müller-Plathe method is that the whole system is to be divided into slabs along the axial direction, and the temperature of each slab is calculated by the following statistics:

$$T_k = \frac{1}{3n_k k_B} \sum_{i \in_k}^{n_k} m_i v_i^2 \tag{3.16}$$

In this technique, the first layer is assumed as the cold slab, while layer N/2 (middle layer) is simulated as a hot slab. The hottest atom having maximum kinetic energy exchanges its energy with the adjacent atoms till the heat energy reaches to the end of cold slab (one with minimum kinetic energy). The temperature gradient between the atoms and the distribution of kinetic energy of atom is very broad. Hence, the hottest atom at cold slab always has higher kinetic energy than coldest atom at hot slab. The linear momentum and energy of the system is conserved, if the mass of the swapping atoms remain the same. However, the angular momenta of the atoms are not conserved. This is not a problem since the introduction of periodic boundary to the system allows the angular momentum to be neglected.

The Müller-Plathe algorithm is relatively easy to implement, as well as to keep the system linear momentum; the total kinetic energy and total energy conserved, and does not require an external heat bath. However, the Müller-Plathe method assumes that the cold slab and hot slab exchange of atomic mass are equal.

3.4 Boltztrap

The simulation of electronic transport quantities such as Seebeck coefficient, electrical conductivity and electronic thermal conductivity has been performed using a modeling code known as BoltzTraP. BoltzTraP uses a Fourier sum to evaluate energy bands, where spacegroup symmetry is maintained by using star functions. This provides a simpler basis for the integrations in order to obtain the transport coefficients. The idea of the Fourier expansion is to use more star functions than band energies, but to constrain the fit so that the extrapolated energies are exactly equal to the calculated band-energies and use the additional freedom to minimize a roughness function. Thus, it is possible to suppress oscillations between the data-points. Since energy bands are given as Fourier sums, their derivatives yield the velocities and their second derivatives yield the curvature or inverse effective masses. All these quantities appear in the Fermi integrals for calculating transport coefficients.

Under the assumption that the relaxation time τ is direction independent, both the Seebeck and Hall coefficients are independent of τ. As the interpolated bands pass through the calculated band-energies, the precision of this method is mainly limited by possible band crossings. At these band crossing locations, the band derivatives will be calculated wrongly. The method has been successfully tested for calculating transport coefficients of intermetallic compounds, high T_c superconductors and thermoelectrics.

The idea of this procedure was developed in 1986 by Koelling and Wood [185]. However, it was implemented into code for solving the Boltzmann equation by the work of Madsen and Singh in 2006 [186]. BoltzTraP only calculates electronic transport coefficients depending on the chemical potential, i.e., charge carrier densities and

temperature. Only an energy independent and direction independent relaxation time is assumed so far. Transport coefficients of phonons are not calculated. BoltzTraP operates in three spaces: real space, k space and energy space. Particularly important is the transfer from k space to energy space via the density of states.

CHAPTER 4

MODELING & SIMULATION

This section has been divided into four sub-sections based on the properties of graphene and its functional derivatives analyzed.

4.1 Electronic Properties

Graphene is known to have relaxed 2-D honeycomb structure (Figure 1.2) and the doped graphene will be assumed to have similar structure, unless violated by energy minimization considerations. The optimizations of the lattice constants and the atomic coordinates are made by the minimization of the total energy. A sample of graphene nano-structure analyzed has been shown in Figure 4.1.

The following steps and methodology have been used for simulating the various graphene based nanostructures:

1. Setting up structure by inputting coordinates. VMD (Visual Molecular Dynamics) software [187] has been used for generating input structure of graphene nanoribbons. An open source code "latgen" has been used for obtaining coordinates of graphene nanosheets and its derivatives.

2. Performing Self consistent (SCF) simulation of graphene nanostructure to obtain minimum total energy configuration.

3. Performing non-SCF calculation by varying energy cutoff, Monkhorst-Pack grid parameters and lattice constant.

4. Repeating the simulation till obtaining the lowest energy configuration in terms of energy, k-points as well as lattice constant.

5. Kinetic energy cutoff for wavefunctions has been chosen as 70 Ry, while the kinetic energy cutoff for charge density and potential has been set as 840 Ry (as a rule, it should be 8-12 times the kinetic energy cutoff for wavefunctions). It is noted that the total energy of the system is minimum at this cutoff.

6. Smearing with degauss 0.03 has been used in considering the semi-metallic nature of graphene.

7. Energy convergence parameter has been set as 1.0E-8 Ry i.e., system converges once it reaches this energy level.

8. Path for plotting bandstructure has been chosen as G, M, K, G.

Figure 4.1 shows the simulated graphene nanostructures. These structures have been modeled using VMD software.

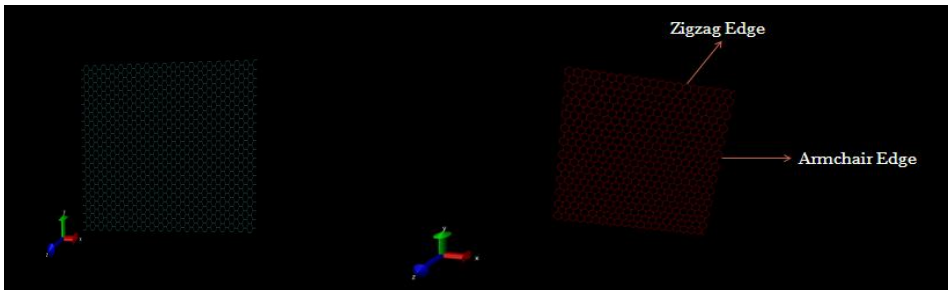

(a) (b)

Figure 4.1 Simulated structure of (a) Graphene nanosheet, (b) Graphene nanoribbon.

Once the verification of the model is established by comparison with the literature (experimental or simulated), the model is then extended to simulate the properties of graphene as function of orientation, number of layers, doping, vacancies etc.

4.1.1 Bandstructures

A. Undoped Graphene

As seen in Figure 4.2, the Dirac point is located on K and the Fermi level is present at energy 0 eV. Thus, it is observed that undoped graphene behaves as a semi-metal.

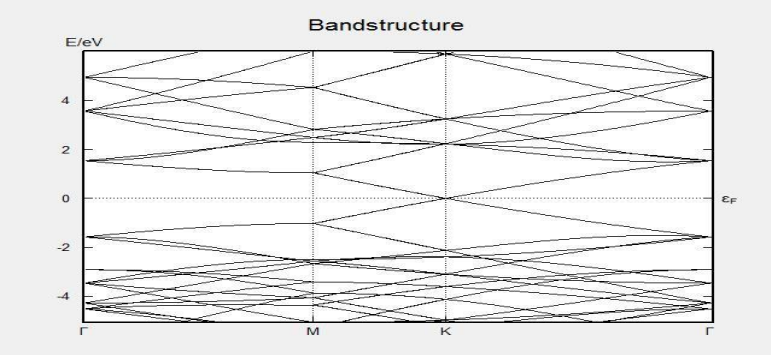

Figure 4.2 Bandstructure of undoped graphene.

B. Boron Doped Graphene

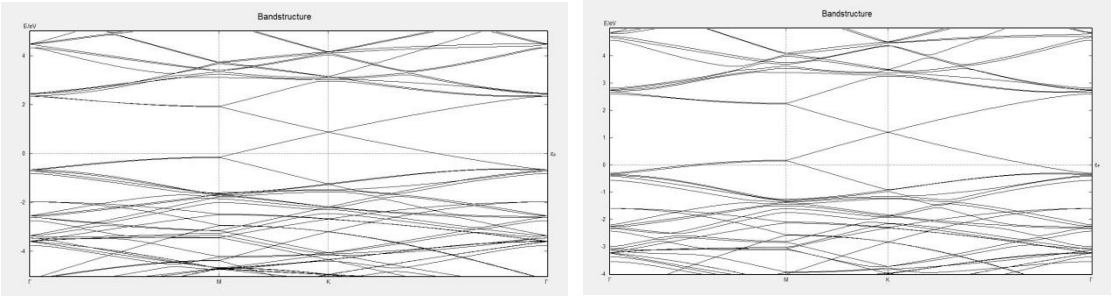

(a) (b)

Figure 4.3 Bandstructure of (a) 2% boron doped graphene and, (b) 4% boron doped graphene.

Upon boron doping, it is observed that the Fermi level is shifted below the Dirac point in graphene. The boron atoms adjust themselves to the surrounding host carbon atoms. When graphene sheet is doped with boron atoms, the boron atoms also undergo sp^2 hybridization. Due to similar size of carbon and boron atoms, there is no significant distortion in the structure of graphene, except for change in adjoining bond length. Doping induces bandgap in graphene. The variations of bandstructure are shown in Figure 4.3. Due to electron deficient nature of boron, it is noted that the Fermi level moves about 1-2 eV below the Dirac point. This is evident from the bandstructures and shows that boron is a p-type dopant in graphene.

C. Nitrogen Doped Graphene

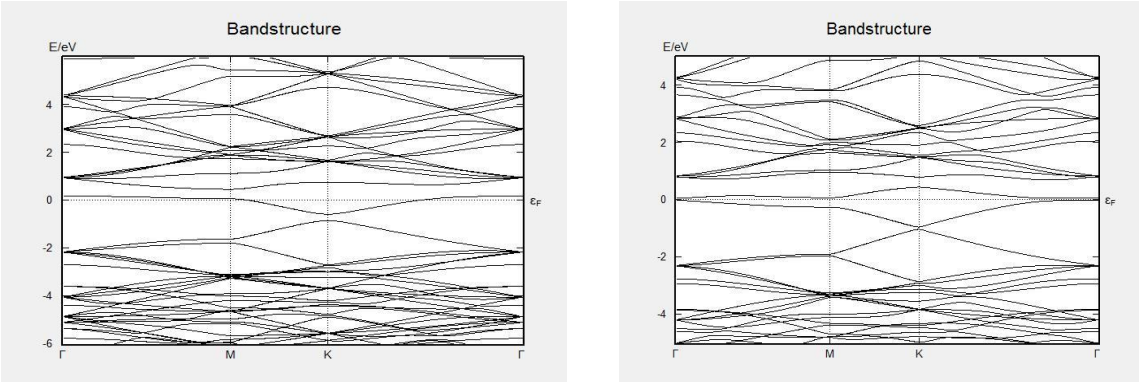

(a) (b)

Figure 4.4 Bandstructures of (a) 2% nitrogen doped graphene and, (b) 4% nitrogen doped graphene.

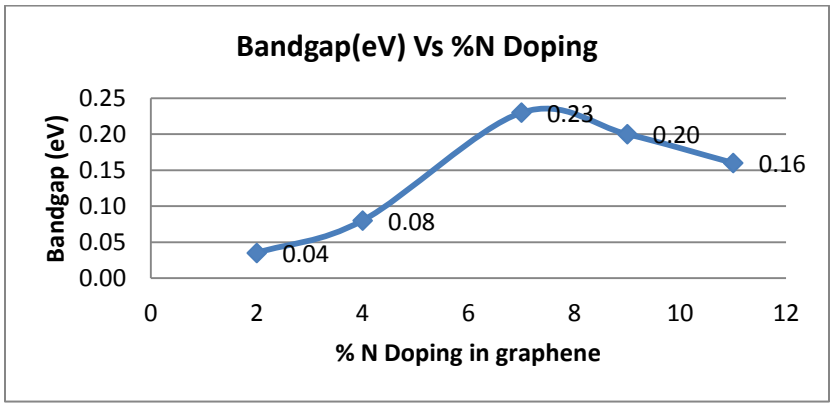

Figure 4.5 Bandgap versus % nitrogen doping in graphene.

Figure 4.4 shows the bandstructure trends by nitrogen doping of graphene. Figure 4.5 shows the trends of bandgap as a function of % nitrogen doping in graphene. It is evident from the study that nitrogen is an n-type dopant in graphene, as the Fermi level moves significantly above the Dirac point with increasing nitrogen doping. This also shows the electron-rich character of nitrogen as a dopant for graphene. It is known that the bandgap results due to breaking of symmetry in graphene sub-lattices. Hence, increasing the dopant concentration in graphene is expected to modify the bandgap in all

the cases. However, it is found that the nature of bandgap versus % nitrogen doping is not uniform and it has a peak at about 8% nitrogen doping in graphene.

4.1.2 Trends in Density of States (DOS)

A. Pure Single Layer Graphene

Figure 4.6 shows changes in the DOS of graphene computed using energy dispersion [73]. It is seen that the DOS is nil in the proximity of charge neutrality point (CNP) for graphene. Its zoomed-in view is shown in the figure on the right.

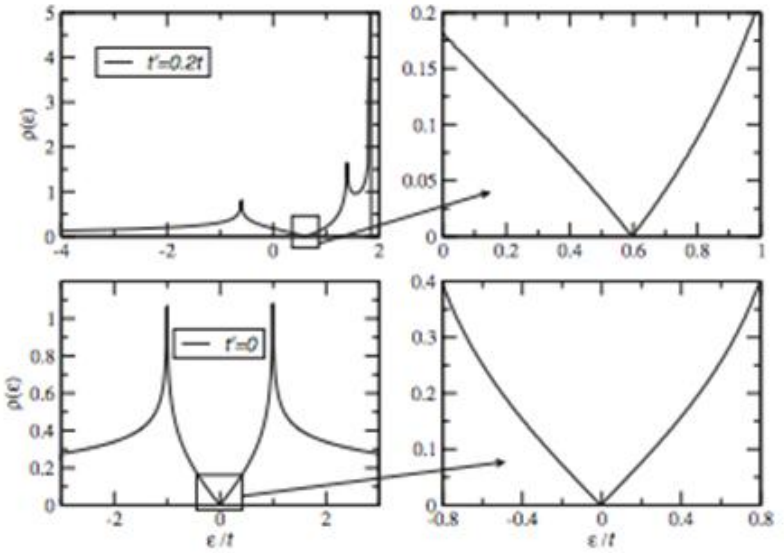

Figure 4.6 DOS per unit cell as a function of energy (in units of t) computed from energy dispersion, with two different values of t' and the zoomed-in view of density of states close to the neutrality point of one electron per site [73].

Figure 4.7 shows the density of states calculated for pristine graphene. It is found to exhibit the peculiar nature of graphene with nil DOS at the CNP, as compared with the literature.

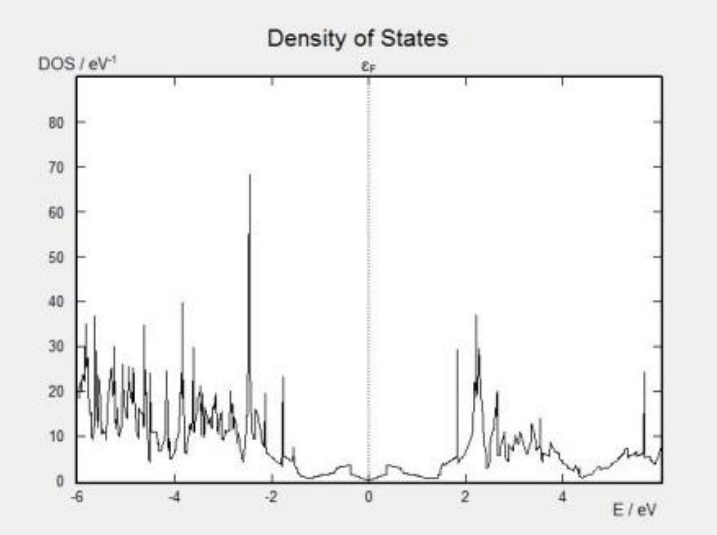

Figure 4.7 DOS for pristine single layer graphene, based on simulations.

B. Boron Doped Graphene

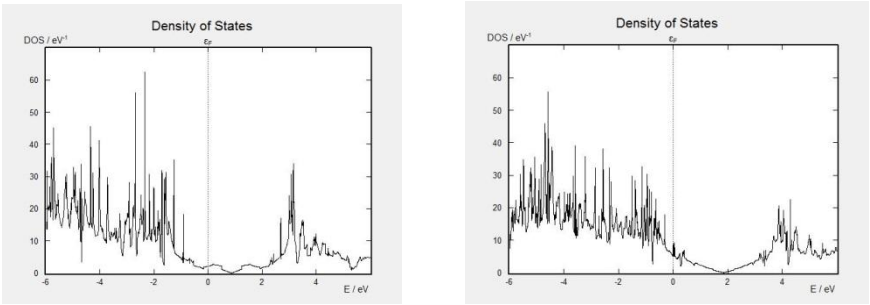

(a) (b)

Figure 4.8 DOS of (a) 2% boron doped graphene and, (b) 11% boron doped graphene.

Figure 4.8 shows the variations in the DOS for varying % boron doping. The shift in the Dirac point from Fermi level can be observed. The point with nil DOS is found to shift from about 0.7 eV for 2% boron to about 1.8 eV for 11% boron doping in graphene. Similar studies have also been done for nitrogen doping in graphene.

4.2 Optical Spectrum

4.2.1 Pure Graphene

Figure 4.9 shows the trends in dielectric constant as per simulations. This is comparable with the literature, as in Figure 2.10. Figure 4.9 (a) shows the real part, with peaks at about 4.9 eV and 14.6 eV, which is also predicted experimentally. Figure 4.9 (b) shows the imaginary part of the dielectric constant for pristine graphene. It also exhibits peaks at 4.9 eV and 14.6 eV while it displays a valley between the two peaks.

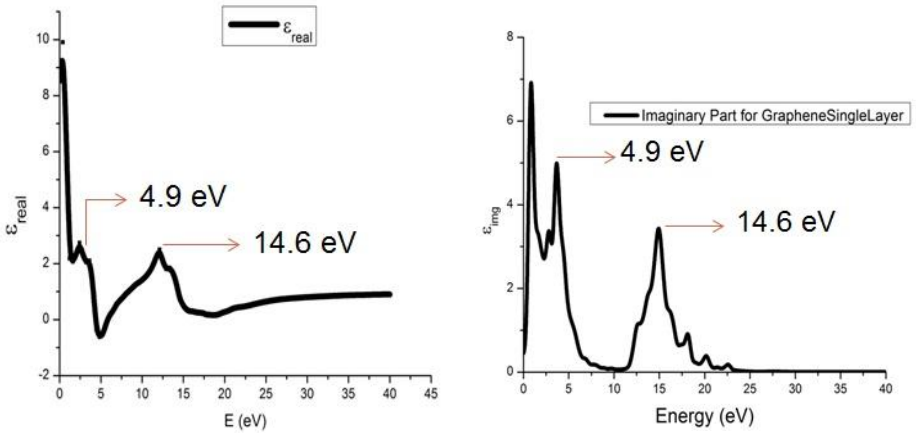

(a) (b)

Figure 4.9 Optical spectrum of pristine graphene showing (a) real and, (b) imaginary component of dielectric constant, as per our simulations. Peaks are observed at about 4.9 eV and 14.6 eV corresponding to $\pi \rightarrow \pi^*$ and $\sigma \rightarrow \sigma^*$ interband transitions, respectively.

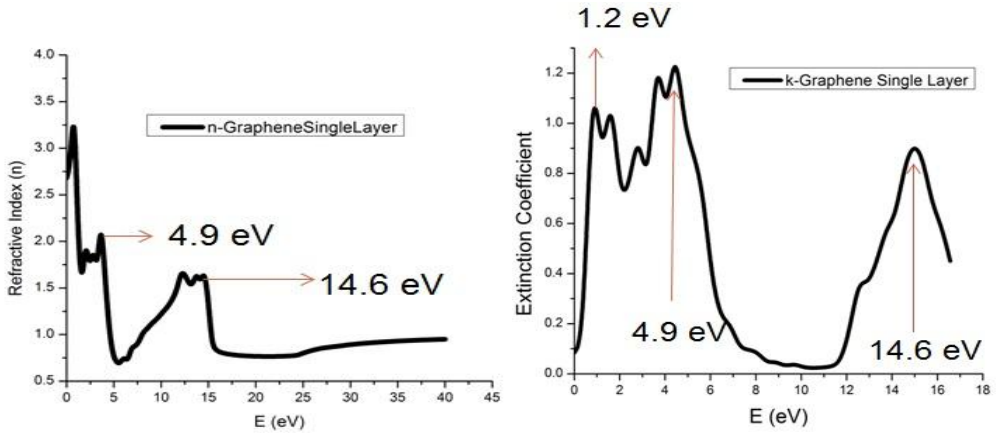

(a) (b)

Figure 4.10 Simulated (a) Refractive Index and, (b) Extinction Coefficient of pristine graphene. Peaks are observed at about 4.9 eV and 14.6 eV corresponding to $\pi \rightarrow \pi^*$ and $\sigma \rightarrow \sigma^*$ interband transitions, respectively.

Figure 4.10 shows the refractive index and extinction coefficient for pristine graphene. Peaks are observed at the same positions, as in the previous cases. It can be observed that the dielectric constant of graphene has an anisotropic nature.

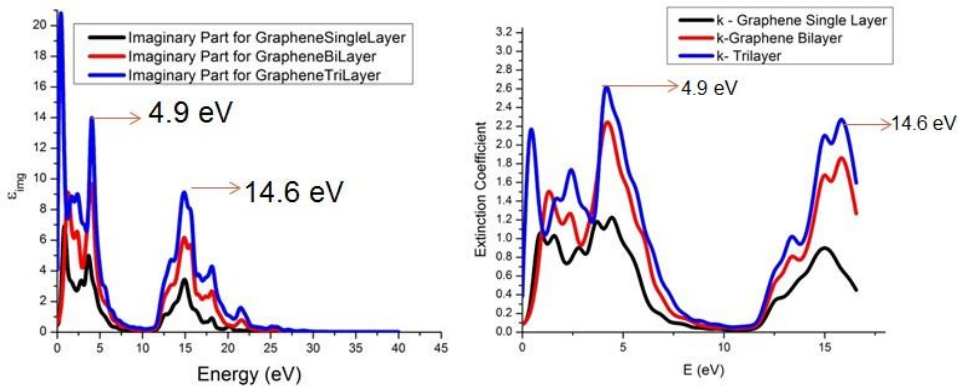

(a) (b)

Figure 4.11 Comparison of (a) Simulated imaginary parts of dielectric constant and (b) Simulated extinction coefficients for single, bilayer and trilayer graphene. Peaks are observed at about 4.9 eV and 14.6 eV corresponding to $\pi \rightarrow \pi^*$ and $\sigma \rightarrow \sigma^*$ interband transitions, respectively.

Figure 4.11 shows the comparison of imaginary part of dielectric constant for layered graphene configuration. It is observed that the curves have the peaks of higher intensity with increasing number of layers. This can be understood from the increase in absorbance with increase in number of layers of graphene.

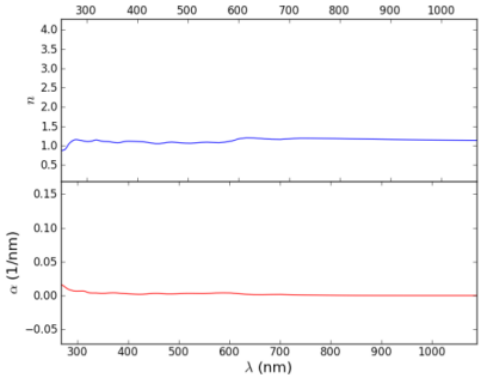

Figure 4.12 Refractive index and optical absorption spectra of graphene monolayer as a function of wavelength from 300-1000 nm, based on simulations.

Figure 4.12 shows the variation of refractive index (top) and optical absorption (bottom) spectra of graphene monolayer as a function of wavelength. It can be observed that it is independent of wavelength in the range of 300-1000 nm.

4.2.2 Boron Doped Graphene

The static dielectric constant of graphene increases significantly with increase in boron doping. The variation is seen in Figure 4.13.

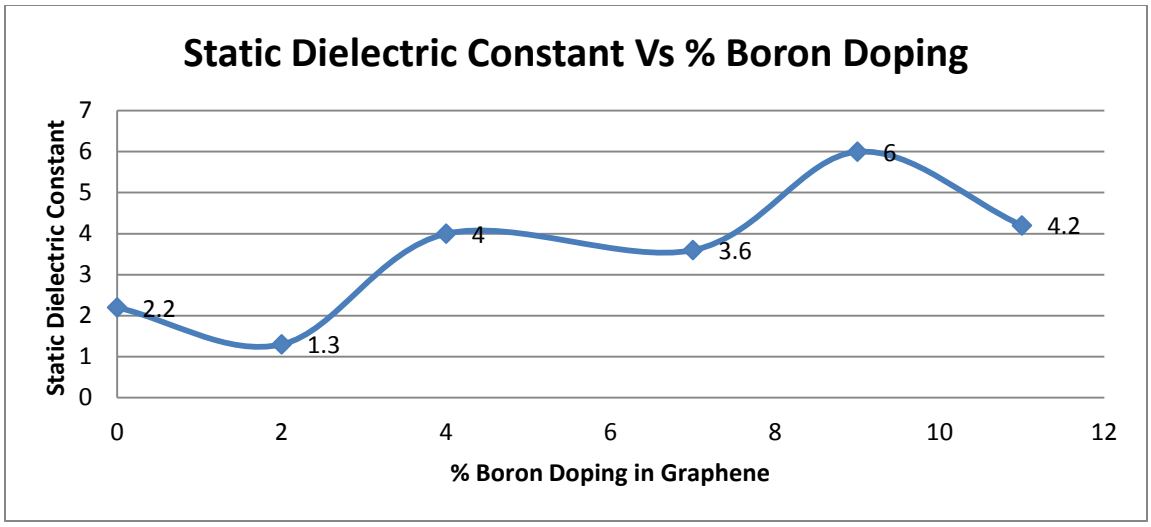

Figure 4.13 Static dielectric constant versus % boron doping in graphene, based on simulations.

4.2.3 Nitrogen Doped Graphene

The variation of static dielectric constant with nitrogen doping in graphene is shown in Figure 4.14.

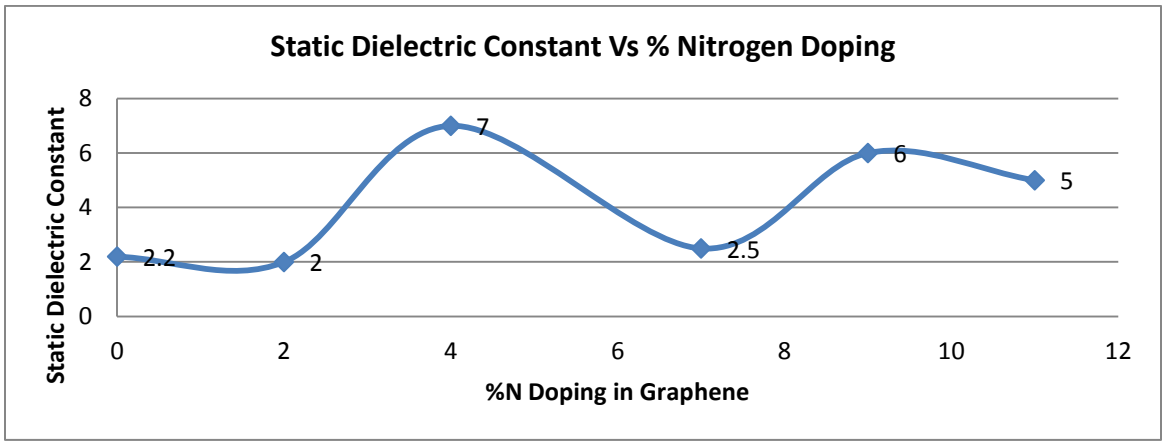

Figure 4.14 Static dielectric constant versus % nitrogen doping, based on simulations.

4.3 Mechanical Properties

Graphene has been reported to exhibit extremely high elastic modulus and hardness. In this study, the mechanical properties of graphene have been evaluated as a function of layers.

The simulation model consists of circular graphene sheet of diameter 16 nm. The simulation cell is relaxed until a little energy drift is observed. After achieving equilibrium configurations, nanoindentation is performed. Here, the circular sheet of atoms, surrounding the graphene sheet, has been fixed. Indenter is considered to be spherical and has diamond-like properties. The diameter of the indenter is considered as 25 Å. The force constant of the indenter is 1 keV/ Å.

A detailed analysis of Oliver-Pharr method to determine the elastic modulus from the load versus displacement curves is presented by Kan et al. [188]. The Oliver-Pharr method begins by fitting the unloading portion of load-displacement curve to power-law relation as shown below:

$$P = \alpha\, m\, (h - h_f) \tag{4.1}$$

Where, 'α' and 'm' are the fitting parameters. Originally, h_f is meant as the final depth after completion of unloading. However, practically when Oliver-Pharr method is used, h_f becomes only a fitting parameter.

The slope of unloading curve at maximum indentation depth is known as "Contact Stiffness" (S). The contact depth of spherical indentation, h_c, can be determined using the Oliver-Pharr method in accordance with the following equation:

$$h_c = h_m - 0.75\frac{P_m}{S} \tag{4.2}$$

Where, h_m is the maximum indentation depth and P_m is the load at maximum indentation depth. The contact area, A_c, can be computed directly from the contact depth h_c and the radius of the indenter tip R:

$$A_c = \pi(2Rh_c - h_c^2) \tag{4.3}$$

The contact stiffness, S, and the contact area, A_c, can be used to calculate the reduced modulus, as per the following equation:

$$E_r = \frac{\sqrt{\pi}}{2\beta}\frac{S}{\sqrt{A_c}} \tag{4.4}$$

Where, β is a dimensionless correction factor. It accounts for the deviation in stiffness from the lack of axisymmetry of the indenter tip with β=1.0 for axisymmetric indenters, β=1.012 for a square-based Vickers indenter, and β=1.034 for a triangular Berkovich punch [189]. For spherical indentations, β is taken as unity in this work.

Wang et al. [190] have used molecular dynamics simulations to emulate the nanoindentation experiments for some single-layer rectangular graphene films with four clamped edges. The obtained typical load versus displacement curves are shown in Figure 4.15. The effects of indenter radii, loading speeds and aspect ratios are discussed.

The Young's modulus of single layer graphene films has been found to be 1 TPa and its yield strength is reported to be 200 GPa.

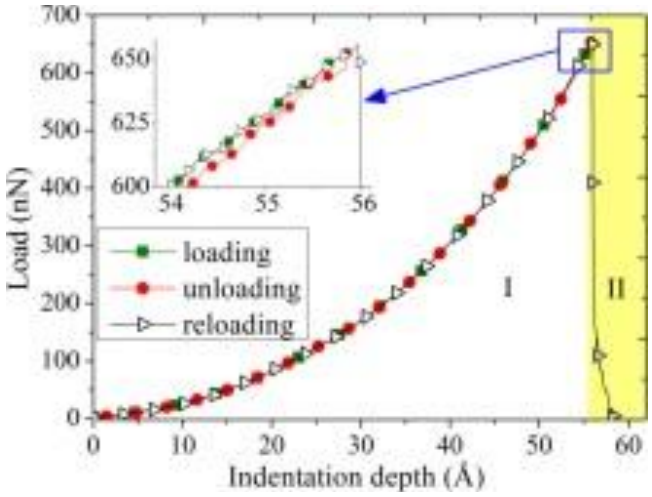

Figure 4.15 Load versus indentation depth with maximum indentation depth smaller than critical indentation depth [190].

Graphene film is ruptured at a critical indentation depth. Figure 4.16 shows the loading-unloading-reloading process with depth less than the maximum indentation depth. The indenter considered is diamond, so that there is no atomic configuration of the indenter. Researchers have used energy function as described by adaptive intermolecular reactive empirical bond-order potentials to describe the interatomic interactions in carbon atoms of graphene layer. In performing MD simulations, canonical (NVT) ensemble is used and temperatures are controlled to within 0.01 K. In order to control the interatomic thermal fluctuations, Nose-Hoover method is used with a timestep of 1 fs. Energy minimization is performed initially and the system is allowed to relax to the lowest energy configuration before indentation.

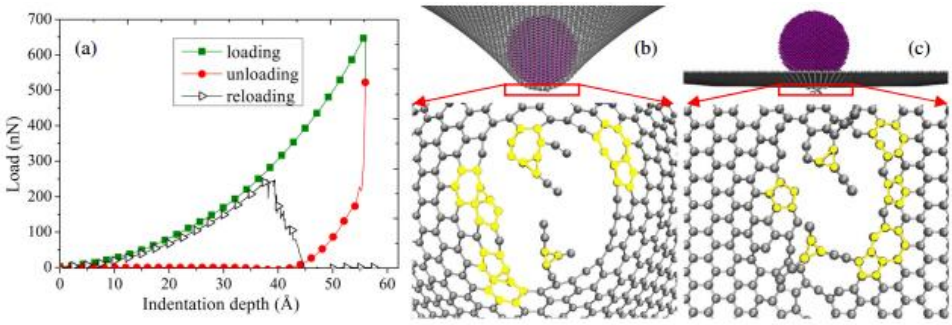

Figure 4.16 Loading-unloading-reloading process with the maximum indentation depth smaller than the critical indentation depth. (a) Load–displacement curve, (b) Local atom configuration when the loading process is finished, (c) Local atom configuration when the unloading process is finished, as per literature [190].

The formation of dislocations in graphene has been described in detail in references [191, 192]. They have mainly focused on the tensile deformation and shear deformation [193]. Most of the references in the literature are using Density Functional Theory (DFT), Tight-Binding Molecular Dynamics (TBMD), and ab initio total energy calculations. Studies show the creation of dislocations and defects, followed by the study of their effects on the properties of graphene. Very few experimental investigations, to study dislocation activities, have been published about graphene, till date [190]. Warner et al. have reported observation of dislocations in graphene using HRTEM for the experiments. Edge dislocations are shown to result in substantial deformation of atomic structure of graphene with bond compression or elongation of ±27%, along with shear strain and rotations of lattice.

4.4 Thermal Conductivity Calculations

Thermal conductivity calculations have been performed with LAMMPS software, as discussed in the previous chapter. Following steps are followed for the simulation:

1. Periodic boundary conditions have been considered in the direction of width and length.

2. Tersoff potential has been used to describe interatomic interactions for C, B and N atoms.

3. Neighbouring atom cutoff distance for force calculations is considered as 2Å.

4. Conjugate gradient algorithm, used for energy minimization, is performed to minimize the energy of system upto the levels of 1.0E-6 eV.

5. Initially, Gaussian distribution is created by setting temperature of system to 300K and the system is described as NPT ensemble for equilibration, which is done upto 5,000 timesteps with each time step of 0.001 fs.

6. NVE ensemble is simulated by thermostating the system using Berendsen thermostat.

7. Müller-Plathe technique is used to calculate the thermal conductivity of a given material. Each simulation is executed for about 2,000,000 timesteps. Sample graph of temperature profile and kinetic energy, swapped as a function of time, are shown in Figures 4.17 and 4.18.

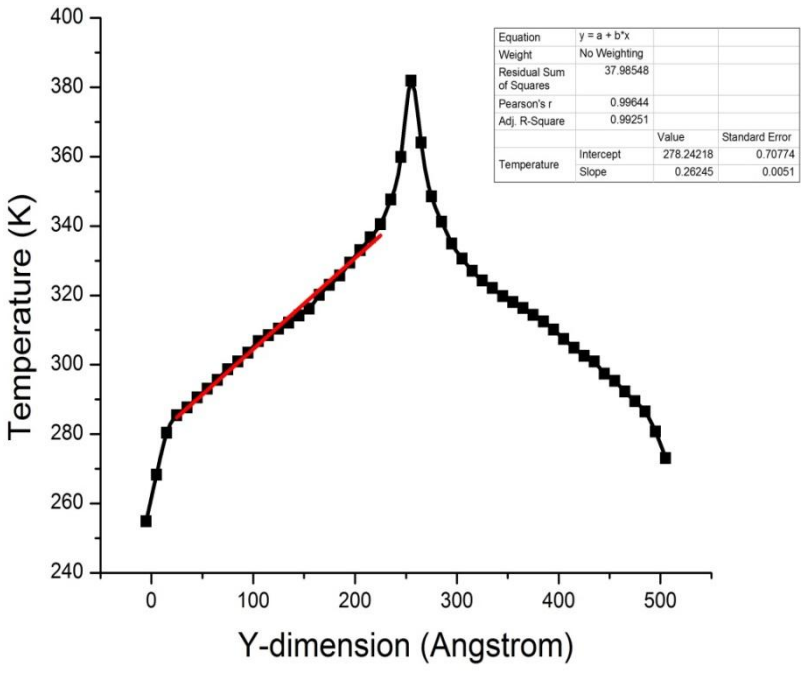

Figure 4.17 Temperature versus size of simulation box in Y direction, based on simulations.

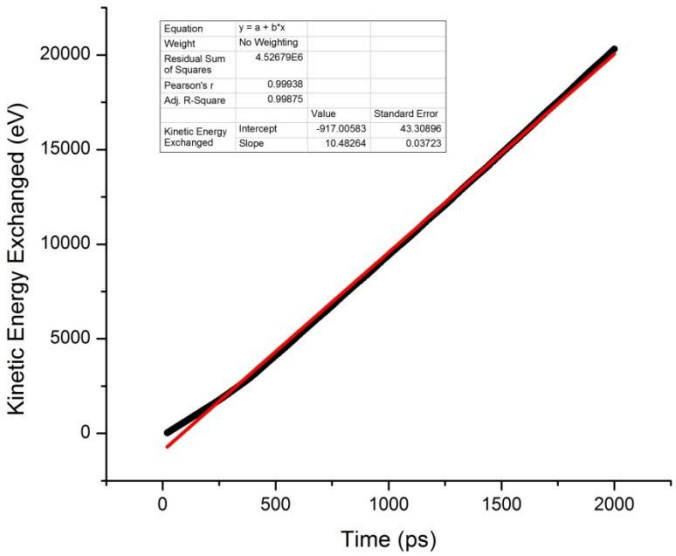

Figure 4.18 Kinetic energy versus time, based on simulations.

Once the verification of the model is established by comparison with the literature (experimental or simulated), the model is then extended to simulate the properties of graphene as function of orientation, number of layers, doping, vacancies etc. The comparison with the literature along with the description of the models will be explained in detail in Chapter 5.

4.4.1 Thermal Conductivity Calculations for Graphene Nanosheets and Nanoribbons

Figure 4.19 shows the thermal conductivity of single layer pristine graphene, armchair and zigzag graphene nanoribbons as a function of their length. It is observed that zigzag graphene nanoribbons have the highest thermal conductivity with respect to the armchair graphene nanoribbons as well as pristine graphene nanosheets. These results are consistent with the theory of Nika et al. [194] on small graphene flakes. The important

role of phonon scattering by graphene edges on the temperature dependence of thermal conductivity has also been discussed [195].

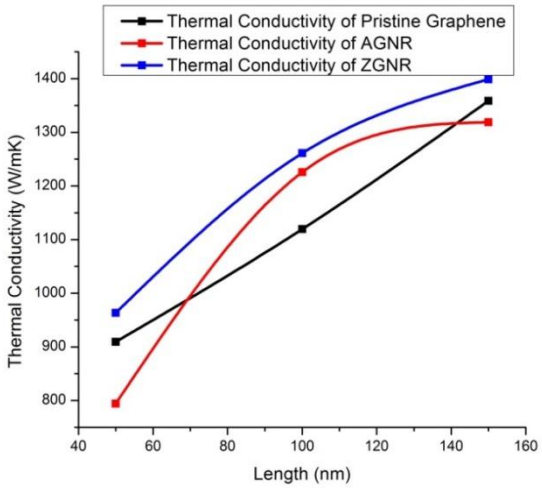

Figure 4.19 Simulated thermal conductivity of pristine graphene, armchair graphene nanoribbons, and zigzag graphene nanoribbons as a function of length.

The edge in the GNRs can decrease the thermal conductivity, which can be attributed to two reasons [196]. First, compared with that of graphene, there appears two edge-localized phonon modes in the low-energy region for the GNRs, i.e., the transverse acoustic mode, and the lowest-lying optical mode [197]. The edge-localized phonons can interact with other low-energy phonons and thus reduce their PMFP edge effect. This would remarkably reduce the low-energy phonon contribution to the thermal conductivity, which is very substantial and significant for thermal transport. Second, the boundary scattering at the edges of GNRs also reduces the thermal conductivity.

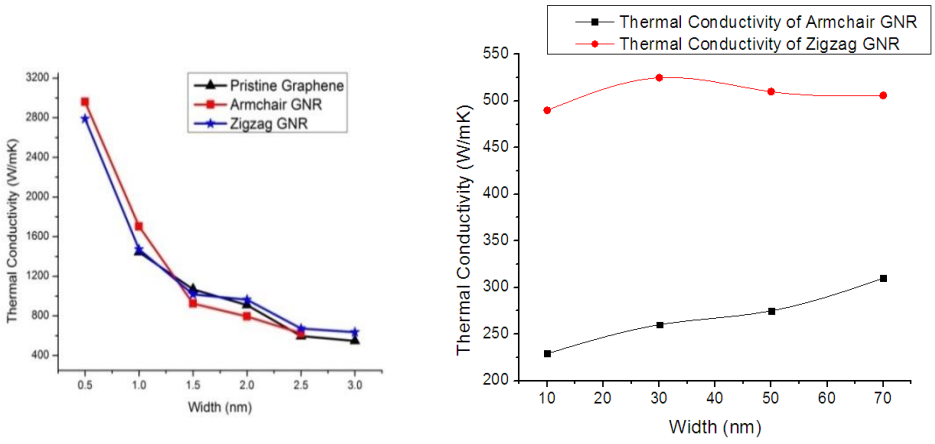

(a) (b)

Figure 4.20 Thermal conductivity of pristine graphene, armchair graphene nanoribbons and zigzag graphene nanoribbons as a function of their widths in the range of (a) 0.5 to 3 nm, (b) 10 to 70 nm with a constant length of 50 nm, based on simulations.

Figure 4.20 (a) shows the variations of thermal conductivity for graphene and GNRs as a function of the width for a constant 50 nm length in each case. Figure 4.20 (b) shows the variations of thermal conductivity for AGNR and ZGNR as a function of width for larger values of width. It is found that there is a sudden drop in the thermal conductivities initially from 0.5 nm to 1.5 nm widths while the thermal conductivity remains constant beyond 2 nm. The constancy of thermal conductivity at higher widths is also evident in the Figure 4.20 (b). The thermal conductivity is also found to be constant for increasing widths in case of AGNR. In the case of ZGNR, it is observed that the thermal conductivity first increases upto about 30 nm but decreases with further increase in width of ZGNR. As the width of GNR increases, the transport becomes more ballistic and is found to approach its limit. The heat flux is known to have preferential flow along the direction of width reduction in asymmetric graphene nanoribbons [198]. This is explained from the phenomena that, with increasing widths of GNRs, the total number of phonon modes increases, while the number of edge-localized phonon modes does not

change. Hence, the effect of edges is found to reduce with further increase in width of GNRs. The energy gap between various phonons is also known to reduce with increase in the width of GNRs. This leads to higher possibility of phonon related Umklapp process and reduction in the thermal conductivity. These phenomena govern the variations in the values of thermal conductivity of asymmetric GNRs with varying widths.

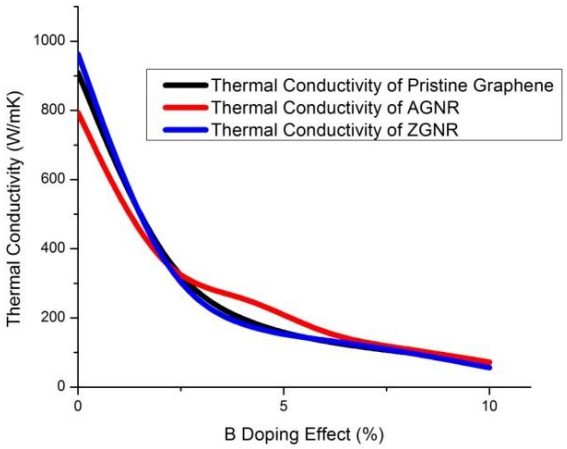

Figure 4.21 Effect of boron doping on the thermal conductivity of pristine graphene, armchair graphene nanoribbons and zigzag graphene nanoribbons, based on simulations.

Boron and nitrogen are known to be effective in modifying the electronic and optical properties of graphene making it suitable for optoelectronic devices. This makes it essential to understand the behavior of the thermal conductivity of doped graphene structures.

The effect of doping pristine graphene, AGNR and ZGNR with boron is shown in Figure 4.21. It is observed that there is a drastic reduction (~50%) in the thermal conductivity of graphene structures on doping with boron upto about 1%. Such a reduction has also been presented by NEMD techniques for doping of graphene with

nitrogen by Mortazavi et al. [199]. It is also noted that there is a reduced chirality dependence upon increase in dopant concentration.

Nitrogen is known to have atomic size comparability with carbon and forming strong bonds with carbon atoms. Doping with nitrogen has also been shown to improve biocompatibility and sensitivity of carbon nanotubes [200]. Figure 4.22 shows the thermal conductivity trends for pristine graphene, AGNR and ZGNR as a function of % nitrogen doping. It is found to exhibit drastic reduction in thermal conductivity, as in the case of boron doping in graphene structures.

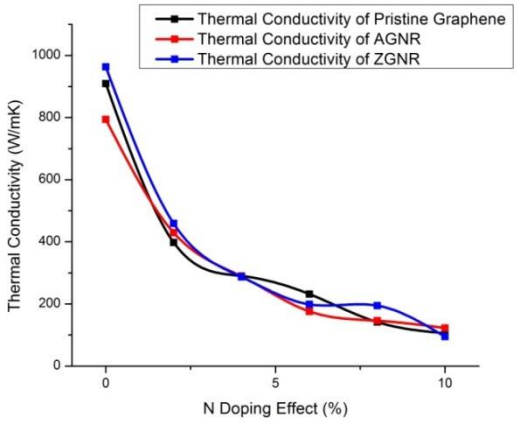

Figure 4.22 Effect of nitrogen doping on the thermal conductivity of pristine graphene, armchair graphene nanoribbons and zigzag graphene nanoribbons, based on simulations.

The temperature dependence of thermal conductivity of graphene is shown in Figure 4.23. It is found that there is a reduction in the thermal conductivity at higher temperatures in graphene structures. The results presented here would be significantly useful in applications involving large temperature variations and gradients. It is noted that the increase in temperature leads to reduction in chirality dependence. At about 400K, all the graphene nanostructures are found to have same value of thermal conductivity.

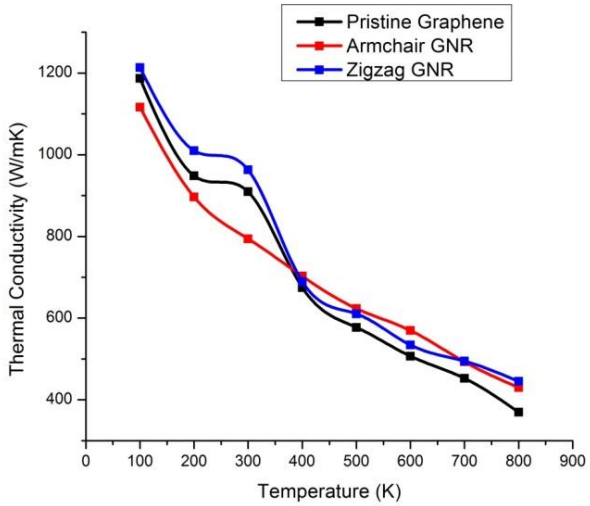

Figure 4.23 Simulated temperature dependence of thermal conductivity of pristine graphene, armchair GNR, and zigzag GNR in the range of 100 – 800 K.

Depending on the procedure used during synthesis of graphene or experiments to modify its properties by doping by chemical reduction, graphene samples are inevitably expected to have single vacancies, Stone-Wales defects, grain boundaries, etc. [201]. We have simulated the thermal conductivity of pristine graphene, AGNR and ZGNR structures with varying concentration of vacancies upto about 10%, using NVE ensembles and periodic boundary conditions using MD. It is noticed that there is a drastic reduction in the thermal conductivity values. Principally, the bonds surrounding the vacancy defects should have higher stiffness (stiffness of bonds comparable to double or triple bonds) due to less coordination than the original graphene structures. Also, it is shown by Klemens et al. [202] that the relaxation time due to point defect scattering is inversely proportional to vacancy concentration and DOS. This leads to higher mean free path with increase in concentration of vacancies in the structure. Thus, a drastic reduction in thermal conductivity is observed with increasing vacancy concentration. A detailed study of graphene with defects along with the corresponding phonon DOS has been

presented by Zhang et al. [201] using NEMD simulations. Effect of vacancies on thermal conductivities of graphene nanostructures is presented in Figure 4.24.

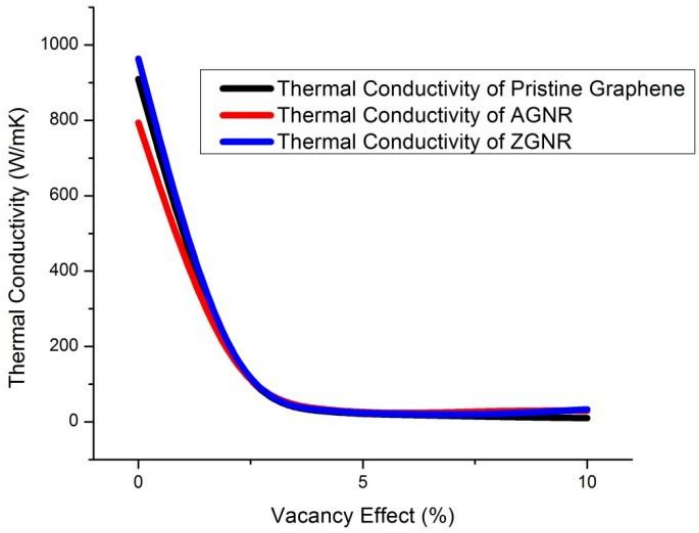

Figure 4.24 Effect of vacancies on thermal conductivity of pristine graphene, armchair GNR, and zigzag GNR, based on simulations.

In principle, reduction in thermal conductivity of graphene structure is expected with increasing number of layers in graphene structures. These trends have been shown in Figure 4.25. The interlayer interactions are found to be responsible for the substantial reduction of thermal conductivity in graphene. Pristine graphene is found to have the lowest thermal conductivity and ZGNR has highest thermal conductivity with increasing number of layers, indicating the dominance of chirality dependence in graphene nanostructures. Applications in thermal management for semiconductor devices and circuits have been proposed for multilayer graphene based materials [203].

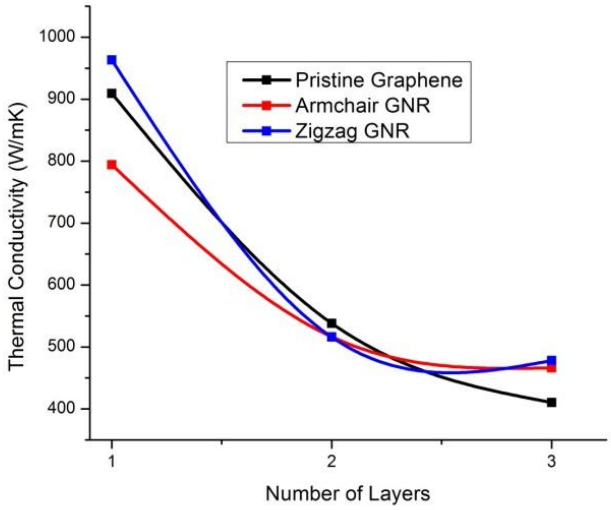

Figure 4.25 Effect of number of layers (upto 3) of pristine graphene, armchair GNR and zigzag GNR on thermal conductivity, based on simulations.

Ghosh et al. [194] have experimentally found that graphene has thermal conductivities in the range of 3000–5000 W/m K depending on the specific sizes, which vary from 1 to 5 microns.

4.5 Transport Parameter Calculations

The transport parameter calculations, in this thesis, have been performed using Boltztrap Software, as explained in Chapter 3. Boltztrap uses the electronic band structure calculations performed using Quantum Espresso for post-processing and evaluating transport parameters. All the transport parameters are found to be interdependent as a function of chemical potential and temperature. This leads to the need for evaluation and comparison of each of these parameters.

Chemical doping is known to change the electronic band structure. Thus, there are changes in transport parameters as a function of % doping (p or n type). In order to

improve the thermoelectric properties, graphene needs to have bandgap. This objective is achieved by using GNRs by appropriate patterning. GNRs have bandgap dependent on the ribbon width. AGNRs are semiconductors and have the bandgap inversely proportional to their widths. Bandgap is found to be dependent on the chirality of graphene (armchair / zigzag). Also, attempts to reduce phonon induced lattice thermal conductivity of graphene have made researchers work on disordered graphene structures. It is found that such structures have improved Seebeck coefficient. However, increase in bandgap in such disordered GNRs is found to lead to reduction in electrical conductivity. Thus, overall thermoelectric performance of such structures is affected and needs to be optimized [204].

Zigzag GNRs are found to be metallic with very low Seebeck coefficient. The transport in ZGNRs is independent of line edge roughness in the first conduction plateau around the Fermi level [205]. The thermoelectric performance of ZGNRs has been reported to be improved in the presence of extended line defects by Hossein et al. [206] using quantum mechanical non-equilibrium Green's function simulations.

Figure 4.26 shows the plot of the density of states (DOS) of pristine graphene as a function of chemical potential. This is found to be matching with DOS plots in the literature, as shown in Figure 2.5. It is known that graphene has a peculiar electronic density of states with nil DOS at the point of connection between conduction band and valence band (called Dirac Point), as discussed in Chapter 2.

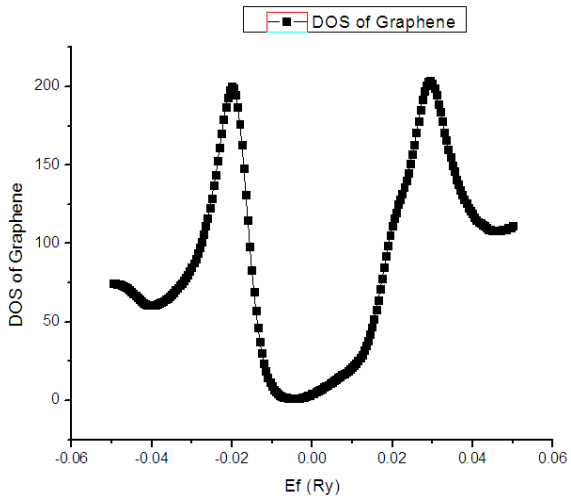

Figure 4.26 Simulated DOS for single layer graphene as a function of chemical potential.

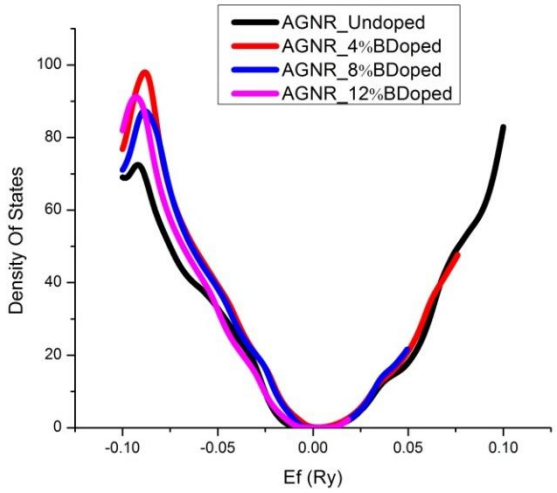

Figure 4.27 Simulated DOS of AGNR and 4%, 8% and 12% boron doped AGNR.

Figure 4.27 shows the comparison of DOS of 0%, 4%, 8% and 12% boron doped armchair GNR. It is observed that there is a finite displacement of Dirac point to the positive side of the energy, indicating p-doping. Also, there is a finite bandgap near the Dirac point.

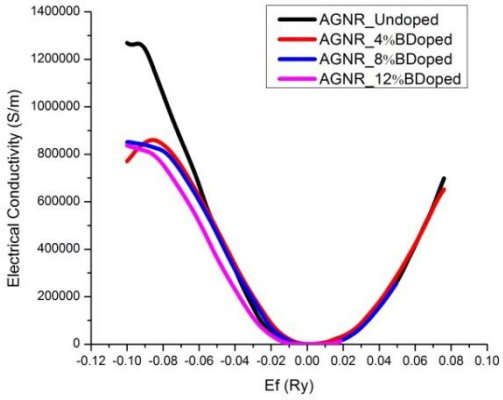

Figure 4.28 Simulated electrical conductivity comparison of AGNR with 0%, 4%, 8% and 12% boron doping.

Figure 4.28 shows the comparison of electrical conductivity of armchair GNR with different % boron doping as a function of chemical potential. It is found that the peak electrical conductivity reduces as a function of boron doping. This is attributed to the changes in band structure of GNRs with doping. The electrical conductivity is also found to be a function of temperature. It is shown that boron or nitrogen doping causes increase in electrical conductivity in the low temperature region, while it causes reduction of electrical conductivity in the high temperature region [207].

Figure 4.29 shows the variations of Seebeck coefficient as a function of chemical potential for AGNR and ZGNR with boron doping. It is noticed that Seebeck coefficient peaks at +/- k_BT and is found to nearly vanish around the band gap. Seebeck coefficient curves are symmetric for AGNRs, which can be attributed to the symmetrical distribution of first conduction channels. There is a change in sign of Seebeck coefficient across the charge neutrality point (CNP) as majority carrier density changes from electrons to holes. This is also reported in the literature [52, 149]. 8% boron doped ZGNRs are not found to be symmetrical around Fermi level, as shown in Figure 4.29. Thermopower for undoped

AGNR is ~200 μV/K. Thermopower ~600 μV/K is observed in case of 12% boron doping of AGNR. It is also noted the peak thermopower for boron doped ZGNR is lesser than the corresponding boron doped AGNR to the extent of ~300 μV/K.

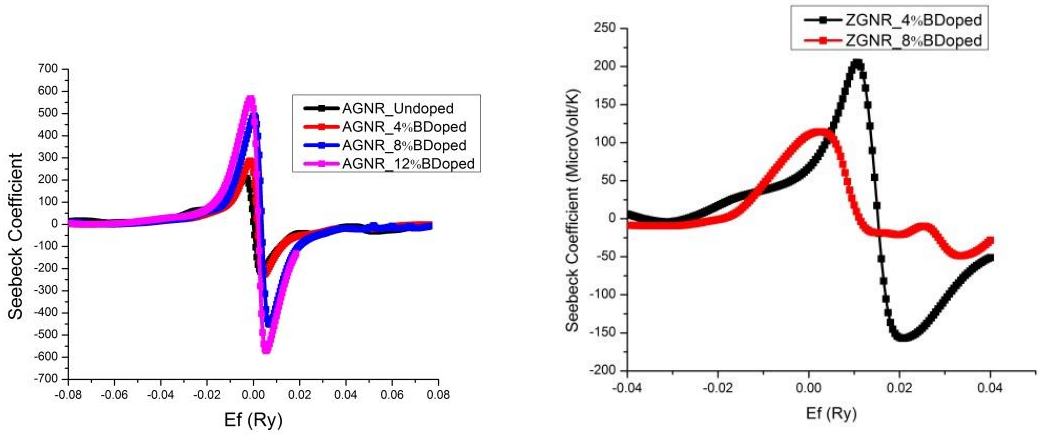

(a) (b)

Figure 4.29 Thermopower (Seebeck coefficient) μV/K versus chemical potential (Ry) for (a) AGNR with 0%, 4%, 8% and 12% B doping and (b) ZGNR with 4% and 8% B doping at 300 K, based on simulations.

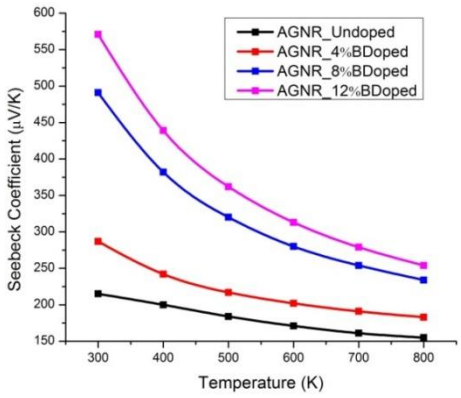

Figure 4.30 Peak Seebeck coefficient as a function of temperature for AGNR with 0%, 4%, 8% and 12% boron doping, based on simulations.

The variation in peak Seebeck coefficient (TEP) with temperature for AGNR with boron doping is shown in Figure 4.30. It is found that the peak value reduces with increase in temperature from 30-800 K almost linearly at higher temperatures.

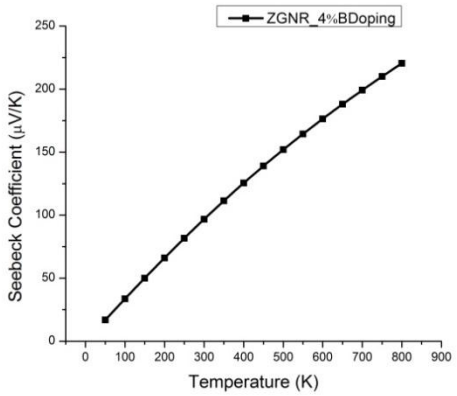

Figure 4.31 Simulated Seebeck coefficient as a function of temperature for 4% boron doped ZGNR at the Fermi level.

Seebeck coefficient as a function of temperature for ZGNR doped with boron at Fermi level is shown in Figure 4.31. It is found that the peak value reduces with increase in temperature from 50-800 K almost linearly at higher temperatures. This is indicative of the thermoelectric generation mechanism being diffusive TEP, with absence of phonon drag component, as reported in the literature [149].

The effect of doping on Hall resistivity of AGNR is shown in Figure 4.32. It exhibits similar variations as observed in the Seebeck coefficient. The maximum Hall resistivity is noted at 12% boron doping.

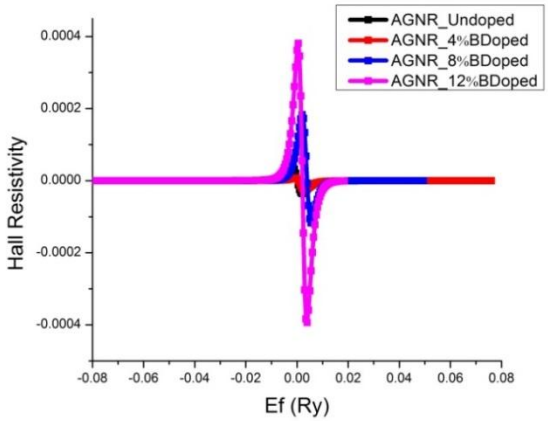

Figure 4.32 Comparison of simulated Hall resistivity (m^3/C) versus chemical potential for AGNR with 0%, 4%, 8% and 12% boron doping.

The electronic thermal conductivity is found to exhibit a behavior similar to electrical conductivity for AGNR. The peak value is found to be ~10 W/mK as shown in Figure 4.33, which is extremely small as compared to phonon-induced lattice thermal conductivity. It is noticed that the peak value reduces with increase in % boron doping in AGNR. The reduction is attributed to the disturbed lattice coordination in the regions around the doped atoms.

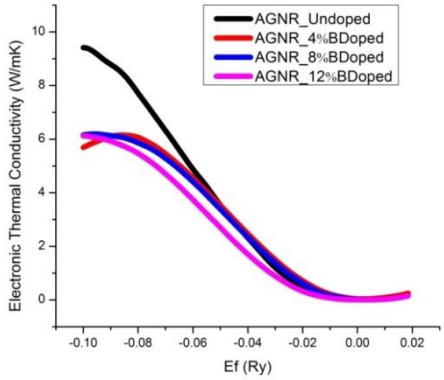

Figure 4.33 Comparison of simulated electronic thermal conductivities of AGNR with 0%, 4%, 8% and 12% boron doping as a function of chemical potential (Ry).

Nitrogen doping in AGNR also leads to variation in the transport parameters. The trends for variations in Seebeck coefficient is as shown in Figure 4.34.

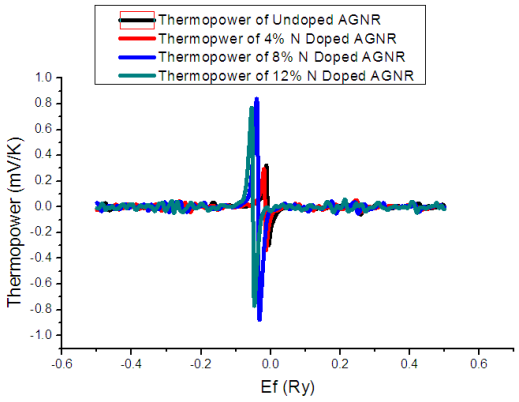

Figure 4.34 Simulated thermopower of AGNR (mV/K) with 0%, 4%, 8% and 12% nitrogen doping as a function of chemical potential (Ry).

It is observed that the peak thermopower is observed at ~ 8% nitrogen doping in AGNR. There is a substantial increase in the thermopower as compared to undoped AGNR. Variation of Hall resistivity for AGNR with nitrogen doping is shown in Figure 4.35. It is found to exhibit behavior similar to the Seebeck coefficient.

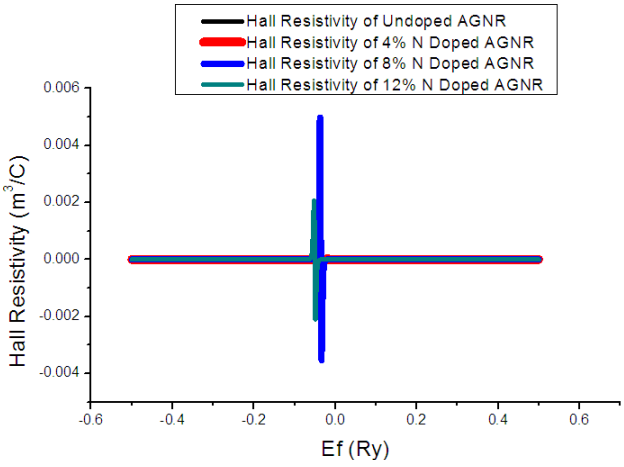

Figure 4.35 Comparison of simulated Hall resistivity for AGNR with 0%, 4%, 8% and 12% nitrogen doping as a function of chemical potential (Ry).

The variation in electronic thermal conductivity for undoped AGNR and 4% nitrogen doped AGNR is shown in Figure 4.36 in the range of -0.07 to +0.07 Ry.

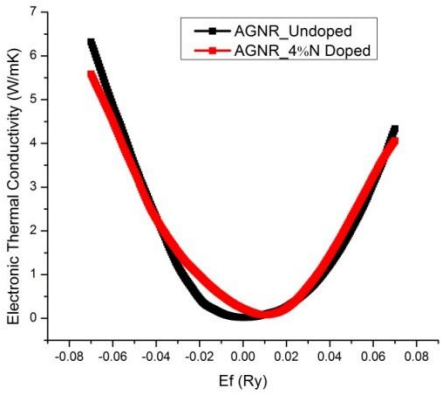

Figure 4.36 Simulated electronic thermal conductivity of AGNR with 0% and 4% nitrogen doping as a function of chemical potential (Ry).

It is noted that the peak values reduce with increase in nitrogen doping. This is comparable with boron doping in AGNR and the reason for reduction is attributed to changes in the lattice coordination leading to corresponding changes in phonon DOS.

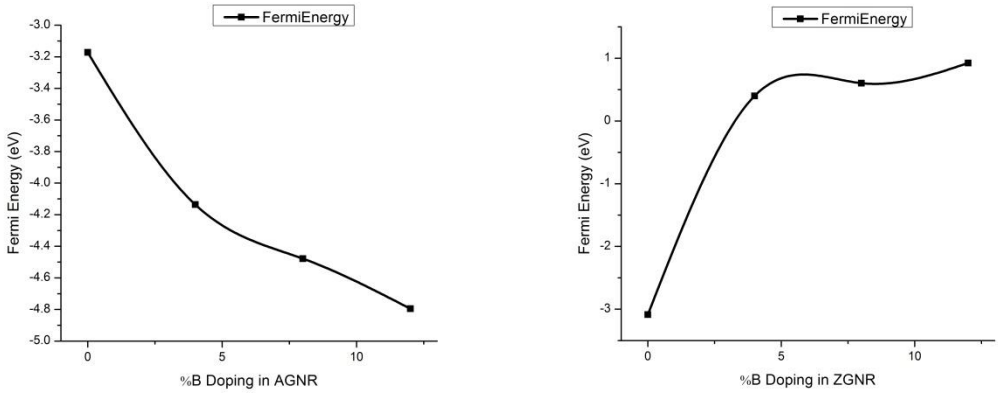

(a) (b)

Figure 4.37 Fermi energy trends for boron doped (a) AGNR and, (b) ZGNR, based on simulations.

The corresponding Fermi energy variations for boron doping in AGNR and ZGNR are shown in Figure 4.37. It can be observed that the p- doping leads to increase in value of Fermi level for each case.

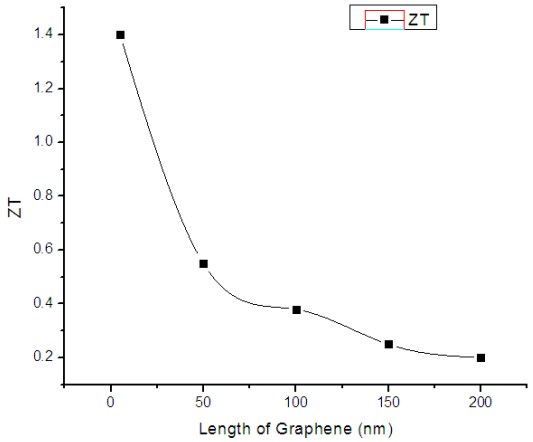

Figure 4.38 ZT values as a function of length of graphene.

Figure 4.38 shows ZT calculated for single layer graphene as a function of length with a constant width of 2 nm. It is found to decrease with increase in the length, as thermal conductivity increases as a function of length in this regime.

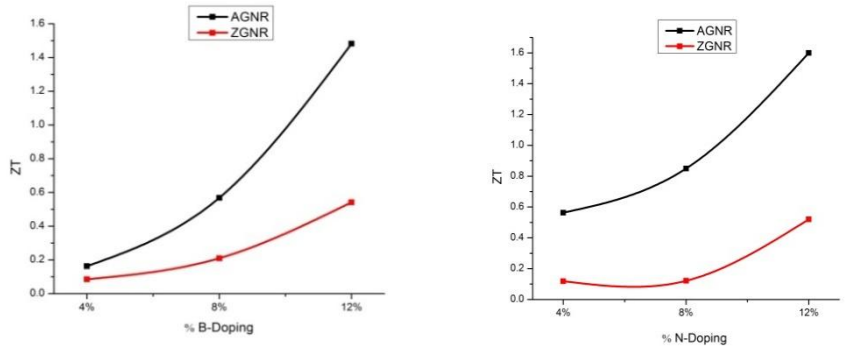

(a) (b)

Figure 4.39 ZT as a function of (a) % boron doping and, (b) % nitrogen doping in armchair GNR and zigzag GNR.

Figure 4.39 (a) and (b) show the comparison of ZT values for similar lengths of armchair and zigzag GNR and the effects of boron and nitrogen doping at room temperature. It is found that the values of thermal conductivity are much lower for AGNR w.r.t. ZGNR, hence leading to higher values of ZT. The peak ZT value observed is about 1.6, which is much higher than conventional thermoelectric materials such as Bi_2Te_3. Even higher values of ZT have been reported for GNRs with optimized geometries.

In attempts to reduce phonon-induced lattice thermal conductivity, ZGNRs with vacancy defects have been simulated. The vacancies have been randomly distributed in the structure. Firstly, the relaxation is performed till the energy of the system reaches 1E-10 eV. This is followed by self-consistent calculation with cutoff for energy as 70 Ry. It

is found that the peak thermopower is found to increase with increasing concentration of vacancies.

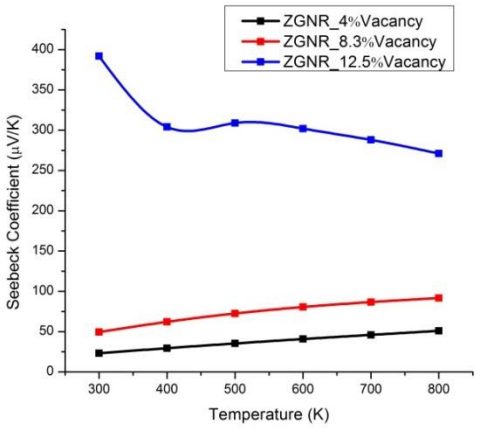

Figure 4.40 Simulated Seebeck coefficient as a function of temperature for ZGNR with 4%, 8.3% and 12.5% vacancies.

Figure 4.40 shows the behavior of Seebeck coefficient as a function of temperature for ZGNRs with about 4%, 8.3% and 12.5% vacancies. It is found that the ZGNRs with 12.5% vacancies are found to have enhanced Seebeck coefficient. Seebeck coefficient is noted to increase slightly with temperature for ZGNR with 4% and 8.5% vacancies. ZGNR with 12.5% vacancies is found to exhibit reduction in Seebeck coefficient with increase in temperature from 300 to 800K.

Bahamon et al. have investigated the electrical properties of ZGNRs that included extended line defects (ELD-ZGNRs) along the length of the nanoribbon [208]. It was noted that the extended line defects break the electron-hole energy symmetry in the GNRs. It introduces an additional electron band around the Fermi level. In this way, the asymmetry in the density of states and transmission function is achieved which improves the Seebeck coefficient. This structure has been experimentally realized recently by Lincoln and Mark [209].

Figure 4.41 shows the improvement in ZT for ZGNR with increase in % vacancy. This is as a result of increased thermopower and reduced value of thermal conductivity for the defected structure of ZGNR. Thus, inducing vacancies in ZGNR is an important technique for improvement of thermoelectric performance of graphene nanostructures.

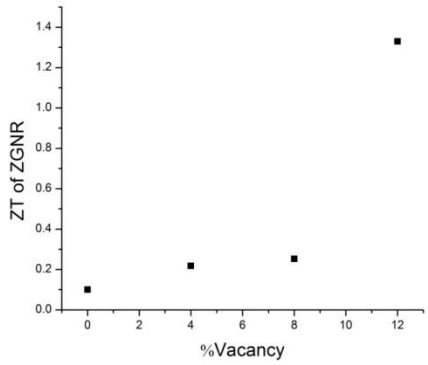

Figure 4.41 ZT as a function of % vacancy in zigzag GNR, based on simulations.

4.6 Emissivity Calculations

This section has been published in Journal of Materials (JOM) [115]. Three case studies have been presented in this work depending on the application of graphene in specific areas. These are:

I. Bulk materials

II. Multi-layers

III. Device applications

4.6.1 Bulk Materials Analysis

In this section, the optical properties, mainly emissivity, transmittance and reflectance spectra of carbon like materials: Diamond, Graphite and Graphene are presented. These materials are of significant importance in electronics.

As discussed in the literature, carbon like materials are finding significant applications in electronics due to their excellent physical, mechanical, electronic and electrical properties. As observed in Figure 4.42 (a), emissivities of bare substrates of carbon allotropes, natural diamond and graphite for different thicknesses, in the wavelength range of 0.4-20 μm, have been compared. It is noticed that the emissivity increases with increasing thickness of diamond in the range of 500-5000 μm from 0 to ~ 0.6. For the same range of thickness, i.e., 500-5000 μm, absorptance in graphite is found to follow a single trend rising from 0.3 at 0.43 μm to 0.48 at 1.7 μm and then the emissivity values decrease linearly to ~ 0.11 at 20 μm. The emissivity of diamond for a thickness of 5000 μm is found to be a maximum, showing the trend of increasing linearly with wavelength from about 0 at 0.4 μm to 0.57 at 4 μm wavelength.

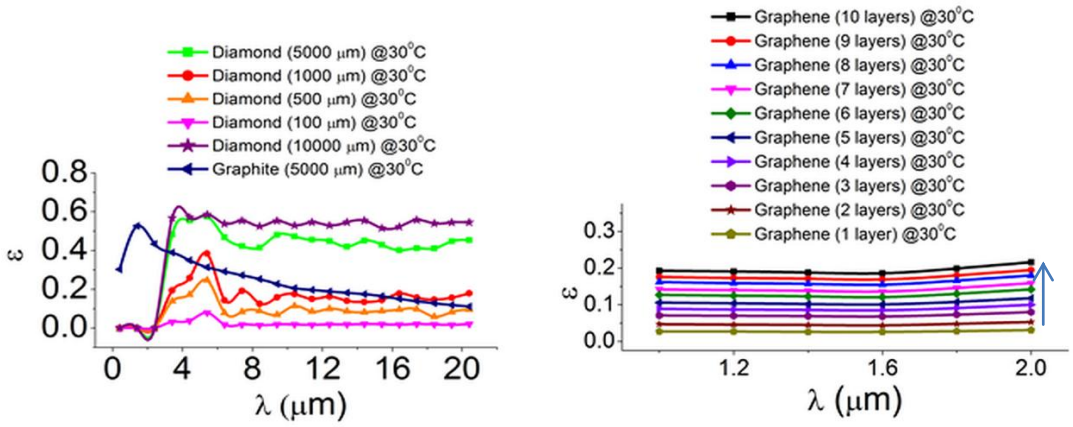

(a) (b)

Figure 4.42 (a) Simulated emissivity versus wavelength for diamond and graphite, (b) Simulated emissivity versus wavelength for graphene up to 10 layers (temperature in ºC) [115].

Figure 4.42 (b) shows emissivity versus wavelength for graphene as well as few layers of graphene (FLG) at room temperature, which is found to be almost constant with respect to wavelength in the range of 1 to 2 μm (Temperature in ºC).

Single layer graphene is found to absorb ~ 2.3% of the incoming IR radiation, theoretically as well as experimentally, which is attributed to the interband absorption in a wide range of wavelengths spanning from the visible to infrared [210]. The values obtained from our calculations are found to be ~2.5% (as can be seen in the emissivity plot in Figure 4.42 (b)) for single layer graphene and is found to increase to ~ 20% with increasing number of layers to 10. Graphene has a very low reflectivity, and most of the incident electromagnetic waves are found to be transmitted (about 97%).

4.6.2 Multilayered Structures

It is essential to obtain accurate values of the temperature in specific spectral range for multilayered structures. This leads to application of non-contact temperature sensing devices such as pyrometers. Accurate values of wavelength and temperature dependent emissivity of a given material or structure are essential in order to obtain temperatures using pyrometers. Here, the trends in optical properties in the IR wavelength range in case of silicon on graphene, silicon on graphite, and graphene on silicon have been presented. A multi-layered structure, as shown in Figure 4.43, has been considered in simulations of the optical properties of silicon on graphene and silicon on graphite. The variation in optical properties with changing substrate thickness from 100-500 μm has been shown.

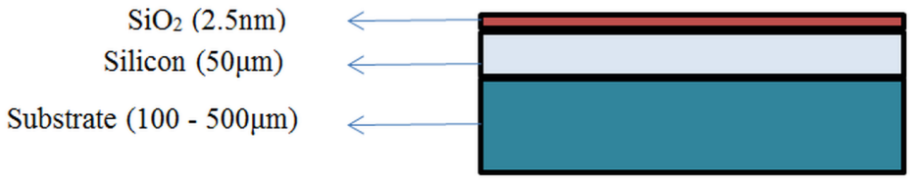

Figure 4.43 Multilayered structure simulated for silicon on graphene / graphite [115].

4.6.2.1 SiO_2 / Si / Graphene. This multilayered structure is simulated as shown in Figure 4.43, with substrate material taken as graphene (1-4 layers) at room temperature and compared with silicon (50μm) and SiO_2(2.5nm)/Si(50μm). The simulated emissivity as a function of wavelength for this structure is shown in Figure 4.44 (a). It is observed that the effect of graphene is to increase the values of emissivity at a given wavelength and its value stays linear over the entire wavelength range.

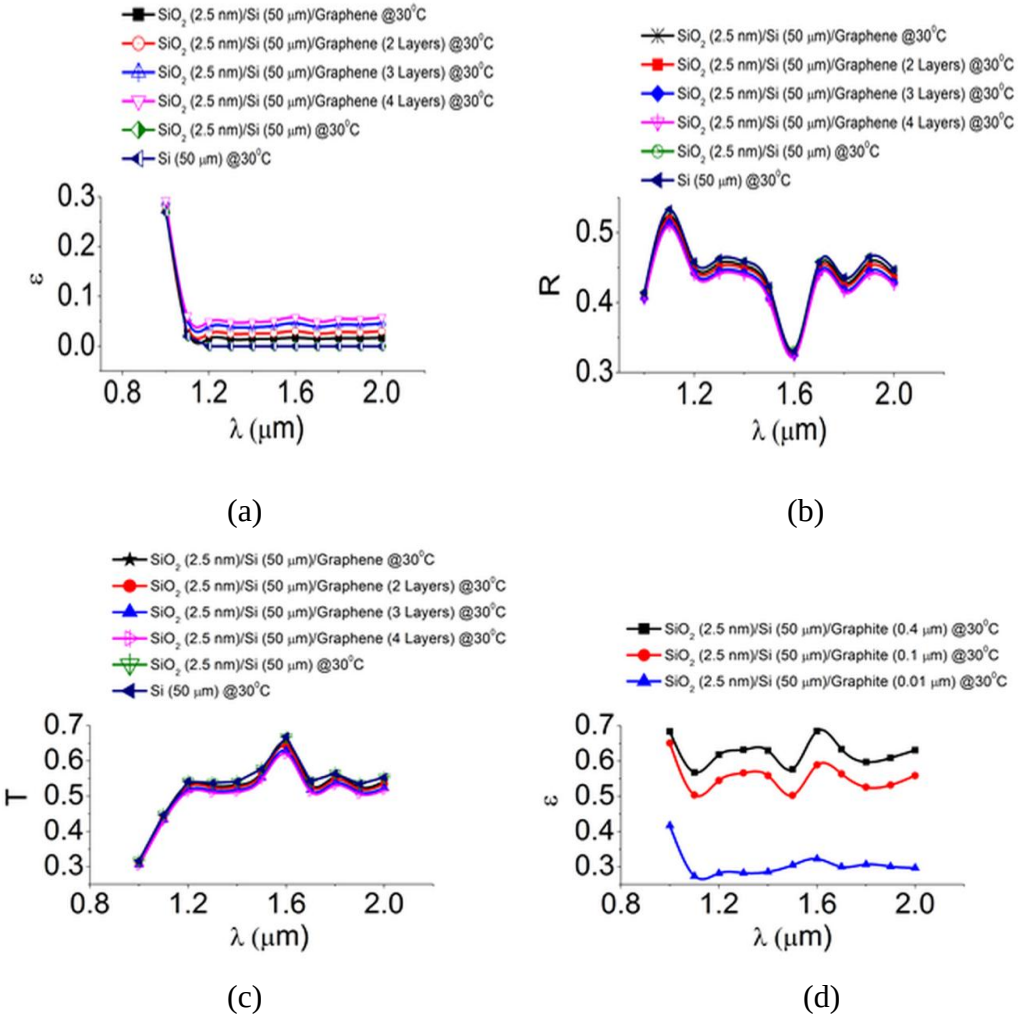

Figure 4.44 (a) Emissivity, (b) Reflectance and (c) Transmittance as a function of wavelength in the wavelength range of 1-2 μm for SiO_2/Si/graphene structure, (d) Emissivity as a function of wavelength in the wavelength range of 1-2μm for SiO2 (2.5 nm)/Si (50 μm)/graphite (0.4 μm, 0.1 μm and 0.01 μm) (Temperature in ºC) [115].

The transmittance is found to decrease slightly with increasing number of layers of graphene as shown in Figure 4.44 (c). As shown in Figure 4.44 (b), a sharp decrease in average reflectance from 0.45 to 0.32, at 1.6 μm wavelength, is observed. Comparison of emissivity of substrate as graphite (Figure 4.44 (d)) versus graphene (Figure 4.44 (a)) indicates that the values of emissivity are much higher in the case of graphite substrate than in the case of graphene at room temperature. The emissivity changes slightly for 0.01μm thick graphite. In Figure 4.44 (d), there are specific features like flat plateaus corresponding to emissivity of 0.65 for the case of graphite substrate (0.4μm thickness). Also, a valley at about 1.5μm wavelength and a peak at about 1.6μm wavelength are observed for the graphite substrate.

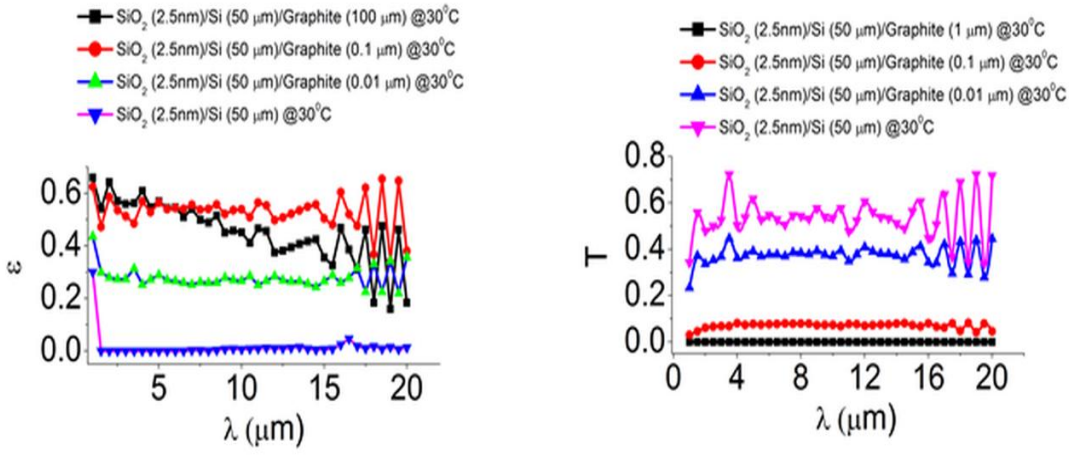

(a) (b)

Figure 4.45 Emissivity of SiO_2 (25Å)/ Silicon (50μm) / Graphite (1μm) (Temperature in ºC) [115].

4.6.2.2 SiO_2 / Si / Graphite. The multilayered structure as in Figure 4.43 has been simulated. Graphite is the substrate layer with varying thicknesses of 0.01μm, 0.1μm and 100μm. Based on our simulations, above ~ 0.3μm thickness of graphite, the

values of emissivity are constant and independent of thickness. The values of emissivity are found to increase with increase in thickness of graphite from 0.01 μm to 0.1 μm. The emissivity of graphite decreases above wavelength of ~ 5μm up to 20μm, for thicknesses above 0.3μm. These trends are as shown in Figure 4.45.

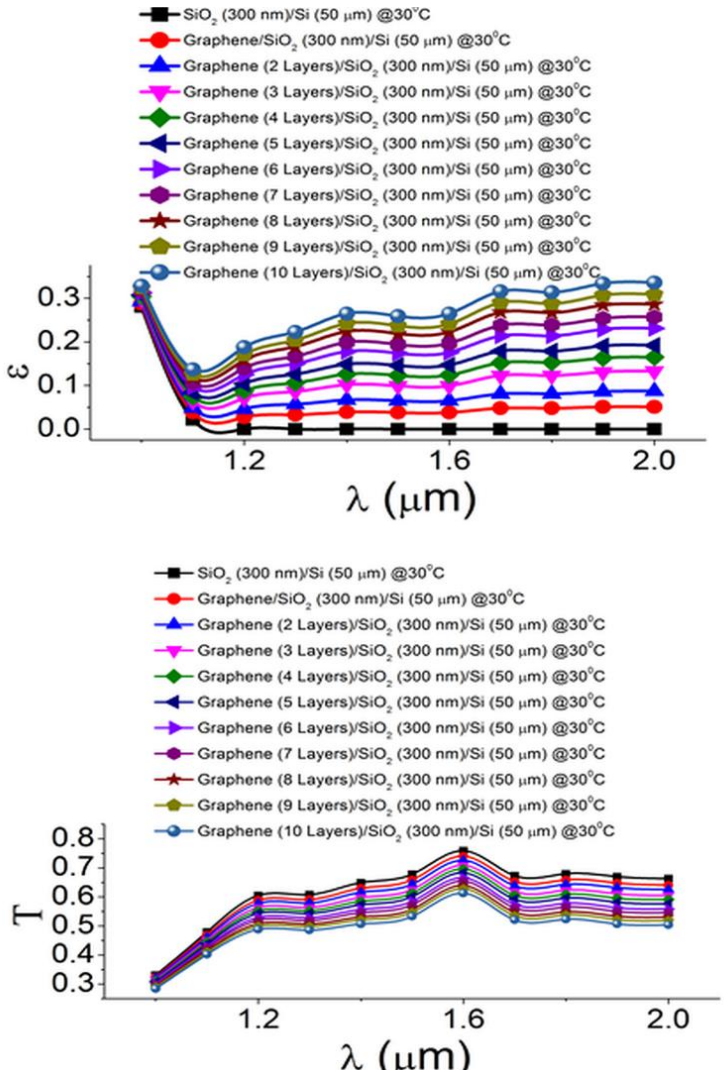

Figure 4.46 Emissivity and transmittance of SiO_2 (25 Å)/silicon (50 μm)/graphite (1 μm) (Temperature in ºC) [115].

4.6.2.3 Graphene / SiO_2 / Si. The structure with top layer of graphene (1-10layers thick)/SiO_2(300nm)/Si(50μm) has been simulated. Results of emissivity and transmittance as a function of wavelength are as shown in Figure 4.46.

It is evident from Figure 4.46 that the emissivity increases with increasing layers of graphene from 1 to 10 layers almost linearly from ~0.02 to 0.2 respectively. It is observed that the emissivity is almost constant for a particular structure within the wavelength range of 1.2-2 μm. The corresponding transmittance versus wavelength plots show a constant decrease in transmittance for a given wavelength as the number of layers of graphene are increased, with a peak at about 1.6 μm wavelength and almost constant transmittance from 1.7-2 μm.

4.6.3 Device Studies

A multilayered bolometer device configuration, as shown in Figure 4.47, has been simulated. A bolometer is a device that responds by changing its resistance due to increase in temperature on interaction with the incident thermal radiation [119]. When power is coupled to electron system, electrons are driven out of thermal equilibrium along with phonons, creating hot electrons and hence such a bolometer is called the Hot Electron Bolometer (HEB) [120]. It is essentially a sensitive thermometer. It can be used with a spectroscope to measure the ability of some chemical compounds to absorb wavelengths of infrared radiation, by which one can obtain important information about the structure of the compounds.

Due to its ability to absorb light from mid-infrared to ultraviolet with nearly equal strengths, graphene has found applications in optical detectors. Graphene is typically well suited for HEBs due to its small electron heat capacity and weak coupling of electrons

and phonons, which causes large light induced changes in electron temperature. Small electronic specific heat makes it possible for faster response times, higher sensitivity and low noise equivalent power. At low temperatures, usually in the cryogenic range, electron-phonon coupling in metals is very weak. The usual range of operation of HEBs are cryogenic, while graphene based HEBs can be used at higher temperatures due to low electron-phonon scattering even at room temperature and its highest known mobilities of charge carriers at room temperature [48, 119, 121].

However, resistance of pristine graphene is weakly sensitive to electron temperature. Various approaches have been attempted to address this issue in the literature. The first one is a dual gated bilayer graphene (DGBLG) bolometer [211], which has temperature dependent resistance as well as weak electron-phonon coupling. Light absorption by DGBLG causes electrons to heat up due to their small electron specific heat, while the weak coupling of electrons and phonons helps in creating bottleneck in heat path, decoupling the electrons from phonon path. Good light sensitivity causes change of resistance in the sample, which can then be converted to detectable electrical signal. The second approach, proposed in the literature, is to use disordered graphene instead of pristine graphene. Disordered graphene has been shown to exhibit highly temperature dependent resistance. Also, graphene film is separated from the electrical contacts by a layer of boron nitride, which acts as a tunneling barrier to increase the contact resistance and hence thermal resistance, resulting in better thermal isolation [119, 211].

It is to be noted that, in order to obtain higher responsivity of a device, one needs to essentially increase the absorptance in the device. Various methods for improving this

characteristic are: using multilayered graphene, surface plasmonics enhancement or microcavity, with the latter two introducing selectivity of wavelengths [119]. Two types of graphene based hot electron bolometer devices have been simulated based on these concepts.

4.6.3.1 Case I. In this case, we have simulated the bolometer structure, as shown in Figure 4.47, by changing the number of layers of graphene and studying their corresponding emissivity (or absorption) to develop understanding of its responsivity [211].

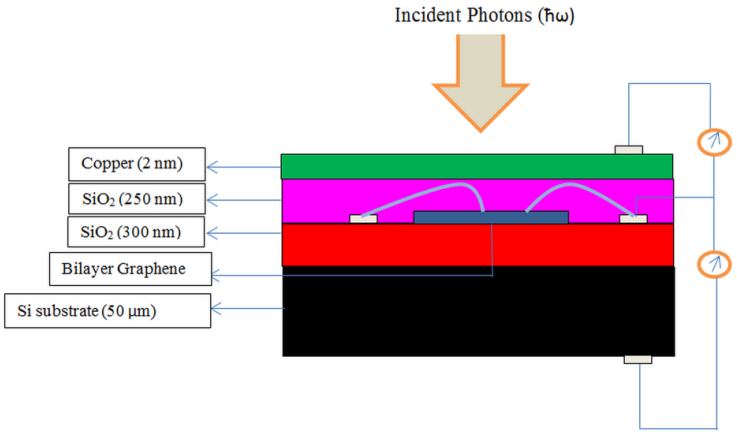

Figure 4.47 Bolometer device configuration [211].

Figure 4.48 shows the behavior of resistance with temperature for a bilayer graphene bolometer [119].

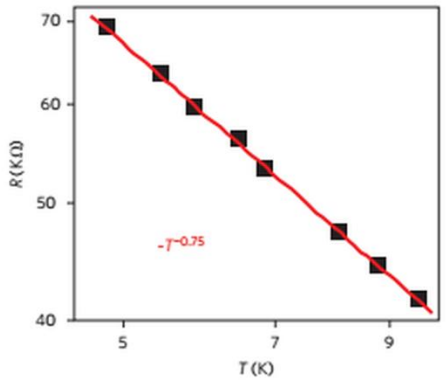

Figure 4.48 Resistance as a function of temperature for bilayer graphene bolometer [119].

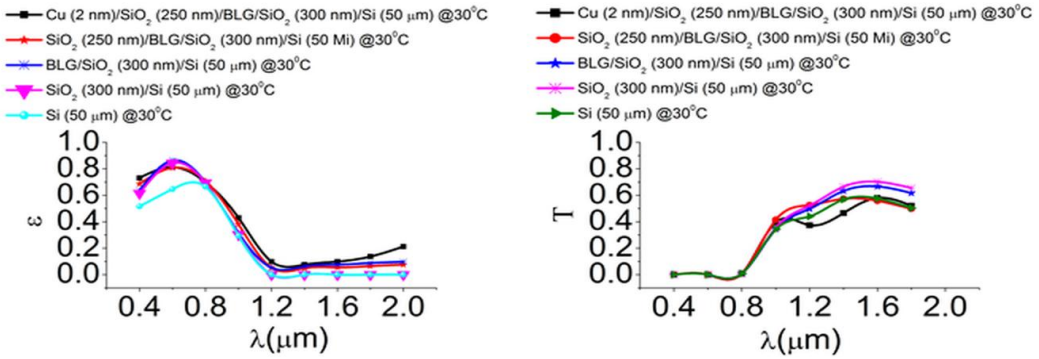

Figure 4.49 Emissivity (or absorptance) and transmittance as a function of wavelength for the various layers in the proposed bolometer configuration (Temperature in ºC).

As shown in the emissivity plot in Figure 4.49, it is observed that, for silicon (50μm) and SiO_2 (0.3μm)/Si(50μm), the curves follow similar trends, with the latter having emissivity (or absorptance) (higher by 0.1) than the former. The emissivity (or absorptance) is found to increase for each added layer in the case of the bolometer configuration. The increase in emissivity (or absorptance) is found to be highest with copper layer of 2 nm on the top, in the range of wavelength from 0.8-2μm for the bolometer structure. This shows improvement in the responsivity of the device.

It is clear that the influence of copper layer on the top is to increase the absorptance to about 20%, as compared to about 10% for the multilayered structure with

corresponding reduced transmittance for the structure. Also, copper has high value of temperature coefficient of resistance (about $4.29 \times 10^{-3}/^{\circ}C$) [212] and hence can be considered as a material that enhances the responsivity of the device by detecting smallest change in temperature. Also, due to the layer of bilayer graphene (BLG), the device is expected to have higher speed of response, as BLG has very less electron-phonon interaction and very high mobility of electrons even at room temperature.

4.6.3.2 Case II. Graphene has been shown to be an excellent material for electronic applications based on its electron transport properties. However, there are some limitations of graphene based devices such as induction of surface optical phonons on graphene that are in contact with substrate materials (commonly SiO_2/Si), reduction in carrier mobilities than its free lying form, surface roughness and inhomogeneity of charge carriers [213].

Hence, a novel approach of suppressing surface dangling bonds and surface charge traps has been proposed by using hexagonal boron nitride (h-BN) as a substrate for graphene, as h-BN has strong ionic bonding in hexagonal lattice structure. It is known that there is about 1.7% lattice mismatch between h-BN and graphene and hence there is little electronic coupling with graphene. This approach has been shown to endow the device with higher electron mobilities as well as electron-hole charge inhomogeneity.

In this case, the bolometer structure, as shown in Figure 4.50, has been simulated, based on the research by Han et al. [119] and the multilayered structure considered by Wang et al. [213]. The optical properties of: (a) pristine graphene (instead of disordered graphene) and (b) varying layer thickness of graphene and hexagonal boron nitride (h-

BN) on SiO_2/Si substrate, have been simulated. The evolution in their emissivity and transmittance as a function of wavelength (1-2 μm) has been presented.

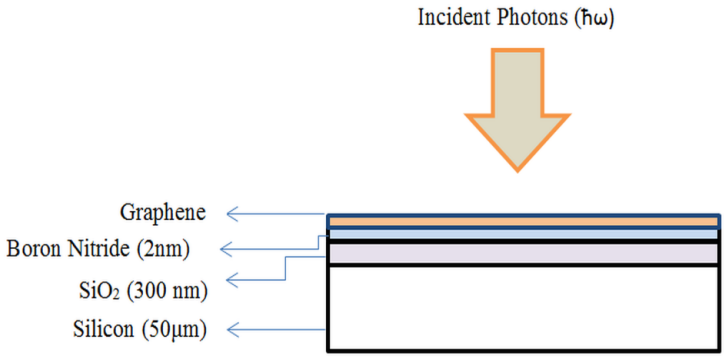

Figure 4.50 Bolometer device structure with multilayered configuration graphene/BN /SiO_2/Si [119].

Figure 4.51 shows the resistance versus temperature plot for this bolometer [119]. It is clear from this figure that pristine graphene layer has a very small change in resistance with temperature. Therefore, increasing the thickness of graphene layer can be considered as an alternate approach to increase the absorption of the device and hence improving its responsivity. Also, varying the thickness of BN will lead to change in emissivity of the device and hence the responsivity.

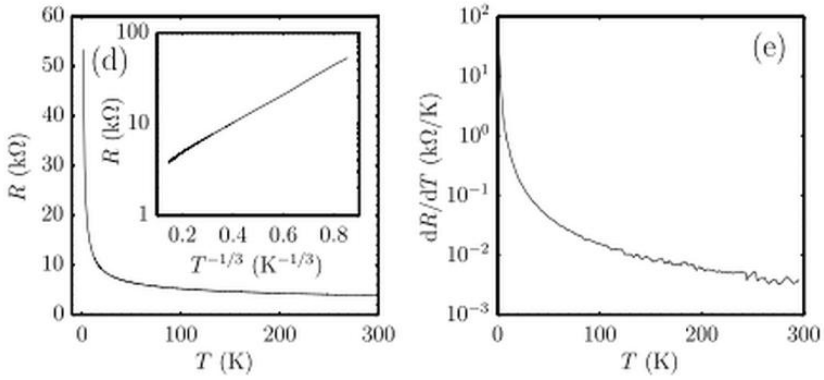

Figure 4.51 Temperature dependence of resistance of graphene nanoribbon based bolometer device [119].

Figure 4.52 (a) shows that the emissivity has an increasing trend with increasing thickness of BN layer from 20 nm to 2000 nm. The corresponding optical transmittance is found to decrease with increasing thickness of BN layer as shown in Figure 4.52 (b).

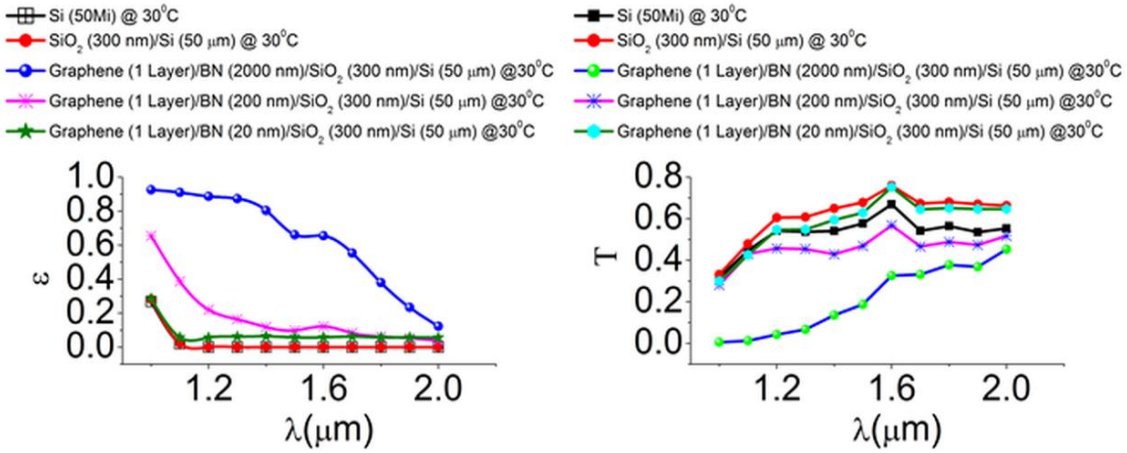

(a) (b)

Figure 4.52 Effect of variation of BN thickness on the (a) emissivity and (b) transmittance of bolometer structure configuration (Temperature in ºC) [115].

CHAPTER 5

RESULTS AND DISCUSSION

In this chapter, analyses of the results presented in Chapter 4 are presented with a view to compare them with the available literature. The modelling techniques, used in our calculations, are presented along with those in the literature.

5.1 Summary of Methods Used for Simulations

Table 5.1 Synopsis of Various Simulation Methods used in this Thesis

Simulation Methods	Molecular Dynamics (MD)	Density Functional Theory (DFT)	Linear Response: The Kubo Formula	Boltzmann Transport Equation (BTE)
Parameters	a)Tersoff /Airebo Potentials for simulating atomic interactions b)NVT thermostat for equilibration & NVE ensemble for NEMD c)Periodic boundary condition	a)Quantum mechanical calculations b)Energy & k-point convergence (20 X 20 X 1) c)Periodic boundary conditions d)Ballistic transport regime	a)It takes input from electronic band structure calculations by Quantum Espresso b)Dielectric matrix calculation within random phase approximation (RPA)	a)It takes input from electronic band structure calculations by Quantum Espresso b)Solving Boltzmann Transport equations with Constant Relaxation time approximation (25 fs)
Software used	LAMMPS	Quantum Espresso	YAMBO	Boltztrap
Properties	Thermal & Mechanical	Electronic	Optical	Thermoelectric

Table 5.1 shows the simulation methods used for simulating the thermal, mechanical, electronic, optical and thermoelectric properties of graphene and its

derivatives. The software tools namely LAMMPS (Large Scale Atomic/Molecular Massively Parallel Simulator), Quantum Espresso, YAMBO, and Boltztrap are available under GNU public license. These softwares have been installed in a Linux operating system.

5.2 Electronic Properties

Figure 5.1 a) shows the simulated electronic properties of pure graphene nanosheets, as per DFT calculations by Rani et al. [75] using VASP (Vienna Ab-initio Simulation Package) code. Figure 5.1 b) shows the simulated electronic properties of pure graphene nanosheets, as per our DFT calculations using Quantum Espresso.

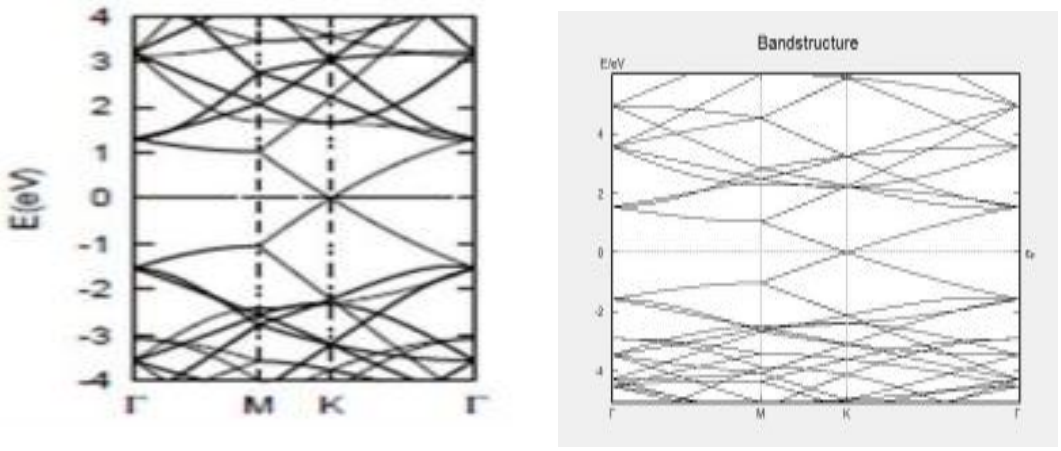

(a) (b)

Figure 5.1 (a) Simulated bandstructure of pure graphene nanosheet, as per literature [75], (b) Electronic bandstructure of pristine graphene, simulated in this thesis.

5.2.1 Analysis of Models for Electronic Properties

Graphene has been shown to have two-dimensional honeycomb structure. The results of electronic band structure calculations in literature reference [75] are shown in Figure 5.1. This analysis has been performed using geometry optimizations and electronic

bandstructure calculations by using the VASP (Vienna Ab-initio Simulation Package) code [214] based on density functional theory (DFT). This approach is based on an iterative solution of the Kohn-Sham equation [166] of the density functional theory in a plane-wave set with the projector-augmented wave pseudopotentials. In the calculations, the Perdew-Burke-Ernzerhof (PBE) [215] exchange-correlation (XC) functional of the generalized gradient approximation (GGA) has been used. The cutoff energy for plane-waves was set to 400 eV. The lattice constant optimizations are made by the minimization of the total energy of the structure.

The 5 × 5 supercell (consisting of 50 atoms) has been used to simulate the isolated sheet and the sheets have been separated by larger than 12 Å along the perpendicular direction to avoid interlayer interactions. The Monkhorst-Pack scheme has been adopted for sampling the Brillouin zone. The structures have been fully relaxed with a Gamma–centred 7 × 7 × 1 k-mesh. During these processes, except for the band determination, partial occupancies have been treated using the tetrahedron methodology with Blöchl corrections. For bandstructure calculations, the partial occupancies for each wavefunction were determined by applying the Gaussian smearing method with a smearing of 0.01 eV. For geometry optimizations, the internal coordinates were relaxed until the Hellmann-Feynman forces were less than 0.005 Å.

Figure 5.2 shows the bandstructure of pristine graphene and the corresponding density of states, as per our simulations. The geometry of the structure and their coordinates are generated using VMD (Visual Molecular Dynamics) software.

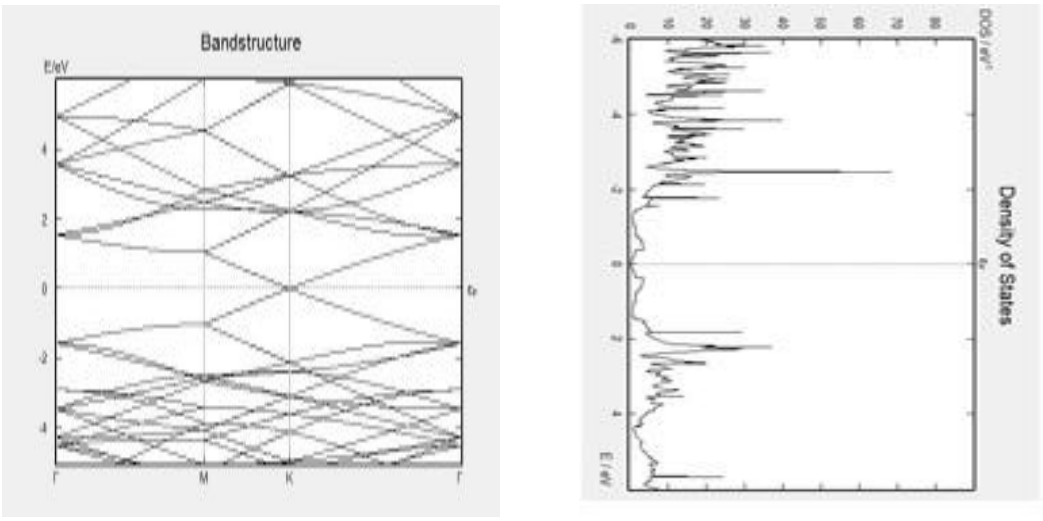

(a) (b)

Figure 5.2 (a) Simulated bandstructure of pure graphene, as per this thesis, (b) Corresponding density of states (DOS) for pure graphene.

The structural parameters i.e., lattice constant and coordinates are optimized by relaxation of the structure by using Quantum Espresso code based on DFT. Self-consistent (SCF) equations, proposed by the Kohn-Sham approach, have been iteratively solved for density functional theory in plane-wave set. The Perdew-Burke-Ernzerhof (PBE) exchange-correlation (XC) functional of the generalized gradient approximation (GGA) is applied. The non-SCF calculations have been performed by varying energy cutoff, Monkhorst-Pack grid parameters, and lattice constant. The optimized parameters obtained from non-SCF calculations are used to perform further simulations. Kinetic energy cutoff for wavefunctions has been chosen as 70 Ry, while the kinetic energy cutoff for charge density and potential has been set as 840 Ry (as a rule should be 8-12 times kinetic energy cutoff for wavefunctions). It is noted that the total energy of the system is minimum at this cutoff. Smearing with degauss 0.03 has been used considering

the semi-metallic nature of graphene. Energy convergence parameter has been set as 1.0E-8 Ry i.e., system converges once it reaches this energy level.

It can be observed that the Dirac point is at nil energy (0 eV) at K-point. This is exactly reported in the literature as per Figure 5.1. Also, DOS plot for pristine graphene is shown to have its minima at the Dirac point, as shown in Figure 5.2 (b).

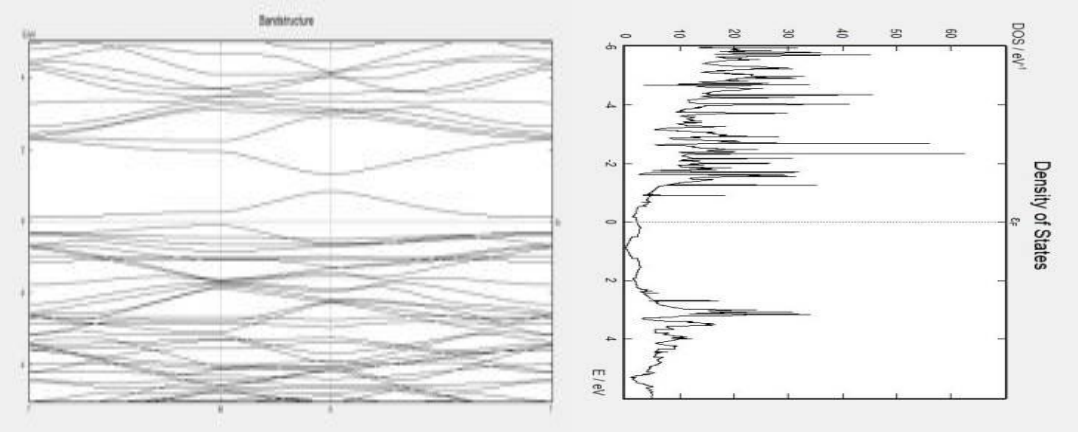

(a) (b)

Figure 5.3 (a) Simulated bandstructure of 4% boron doped graphene, (b) Simulated DOS for 4% boron doped graphene, as per calculations.

Further, doping of graphene nanosheet is carried out and its bandstructure as well as corresponding DOS is plotted as a function of concentration of dopants. Boron is a p-type dopant in graphene and it has diameter very close to carbon atoms. Hence, upon doping of graphene with boron, the boron atom undergoes sp^2 hybridization and there is no significant distortion in the structure of graphene sheet. The corresponding band structure for boron doped graphene is shown in Figure 5.3. However, there is change of adjoining bond lengths of boron atoms. It is observed that, with about 2% boron doping, the lattice parameter is 2.5794 Å as compared with about 2.455 Å for relaxed undoped graphene. As shown in Figure 5.4, there is a shift in Fermi level below the Dirac point

and the linear dispersion near the Dirac point is still intact. This shift is attributed to the electron deficient nature of boron in carbon lattice. Another important observation is the presence of bandgap in boron doped structure, to the extent of about 0.14 eV on 2% boron doping in graphene. Thus, graphene changes its semi-metallic nature to semiconducting.

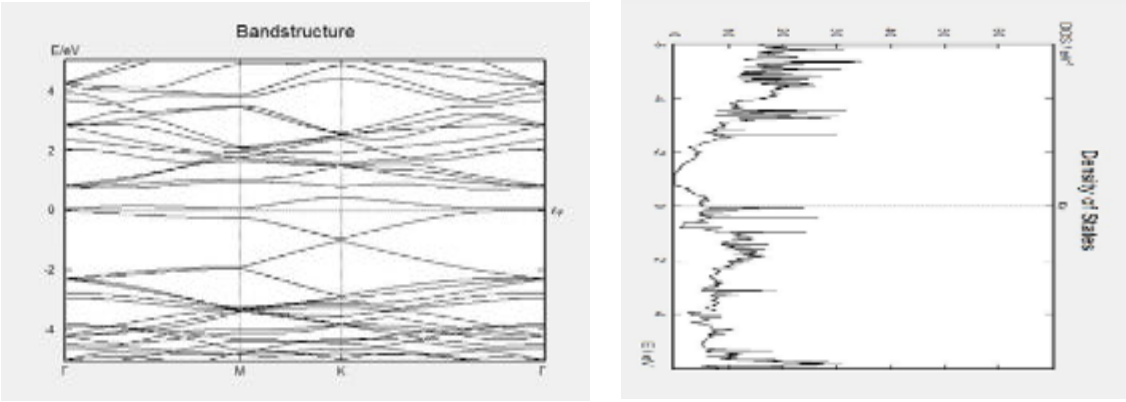

(a) (b)

Figure 5.4 (a) Simulated bandstructure of 4% nitrogen doped graphene, (b) Simulated DOS for 4% nitrogen doped graphene, as per calculations.

When graphene is doped with nitrogen atoms, there is a similar behavior as observed in B-doping. However, in this case, the bond length of C-N bonds is decreased. This results in the lattice parameter of about 4% nitrogen doped graphene sheet as 2.4338 Å. Thus, there is a reduction in the lattice parameter of graphene nanosheets with N-doping. Due to electron-rich nature of nitrogen atoms in graphene lattice, one observes that the Fermi level shifts by 0.7eV above the Dirac point. Due to broken symmetry of graphene sub-lattice on doping, there is a bandgap of about 0.14 eV with about 2% nitrogen doping.

Electrons in bilayer graphene are shown to possess an unusual property of being chiral quasiparticles, which is characterized by Berry phase 2π [216]. The low energy Hamiltonian of a bilayer describes chiral quasiparticles with a parabolic dispersion and Berry phase 2π. This is confirmed by quantum Hall effect (QHE) and Angle-Resolved Photoemission Spectroscopy (ARPES) measurements. The asymmetry between the on-site energies in the layers leads to a tunable gap between the conduction and valence bands.

As discussed in reference [216] and shown in Figure 5.5 (a), bilayer graphene is considered to consist of two coupled hexagonal lattices with inequivalent sites A1B1 and A2B2 on the bottom and top graphene sheets, respectively. They are arranged in accordance with Bernal (A2–B1) stacking. Every B1 site in the bottom layer lies directly below an A2 site in the upper layer, but sites A1 and B2 do not lie directly below or above a site in the other layer. Tight binding model of graphite has been applied by considering the Slonczewski–Weiss–McClure parameterization. The inversion symmetric pristine bilayer graphene can be seen as a zero bandgap semiconductor, as shown in Figure 5.5 (b).

Our calculated results for band structure of pristine bilayer graphene are presented in Figure 5.5 (c). The simulations have been performed using bilayer graphene structure similar to the one explained in the literature. The results are calculated using Quantum Espresso with implementation of DFT and plane wave sets. Similar to literature, it can be observed that pristine bilayer graphene is a zero bandgap semiconductor, with a possibility to modulate its bandgap by functionalization and doping.

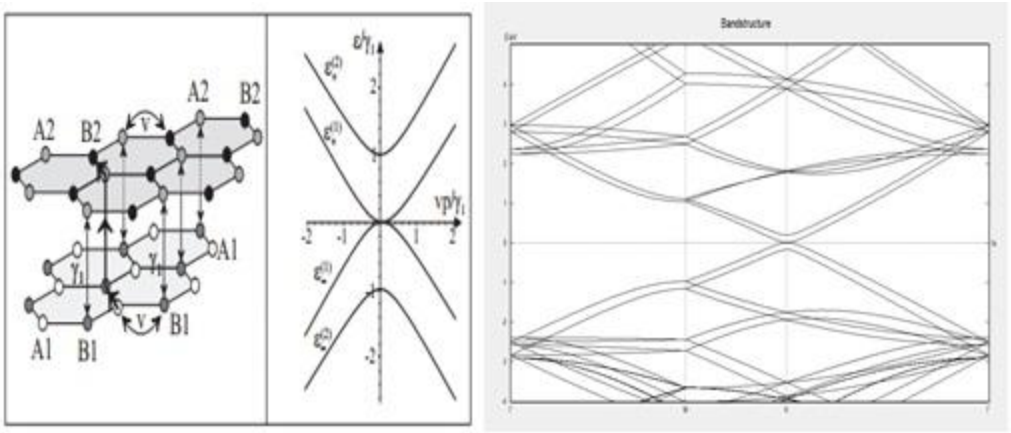

(a) (b) (c)

Figure 5.5 (a) Schematic of the bilayer lattice containing four sites in the unit cell: A1 (white circles) and B1 (grey) in the bottom layer, and A2 (grey) and B2 (black) in the top layer [216], (b) Schematic of the low energy bands near the K point obtained by taking into account intralayer hopping with velocity v, B1A2 interlayer coupling γ1, A1B2 interlayer coupling γ_3 [with $v_3/v = 0.1$] and zero layer asymmetry Δ, as per literature [216], (c) Simulated bandstructure of bilayer graphene, as per our calculations.

5.3 Optical Properties

Optical properties have been simulated by performing bandstructure calculations using Quantum Espresso along with a post-processing tool, YAMBO [104]. Yambo is a FORTRAN/C code for many-body calculations in solid state and molecular physics. Yambo relies on the Kohn-Sham wavefunctions generated by the DFT public code: Quantum Espresso.

Application of graphene in nano-photonics has been explored because of the unique combination of its optical and electronic properties. Visual transparency of graphene in the visible range of energy has led to its application as transparent coatings. Optical absorption of graphene is anisotropic due to difference in properties with light polarization along parallel and perpendicular to axis normal to the sheet. Experiments

have indicated that, as compared to graphite, there is red shift of absorption bands $\pi+\sigma$ electron plasmon and disappearance of bulk plasmons. As discussed in Chapter 3, Eberlein et al. [103] have shown that π and $\pi+\sigma$ surface plasmon modes in free-standing single sheets are present at 4.7 and 14.6 eV. These values exhibit substantial red-shift from the corresponding values in graphite.

5.3.1 Analysis of Models Used for Evaluating Optical Properties

As discussed in literature, as per ref. [100], VASP (Vienna *Ab-initio* Simulation Package) based on DFT has been used. The self-consistent Kohn-Sham equations of the density functional theory in a plane-wave set, with the projector-augmented wave pseudopotentials, have been applied. The Perdew–Burke–Ernzerhof (PBE) exchange-correlation (XC) functional of the generalized gradient approximation (GGA) has been adopted in the calculations. The plane-wave cutoff energy has been set to 400 eV. The 4×4 supercell (consisting of 32 atoms) has been used to simulate the isolated sheet. The graphene sheets have been separated by larger than 12 Å along the perpendicular direction in order to avoid interlayer interactions. The Monkhorst-Pack scheme has been used for sampling the Brillouin zone. The structures have been fully relaxed with a Gamma-centered 7×7×1 k-mesh. The partial occupancies have been treated using the tetrahedron methodology with Blöchl corrections. For geometry optimizations, the coordinates have been relaxed until the Hellmann–Feynman forces were less than 0.005 Å. Dielectric function $\varepsilon(\omega)$ has been calculated in the energy interval from 0 to 25 eV within the random phase approximation (RPA).

Figure 5.6 (a) shows the real part of the dielectric constant for pristine graphene. Results have been simulated as described above.

Figure 5.6 (b) shows the real part of dielectric constant for pristine graphene simulated by us. Quantum Espresso, with implementation of DFT and plane wave sets, has been used for bandstructure calculations. We have considered graphene sheet of width 2 nm and length 2 nm with periodic boundary conditions. The width of the vacuum layer, above the graphene layer, is assumed to be 13 Å in order to ensure that there is no interlayer interaction. The Monkhorst-Pack scheme has been used for sampling the Brillouin zone and it is found that 13 X 13 X 1 is the K-point mesh for which the energy of system is a minimum. Dielectric function $\varepsilon(\omega)$ has been calculated in the energy interval from 0 to 40 eV within the random phase approximation (RPA). It is found that there are two major features – one peak at around 5 eV corresponding to $\pi \rightarrow \pi^*$ and the other peak at about 14.6 eV corresponding to $\sigma \rightarrow \sigma^*$ interband transitions.

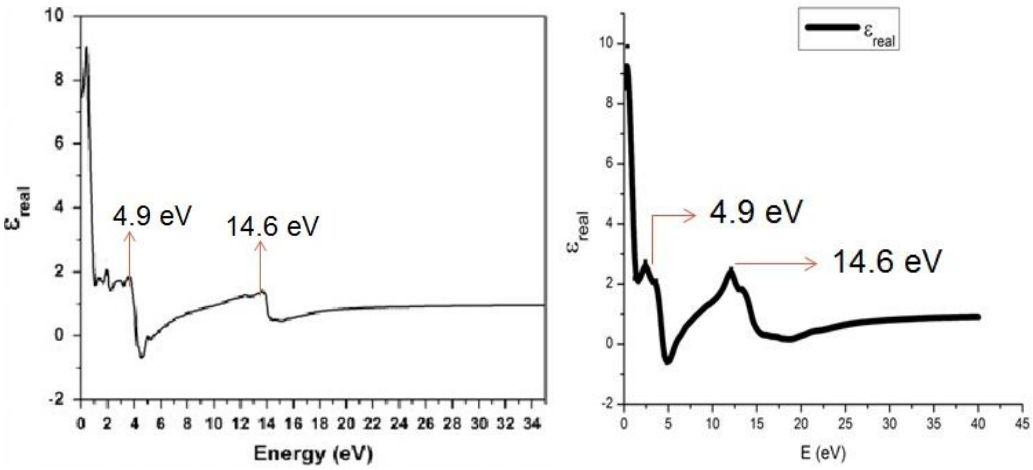

(a) (b)

Figure 5.6 (a) Simulated real part of dielectric function of pure graphene for $E \perp c$, as per literature [100], (b) Simulated real part of dielectric function of pure graphene, as per calculations. Peak at around 5 eV is corresponding to $\pi \rightarrow \pi^*$ and other peak at about 14.6 eV corresponding to $\sigma \rightarrow \sigma^*$ interband transitions.

Figure 5.7 (a) shows the imaginary part of the dielectric constant evaluated as per reference [100]. It is observed that the plot for E⊥c consists of a very significant peak at small frequencies (up to 5 eV) and also another peak structure of broader frequency range which starts from about 10 eV and has a weak intensity peak at 14 eV. Figure 5.7 (b) shows the imaginary part of the dielectric constant in accordance with our DFT simulations with Quantum Espresso in combination with post-processing tool – YAMBO. The procedure adopted for modeling and analysis is explained in the previous section.

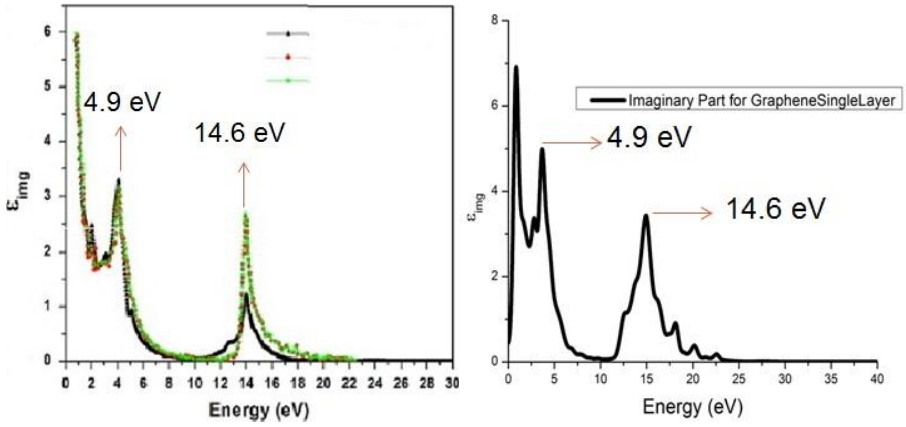

(a) (b)

Figure 5.7 (a) Simulated imaginary part of dielectric function of pure graphene for light polarization perpendicular to the plane of graphene sheet ($E \perp c$), as per literature [100] and, (b) Simulated imaginary part of dielectric function of pure graphene for light polarization perpendicular to the plane of graphene sheet ($E \perp c$), as per our calculations.

Once the verification of the model is established by comparison with the literature (experimental or simulated), the model is then extended to simulate the properties of graphene and zigzag GNR, as a function of number of layers. The results are presented in Figure 5.8 (a) and (b). It is observed that there is a rise in intensity of peaks at 4.9 eV and 14.6 eV. Other features such as shoulder in the range from 5-10 eV is constant

irrespective of the number of layers. Above 27.5 eV, the imaginary part of the dielectric constant shows nil value.

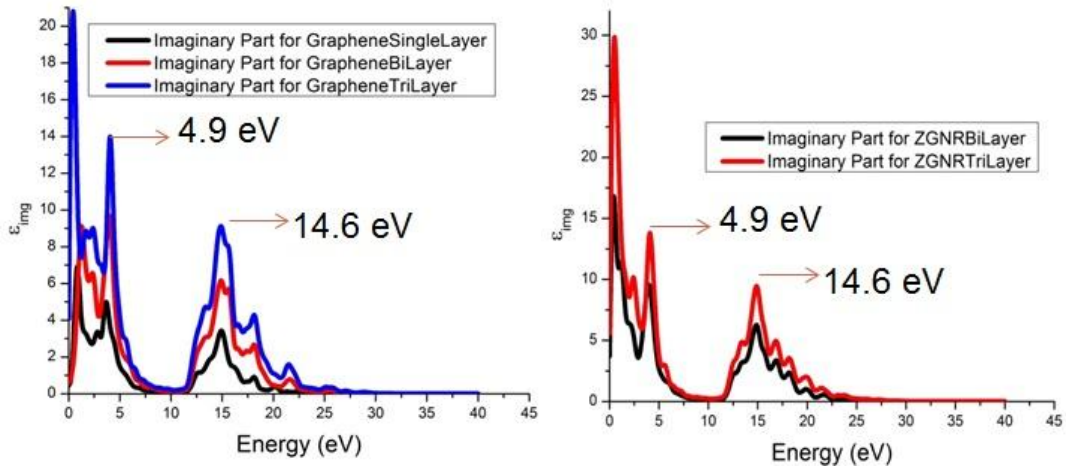

(a) (b)

Figure 5.8 (a) Simulated imaginary part of dielectric constant for single layer, bilayer and trilayer graphene, as per our calculations, (b) Simulated imaginary part of dielectric constant for bilayer and trilayer zigzag GNRs, as per our calculations.

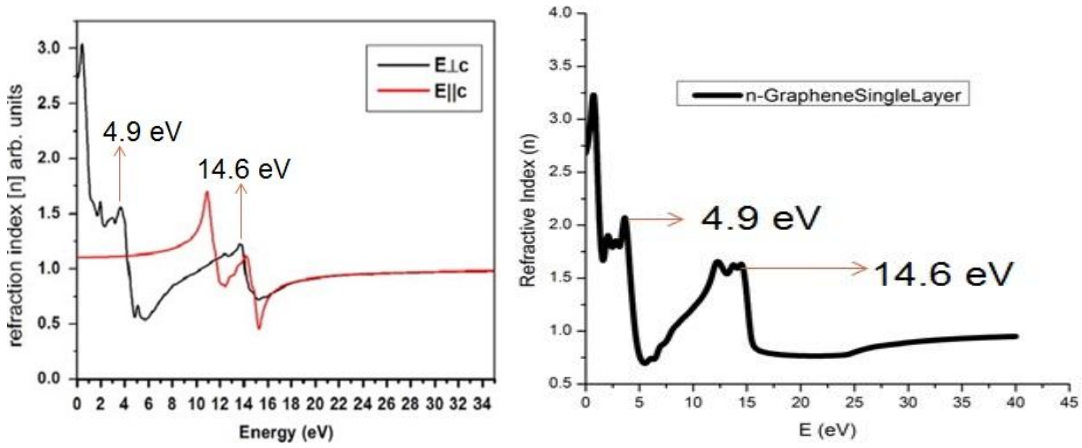

(a) (b)

Figure 5.9 (a) Simulated refractive index of graphene for light polarization perpendicular to the plane of graphene sheet ($E \perp c$) as well as ($E \| c$), as per literature, (b) Simulated refractive index of graphene for light polarization perpendicular to the plane of graphene sheet ($E \perp c$), as per our calculations.

Figure 5.9 (a) shows the trend of refractive index as a function of energy as per reference [100]. Refractive index follows similar trends as it has been evaluated from the corresponding dielectric functions. It shows minima positions at the maximum positions in the absorption spectra, as expected. Figure 5.9 (b) shows the trend of refractive index as a function of energy as per our calculations for the case of E ⊥ c. It is noted that similar trends are observed in the literature.

Figure 5.10 (a) shows the trends for refractive indices for armchair GNR as a function of energy for single layer, bilayer and trilayer armchair GNR. It is observed that the peaks are present at the same positions, i.e., 4.9 eV and 14.6 eV.

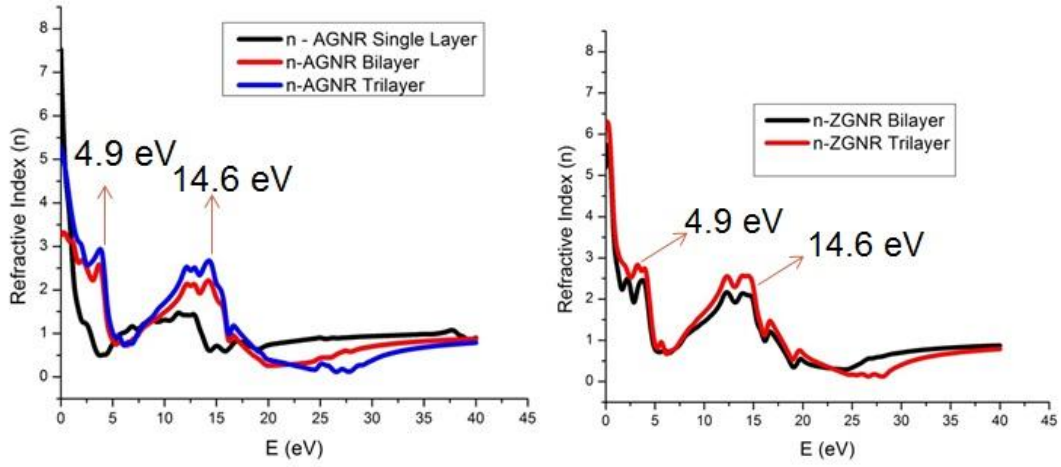

(a) (b)

Figure 5.10 (a) Simulated refractive indices of single layer, bilayer and trilayer armchair GNRs, (b) Simulated refractive indices of bilayer and trilayer zigzag GNRs, as per our calculations.

There is similar observation of rise in intensity of peaks at 4.9 eV and 14.6 eV. It can be seen that the shoulder locations are found at the same positions in the lower energy region from 5-15 eV, while beyond 15 eV, there is a slight rise in all the portions of the curves for refractive indices. Figure 5.10 b) shows the trends observed for zigzag

bilayer and trilayer GNRs. It can be observed that the curves follow similar trends as reported in earlier cases.

Figure 5.11 a) shows the extinction coefficient (k) as a function of energy presented in reference [100]. It is observed that there is an additional peak at about 1.2 eV in the curve for E ⊥ c, along with 4.9 eV and 14.6 eV, as reported in all the previous results. Figure 5.11 (b) shows the extinction coefficient (k) as a function of energy simulated as per our calculations. It is observed that similar peaks are observed at 1.2 eV, 4.9 eV and 14.6 eV for the orientation E ⊥ c.

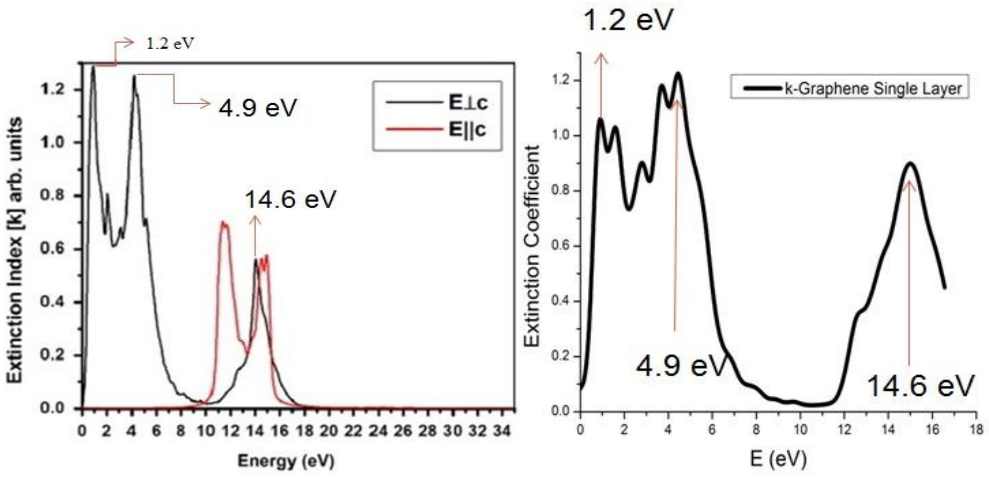

(a) (b)

Figure 5.11 (a) Simulated extinction coefficient as a function of energy for single layer graphene for light polarization perpendicular to the plane of graphene sheet ($E \perp c$) as well as ($E \| c$), as per literature [100], (b) Simulated extinction coefficient as a function of energy for single layer graphene for light polarization perpendicular to the plane of graphene sheet ($E \perp c$), as per our calculations.

Figure 5.12 (a) shows the trends for single layer, bilayer and trilayer graphene as a function of energy. It can be seen that there is rise in intensity at all the portions of the curve except the shoulder between 8-12 eV. Figure 5.12 (b) shows the trends for bilayer and trilayer zigzag GNRs as a function of energy.

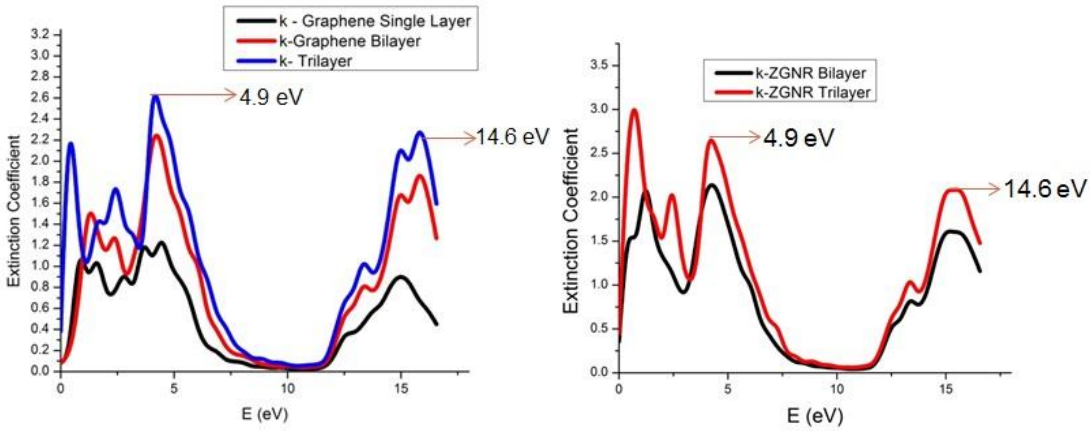

(a) (b)

Figure 5.12 (a) Simulated extinction coefficient for single layer, bilayer and trilayer graphene as a function of energy, as per our calculations, (b) Simulated extinction coefficient for bilayer and trilayer zigzag GNRs, as per our calculations.

5.3.2 Experimental Observations of Optical Properties of Graphene

Kravets et al. [217] have demonstrated the optical transparency of two dimensional system with a symmetric electronic spectrum by a fine structure constant. They have measured ellipsometric spectra and extracted the optical constants of a graphene layer.

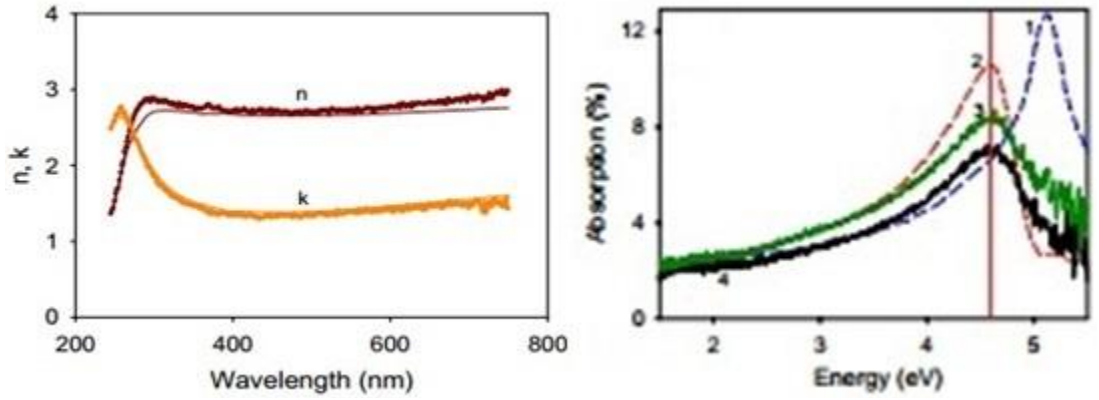

(a) (b)

Figure 5.13 Experimental measurement of variable angle spectroscopic ellipsometry of graphene on amorphous quartz substrate (a) Reconstructed optical constants of graphene are shown, (b) Absorption spectra of single layer graphene. Solid curves 3 and 4 are experimental data. Dashed curves 1 and 2 are calculations from reference [218].

There is a reconstruction of the electronic dispersion relation near the K point using optical transmission spectra. Spectroscopic ellipsometry analysis of graphene placed on amorphous quartz substrates has been reported in Figure 5.13 [217, 218]. A pronounced peak in the ultraviolet absorption at 4.6 eV is observed because of a van Hove singularity in the DOS of graphene. The peak has been found to be asymmetric and downshifted by 0.5 eV. The downshift is attributed to possible excitonic effects. The symmetric peak at 5.2 eV (curve 1) is expected by non-interacting theory, whereas interaction effects should result in asymmetric peak downshifted to 4.6 eV (curve 2) [217].

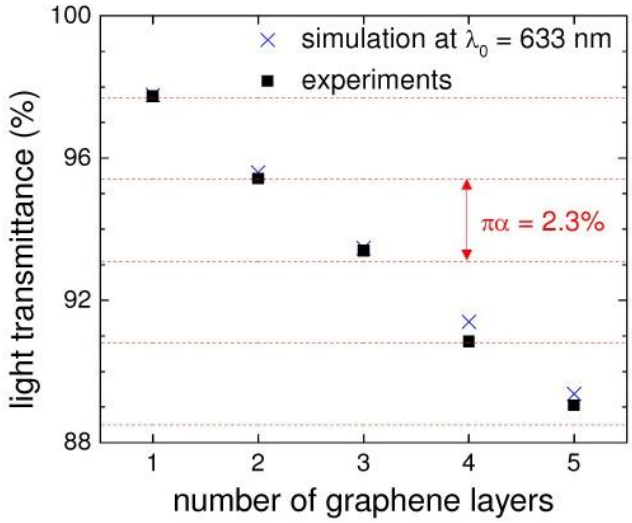

Figure 5.14 Simulated transmittance of light at λ_0 = 633 nm (crosses) and measured transmittance of white light (squares) [18] as a function of the number of graphene layers, as per reference [219]. The dashed lines correspond to an intensity reduction by $\pi\alpha$ = 2.3% with each added layer, where α is the fine structure constant [219].

Wu et al. [219] have explored the sensitivity of graphene based optical biosensor with analysis of the optical properties of graphene. Experimental measurements by Nair et al. [18] on light transmission through suspended graphene membranes showed that the transparency of graphene is a universal constant and independent of the wavelength.

On the basis of measurements, the dielectric function ε or complex refractive index n of graphene in the visible range has been obtained within the framework of Fresnel coefficients calculation:

$$n = 3.0 + i\,\frac{C_1}{3}\lambda_0 \qquad (5.1)$$

Where, the constant $C_1 \approx 5.446\,\mu\text{m}^{-1}$ is implied by the opacity measurement by Nair [18], and λ_0 is the vacuum wavelength. In order to validate this experimental model, Wu et al. [219] used full wave electromagnetic field simulation in frequency domain using CST MICROWAVE STUDIO®2009. In the calculations, the thickness of graphene $d = L \times 0.34$ nm (where L is the number of graphene layers) is sandwiched between two vacuum blocks. The light transmittance through monolayer graphene is about 97.7%, which is related to the fine structure constant α by $\pi\alpha$ = 2.3%, as shown in Figure 5.14. Thus, monolayer of graphene would absorb 2.3% of the incident light. The simulated transmittance is also shown to follow the same trends and it is shown to absorb 2.3% of the incident light for each added layer of graphene. The measured optical spectra of graphene enable one to use the complex refractive index for prediction of the optical behavior of graphene for surface plasmon resonance biosensing.

5.3.3 Experimental Measurements of Emissivity of Graphite

In most of the applications of thermography, relative temperature variations are of interest. Variation of measured intensity can be interpreted in terms of temperature variations or emissivity change of the surface with respect to its surroundings. Typical

areas of application of emissivity measurements are oxidation of metals and semiconductors or erosion of materials on reentry of vehicles from space. Knowledge of emissivity is the first step for determination of accurate radiation temperatures.

The method of comparison of radiation is known to be a well suited method for measuring emissivities that are essential for temperature measurements. The sample surface radiance is measured by using calibrated detector and the surface temperature can be estimated independently. Temperature difference between sample surface and black body can be calculated using heat conduction equation. Accuracy in determination of temperature difference depends on the thermal conductivity of the material, which should be either known or measured [220].

For detectors with linear operation, the emittance ε can be evaluated as the ratio of detector signals measured from the sample (U_s) to the signal measured at the black body (U_{BB}) at the same temperature, as per Equation (5.2).

$$\varepsilon = \frac{U_s(T_s)}{U_{BB}(T_s)} \qquad (5.2)$$

The radiation from the sample consists of contribution from the direct radiation as well as reflected radiation. The contribution from reflection can be either calculated or determined experimentally. The samples in this study have been 15 mm in diameter and 3-6 mm thick. The sample is heated using electron gun and the vacuum in the chamber is $< 0.7 \times 10^{-4}$ mbar. Linear pyrometer is used in the measurements in lower wavelength range and thermal detector is used for determination of emissivity in the higher wavelength range > 1.3 μm.

Spectral emissivity has been measured at temperatures in the range of 1100 K to 2000 K and is presented in Figure 5.15 (a). No systematic temperature dependence has been noted. The rate of decrease of emissivity, at longer wavelengths, is reported to be much higher for composite samples as compared with pure graphite. The reason for lower value of emissivity for composite samples is attributed to the extreme surface smoothness of fiber bundles. In contrast to the temperature independent nature of spectral emissivity, the total normal emissivity increases with increasing temperature. As per Wien's displacement law, lower wavelength corresponds to higher radiation intensity. Hence, the total (integrated) emissivity increases with temperature if the spectral emissivity increases with reduction in wavelengths. Figure 5.15 (b) shows the experimental trends for total normal emissivity as a function of temperature.

Figure 5.15 (c) shows the simulated trends for spectral emissivity of 5000 μm thick graphite at room temperature. Simulated trends for spectral emissivity for various thicknesses of natural diamond, at room temperature, are also included for comparison. It is observed that the values of emissivity of graphite at room temperature are much lower than the reported experimental values for higher temperatures. In case of natural diamond, the emissivity is found to be increasing with increase in thickness at room temperature. Emissivity of natural diamond is found to be almost independent of wavelength for thicknesses below 1000 μm, in the wavelength range of 6-20 μm. While, for higher thicknesses > 1000 μm of natural diamond, there are some variations in the emissivity values.

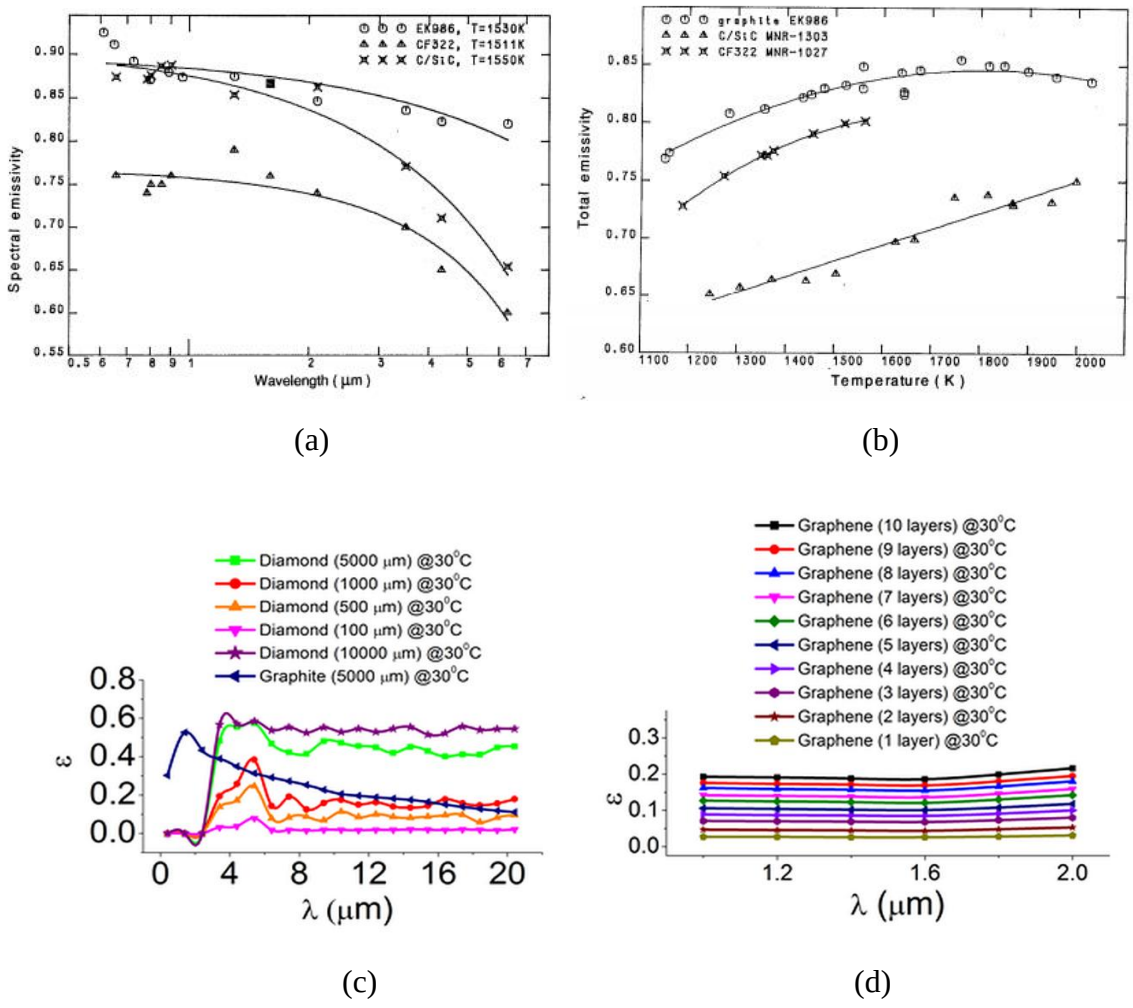

Figure 5.15 (a) Experimental normal spectral emissivity of graphite (EK986) carbon/carbon (CF322) and carbon/silicon carbide (C-SiC) composites at higher temperature, as per literature [220], (b) Total normal emissivity of graphite (EK986), carbon/carbon (CF322), and carbon/ silicon carbide (C-SiC) composites [220], (c) Simulated normal emissivity versus wavelength for diamond and graphite [115], (d) Emissivity versus wavelength for graphene up to 10 layers (temperature in ºC) [115].

Figure 5.15 (d) shows the simulated trends of emissivity for graphene (1-10 layers) in the wavelength range of 0.4 – 2.0 μm. It is observed that the emissivity increases with increasing number of layers of graphene, independent of the wavelength. Increase in emissivity of graphene with increase in thickness is attributed to the higher absorption with increasing number of layers.

5.4 Mechanical Properties

Graphene is reported to have intrinsic strength exceeding any other material as well as other carbon allotropes. Hence, there is a motivation for application in carbon fiber reinforcements in advanced composites. However, the high theoretical values of mechanical properties, reported in the literature, are very difficult to realize experimentally. Recent experimental studies have made possible use of single layer graphene in applications.

Atomic force microscope (AFM) nanoindentation has been used to determine the mechanical properties of graphene as per reference [53]. Advantages of AFM for testing properties of graphene over CNT are: precise definition of sample geometry, 2D structure is less sensitive to presence of defects, and sheet is clamped around entire hole circumference, which is different from CNTs. Figure 5.16 shows the nanoindentation study of 5 x 5 mm array of circular wells patterned on Si substrates with 300 nm SiO_2 epilayer by nanoimprint lithography and reactive ion etching. Flakes of graphene have been mechanically deposited on the substrate. Graphene has been shown to adhere with vertical wall of the hole for 2-10 nm due to van der Waals attraction to the substrate.

Prior to the start of indentation, graphene membranes has been scanned using AFM non-contact method. AFM tip has been placed within 50 nm of the center. Mechanical testing has been performed at a constant displacement rate, followed by reversal of load. The repetition of such cycles for several times for each film tested showed no hysterisis data. This indicates the elastic behaviour of graphene film around the periphery of the well. Followed by studies of elastic behavior of graphene films, the samples were subjected to indentation till failure. Using ab initio values for in-plane

stiffness and flexural rigidity, it has been reported that the energy from bending the graphene membranes is about three orders of magnitude less than the energy from in-plane strain. Images of suspended graphene membranes are shown in Figure 5.16.

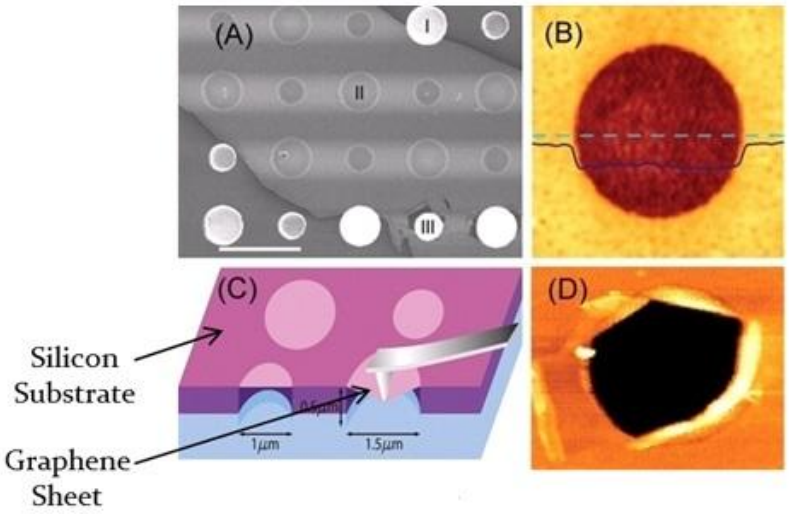

Figure 5.16 Images of suspended graphene membranes. (A) Scanning electron micrograph of a large graphene flake spanning an array of circular holes 1 μm and 1.5 μm in diameter. Area I shows a hole partially covered by graphene, area II is fully covered, and area III is fractured from indentation. Scale bar, 3 μm. (B) Noncontact mode AFM image of one membrane, 1.5 μm in diameter. The solid blue line is a height profile along the dashed line. The step height at the edge of the membrane is about 2.5 nm. (C) Schematic of nanoindentation on suspended graphene membrane. (D) AFM image of a fractured membrane [53].

The resulting force versus displacement curve for loading/unloading is shown in Figure 5.17 (a). Using numerical simulations and molecular dynamics simulations, it has been shown that the elastic response of graphene nansheets is non-linear. Force versus displacement behavior has been approximated as per Equation (5.3).

$$F = \sigma_0^{2D}(\pi \mathrm{a}^2)\left(\frac{\delta}{a}\right) + E^{2D}(q^3 a)\left(\frac{\delta}{a}\right)^3 \qquad (5.3)$$

Where, F is the applied force, δ is the deflection at the center point, σ_0^{2D} is the pre-tension in the film, ν is Poisson's ratio [taken as 0.165, the Poisson's ratio for graphite in the basal plane], and $q = 1/(1.05 - 0.15\nu - 0.16\nu^2) = 1.02$ is a dimensionless constant. The solid line in Figure 5.17 (a) shows the least-squares curve fit of one set of experimental data, based on Equation (5.3), taking σ_0^{2D} and E^{2D} as free parameters. The closeness of the fit has been considered to validate the appropriateness of this model.

Figure 5.17 (b) shows the typical breaking curves for different indenter tip radii and well diameters. The graphene film has been reported to be hanging around the edge of the hole without significant sign of slippage or irreversible deformation prior to catastrophic failure. This indicates the fracture in the graphene film initiated at the indentation point. The indentation forces in this process have been sufficient to break Si AFM tips. However, the diamond tips used in this experiment have been confirmed by TEM to have no damage.

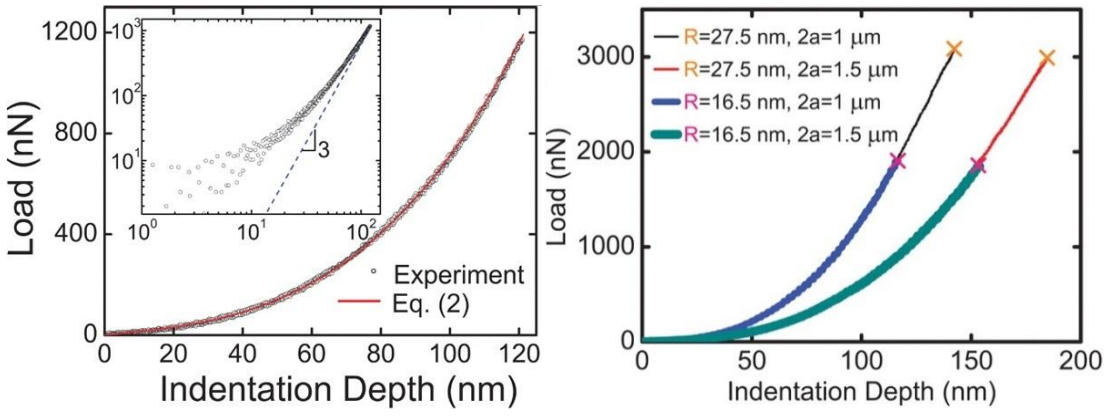

(a) (b)

Figure 5.17 (a) Loading / unloading curve and curve fitting to Equation (5.3). The curve approaches cubic behavior at high loads (inset), (b) Fracture test results. Four typical tests, with different tip radii and film diameters; fracture loads are indicated by × marks. Breaking force depends strongly on tip radius but not on sample diameter [53].

Wang et al. [190] have performed molecular dynamics study on nanoindentation experiments for single layer rectangular graphene films with four clamped edges. Load versus displacement curves have been presented and the effects of indenter radii, loading speeds and aspect ratios of graphene film on the mechanical properties have been discussed. Youngs' Modulus and strength of single layer graphene film have been determined and the values are 1.0 TPa and 200 GPa, respectively. Graphene film is shown to rupture at a critical indentation depth, as shown in Figure 5.18.

A spherical diamond indenter has been used to simulate the nanoindentation (as per Figure 5.18) [190]. The upper ball in Figure 5.18 (a) is diamond indenter. It is considered to be rigid, so that there are no changes in the atomic configuration of the indenter during the molecular dynamics simulation. The lower layer is single layer rectangular graphene.

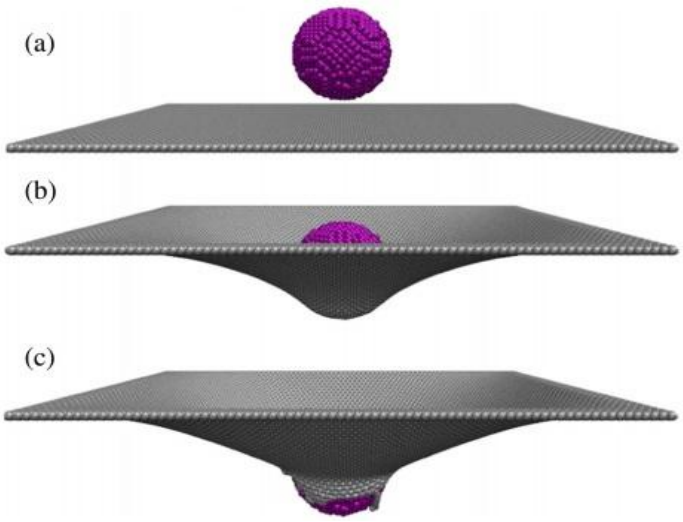

Figure 5.18 Atomic configuration of the system model during the nanoindentation experiment. (a) The origin model, (b) the state during the loading process, and (c) at rupture state, as per literature [190].

The interatomic interaction of carbon atoms in the graphene layer have been described by AIREBO (Adaptive Intermolecular Reactive Empirical Bond Order) potential. AIREBO potential has been shown to consider multi-body potential effects and local atomic circumstance effects. AIREBO introduces long-range interaction and torsion term. This is in contrast to the Tersoff-Brenner potential. Hence, AIREBO potential is found to be more accurate in evaluation of Youngs' modulus as well as breaking and reforming of bonds in carbon atoms of graphene layer. The cutoff parameter of AIREBO potential has been considered as 2 Å, which helps to avoid the influence of non-physical explanations with improper cutoff on fracture mechanics. Canonical ensemble (NVT) has been considered during molecular dynamics simulations and the temperature has been maintained at 0.01 K. Nosé-Hoover thermostat has been used for avoiding the complex effects of atomic thermal fluctuations and timestep has been set as 0.001 ps. Initially, the system has been relaxed and equilibration has been maintained to keep system at lowest energy state during the simulation.

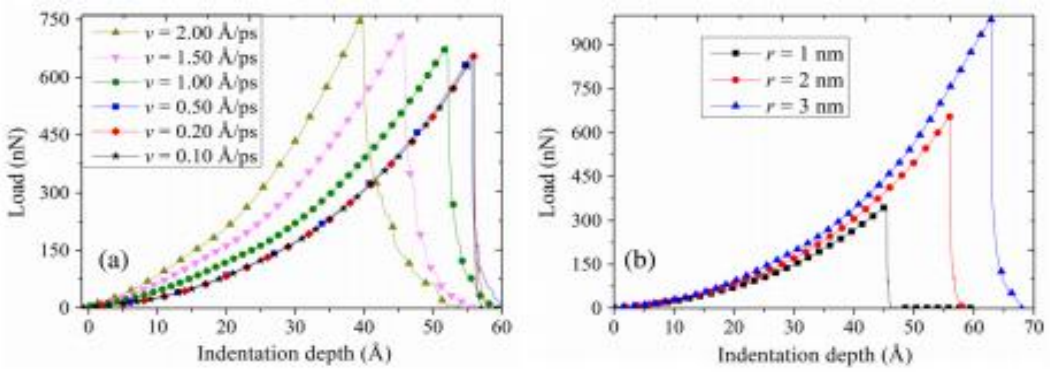

(a) (b)

Figure 5.19 Comparison of load versus indentation depth for different parameters. (a) The indenter is loaded at different loading speeds between 0.10 and 2 Å/ps. (b) The indenter is loaded with different indenter radii of 1, 2, and 3 nm, as per literature [190].

Figure 5.19 (a) shows the effect of various indenter speeds and Figure 5.19 (b) shows the effect of various diameters of indenter on the load versus displacement plots. It is found that, when the loading speed is higher than the critical value, with the increase of speed, the maximum load increases rapidly; simultaneously, the critical indentation depth decreases rapidly. The higher is the indenter loading speed, the lesser is the time required for the indenter to pass through the graphene sheet. This leads to higher load and lower indentation depth than the ones at lower speed. Figure 5.19 (b) indicates that the radii of the spherical indenter affects the indentation depth. It is noted that critical indentation depth increases with increase in the indenter radius.

Figure 5.20 (a) shows our simulation of the indentation of a rectangular single layer graphene sheet. We have considered a molecular dynamics simulation with two different interatomic potentials describing interactions of carbon atoms in graphene layer, one with AIREBO potential and other with Tersoff-Brenner potential. The indenter is considered to be spherical rigid type with force constant as 1,000 eV/ Å. Initially the system is relaxed and the structure is equilibrated during the simulation. The atoms at the edges of the graphene sheet (about 10 Å on each edge) are kept fixed during the simulation in order to provide physical support to the system during indentation. The timestep is considered as 1 fs and the cutoff distance for the AIREBO potential is considered to be 2.5 Å. We have considered NVT ensemble (canonical) and system temperature is maintained at 300 K during the simulation. Berendsen thermostat has been applied to maintain the constant temperature of the system. As noted in the literature, we found that AIREBO potential has more accuracy than Tersoff-Brenner type interatomic potential for calculating the indentation force. The higher values of indentation force for

the AIREBO potential are attributed to the inclusion of additional long-range interaction term and torsion in the case of AIREBO potential, which is absent for Tersoff-Brenner type potential.

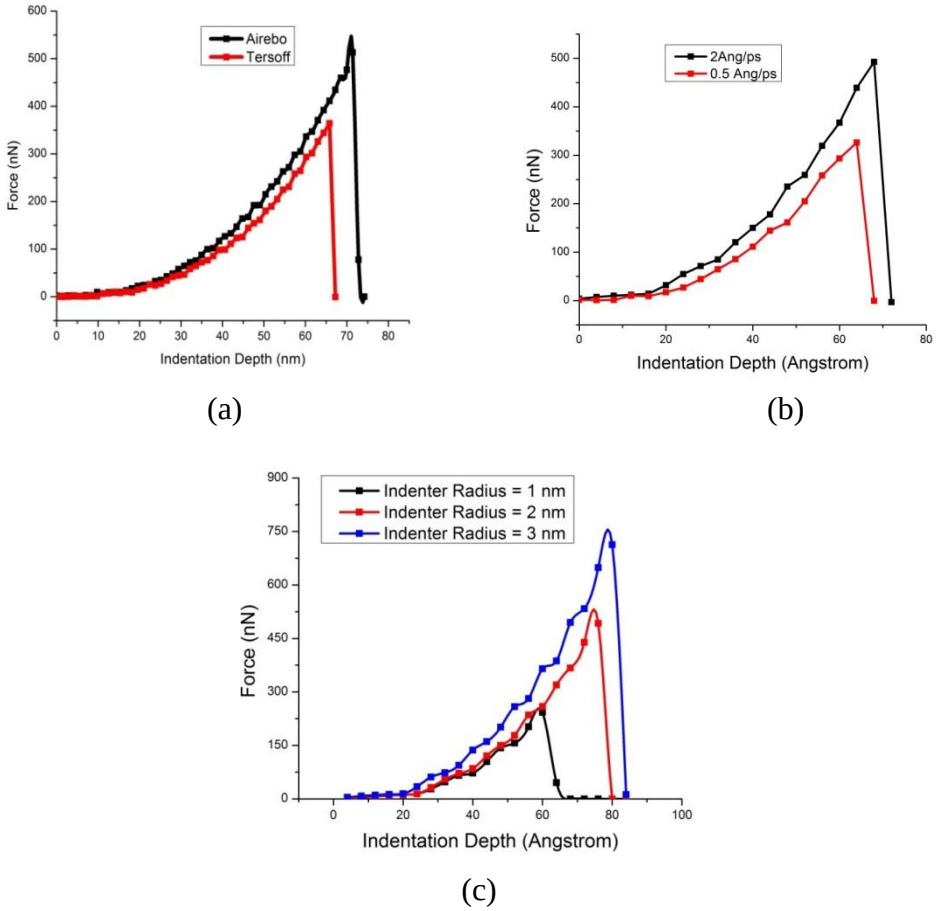

Figure 5.20 (a) Comparison of simulated force versus indentation depth using Tersoff-Brenner and AIREBO interatomic potentials, as per our calculations, (b) Simulated force exerted by indenter as a function of indentation depth for variation in speed of indenter, (c) Simulated force exerted by indenter as a function of indentation depth for variation of indenter radius, as per our calculations.

Figure 5.20 (b) shows the effects of variation of speeds of the diamond indenter on the force versus displacement curves. It is noted that the higher is the indentation speed, the higher is the slope of the curve. This is consistent with the observation in the literature. Figure 5.20 (c) shows the effect of variation of indenter diameter on the force

versus displacement curves. It is found that the higher is the indenter radius for the same aspect ratio of the graphene sheet, the higher is the slope of the force versus indentation depth curves. This indicates that the system will show higher stiffness with higher indenter radius. However, the elastic moduli, evaluated from the force versus indentation depth curves, are found to be in the range of 0.9-1.2 TPa, which are also noted from various AFM nanoindentation experiments in the literature. Thus, our model is verified with the reported literature. The non-linear elastic response of graphene is evident from the curves in Figure 5.20.

Figure 5.21 shows the comparison of nanoindentation behaviour of single layer and bilayer graphene. The simulation methodology is as explained in earlier cases. It can be noted that the values of indentation force are much higher (almost double) in case of bilayer graphene as compared to single layer graphene. It is seen that the values of indentation force are rapidly increasing with increasing depth of indentation. Higher stiffness values of bilayer graphene are evident from the curves in Figure 5.21.

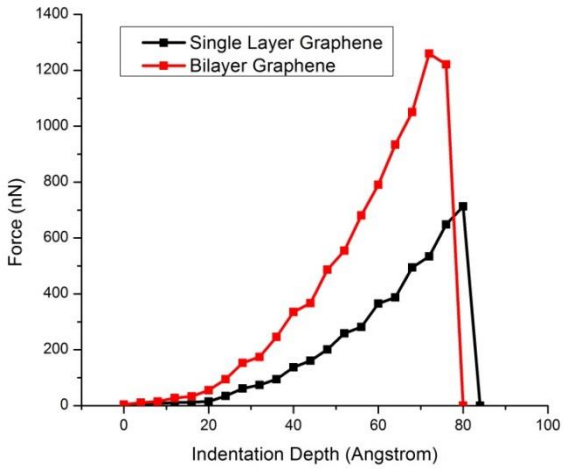

Figure 5.21 Simulated force versus indentation depth trends for single layer and bilayer graphene, as per our calculations.

Zandiatashbar et al. [221] have studied the effects of defects on the intrinsic strength and stiffness of graphene. It is reported that, even with high density of sp^3 defects in graphene, the two-dimensional elastic modulus is maintained. The defective graphene in sp^3 regime is noted to have breaking strength ~ 14% smaller than its pristine counterpart. In contrast to this, the mechanical properties of graphene have been reported to have significant drop in the vacancy defect regime. They have provided a mapping between Raman spectra of defective graphene sheets with its mechanical properties.

In experimental studies, $1 \times 1\ cm^2$ array of circular wells, with diameters ranging from 0.5 to 5 μm, has been patterned on Si chip with a 300-nm SiO_2-capping layer, by means of photolithography and reactive ion etching. Suspended membranes have been created by mechanical exfoliation of graphene on the patterned substrate. Elastic stiffness and breaking strength have been evaluated using AFM nanoindentation with a diamond tip indenter, as shown in Figure 5.22.

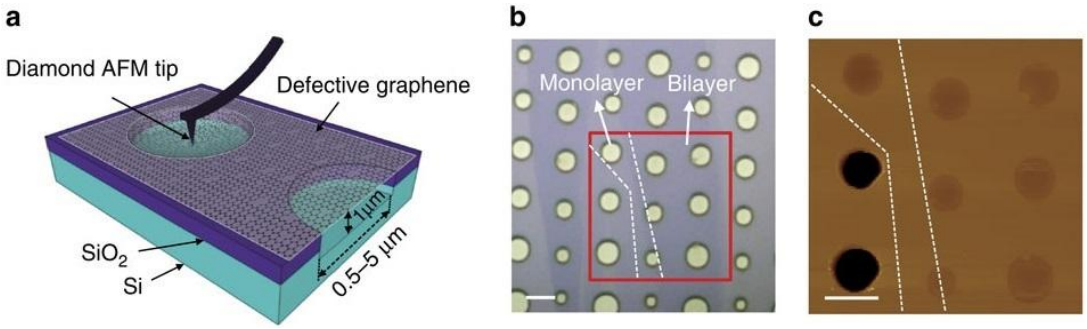

Figure 5.22 (a) Schematic representation of atomic force microscopy (AFM) nanoindentation test on suspended graphene sheets with defects. Graphene sheet is suspended over a hole with diameters ranging from 0.5 to 5 μm and depth of ~1 μm. (b) Optical micrograph of exfoliated graphene sheets suspended over holes. White-dashed line indicates the boundary of each layer. (c) Non-contact mode AFM image of suspended graphene sheet obtained from the red square box region marked in (b). Scale bars, 3 μm [221].

Defects in graphene sheet have been induced using tabletop oxygen plasma etcher. Some other methods, reported in the literature, for inducing defects in graphene are weak oxidation by ion bombardment, oxygen plasma or ultraviolet irradiation to etch graphene. The etch rate in oxygen plasma has been reported to be ~ 9 layers per minute at a chamber pressure of ~ 215 mTorr. This rate is much faster as compared to the other approaches. Raman spectroscopy has been used to characterize defective graphene sheets. Figure 5.23 (a), (b) and (c) show the images of AFM nanoindentation of the graphene sheet at various stages. Figure 5.23 (d) is the typical force versus indentation depth curve for a defective graphene sheet. It has been reported that the breaking stress shows higher sensitivity to defects than the elastic stiffness, irrespective of the type of defects. Principal finding of this study has been to show that graphene can maintain large fraction of its pristine strength and stiffness even in the presence of sp^3 type defects.

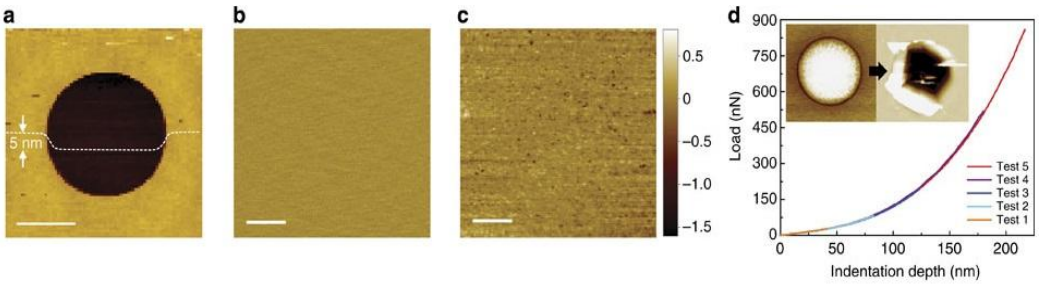

Figure 5.23 (a) AFM image of a graphene sheet fully covering a hole. High-resolution AFM images of suspended graphene sheet (b) before and (c) after oxygen plasma exposure of 55 s. The plasma treatment leaves the surface pock-marked with a multitude of nanopores that are several nm in size (the dark spots in the image represent the nanopores). (d) Typical force versus displacement curves of AFM nanoindentation test for defective graphene exposed to oxygen plasma for 30 s. Tests are repeated at increasing indentation depths until the sample breaks. The curves fall on top of each other (no hysteresis), which indicates no significant sliding or slippage between the graphene membrane and the substrate. The AFM images in the inset of d show a graphene sheet before and after fracture. Scale bars, 1 μm (a); 100 nm (b,c) [221].

Figure 5.24 shows the aberration corrected high resolution TEM (AC-HRTEM) image of defective graphene lattice with different oxygen plasma times. These images confirm that, in sp^3 defect regime, sp^3 point defects in the form of oxygen adatoms are generated. With higher plasma exposure, carbon atoms are etched from the lattice. This leads to the formation of nano-cavities or nano-pores in the lattice.

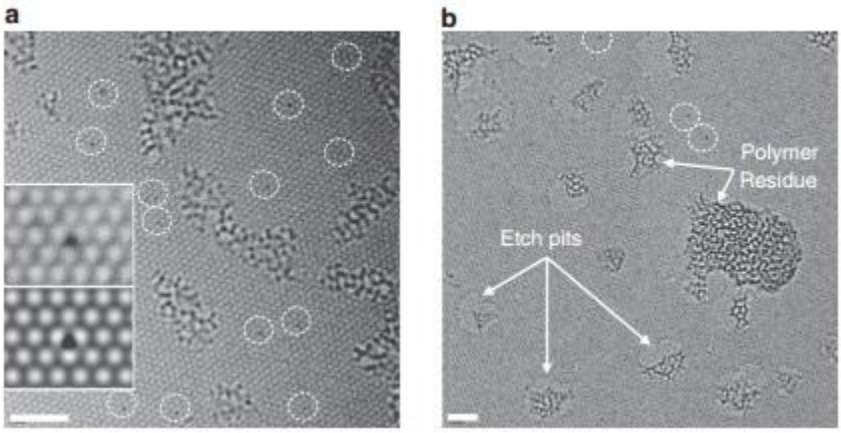

Figure 5.24 AC-HRTEM characterization of defect structures. Images of a typical graphene sheet in (a) sp^3-type and (b) vacancy-type defect regime. Polymer residue associated with the transfer process onto the TEM grid is indicated by arrows. The defective graphene of the vacancy-type defect regime contains an abundance of nanocavities (that is, etch pits), while the defective graphene of the sp^3-type defect regime shows a contrasting absence of such cavities. The black dots circled with dashed lines in (a) and (b) are oxygen adatoms. The insets of (a) show the experimentally obtained TEM image (upper) and the corresponding simulated image (lower) of oxygen atoms bonded to carbon forming sp^3 point defects. Scale bars, 2 nm (a,b) [221].

5.5 Thermal Conductivity

The continuing progress in the electronic industry has led to miniaturization of circuit components. This is leading to challenges in the thermal management in electronic devices and hence the immense interest in the thermal properties of materials used in nanostructured form in electronic components and circuits. The room temperature

thermal conductivity of carbon based allotropes have a very wide range – of over five orders of magnitude – least for amorphous form of carbon to the highest in carbon nanotubes and graphene. A field of special interest has been the size dependence of thermal conductance of graphene and its derivatives [144].

Heat conduction in carbon materials is usually dominated by phonons, even in case of graphite (having metallic properties). This is attributed to the strong covalent sp^2 bonding which results in efficient heat transfer by lattice vibrations. The thermal conductivity of both suspended as well as supported graphene has been studied by molecular dynamics simulations. Length dependence has been reported in the case of suspended single layer graphene. The thermal conductivity of supported single layer graphene has been found to be independent of its length. Figure 5.25 shows the simulated thermal conductivity of suspended single layer zigzag graphene as a function of its length at room temperature, as per reference [222].

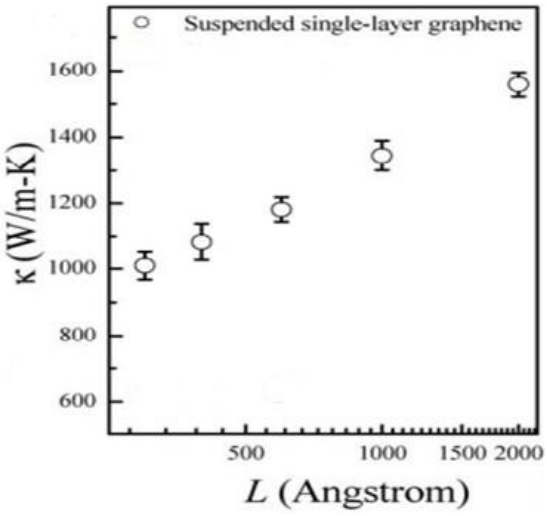

Figure 5.25 Simulated thermal conductivity κ of suspended (empty circle) and single-layer graphene versus the length L at room temperature, as per literature. Here, zigzag graphene with fixed width W=52 Å is used [222].

In this study, MD simulations have been performed using LAMMPS package. Tersoff potential with optimized potential parameters has been used in the simulations to describe C-C interatomic interactions. Graphene interlayer interactions have been modeled using van der Waal (vdW) type Lennard-Jones potential. Non-equilibrium molecular dynamics (NEMD) simulations with Langevin heat bath have been used to study thermal transport in graphene structures.

Figure 5.26 shows our calculated results of the thermal conductivity for pristine graphene nanosheets as well as armchair and zigzag GNRs, as a function of their lengths, with NEMD simulations. All the structures, considered for these simulations, have a width of 2 nm. It is seen that κ_p increases as a function of length for the suspended graphene structures, as reported in literature. As the sample size increases, more low-frequency acoustic phonons can be excited and contribute to thermal conduction, resulting in a length-dependent behaviour. Extremely long-wavelength low-frequency acoustic phonons have ballistic transport mechanism.

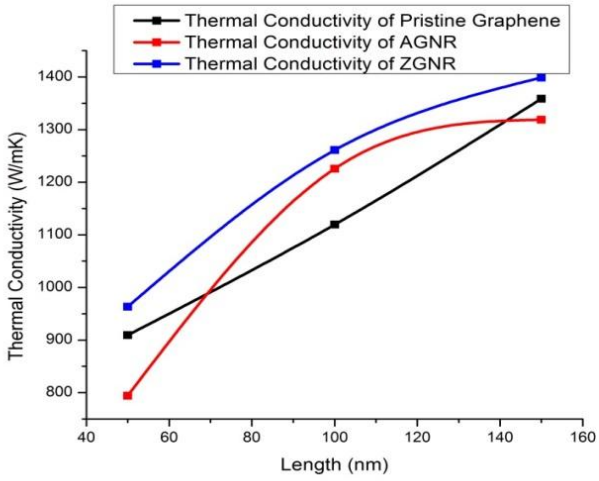

Figure 5.26 Simulated thermal conductivity of pristine graphene, armchair GNR, and zigzag GNR, as per our calculations.

The variations in widths of single layer graphene are known to have significant effect on their thermal conductivity values. Figure 5.27 (a) shows the width dependence of thermal conductivity as a function of number of layers of graphene [223].

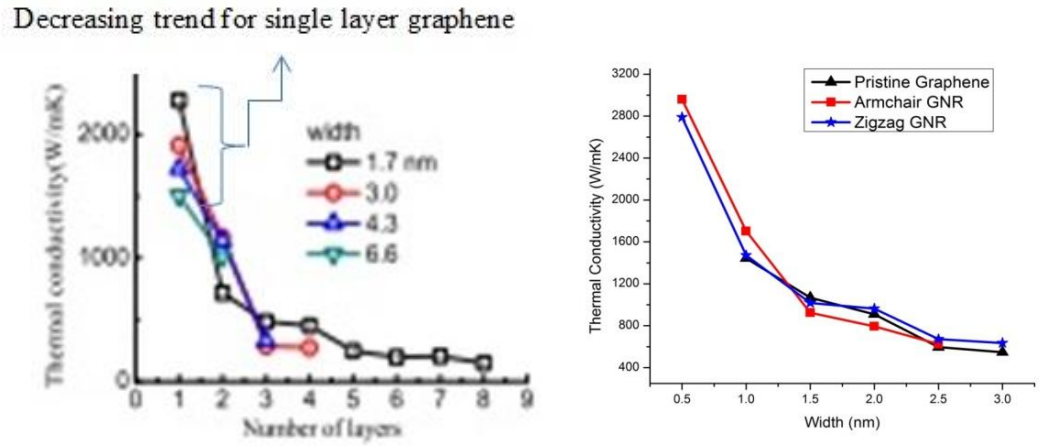

(a) (b)

Figure 5.27 (a) Layer-dependent simulated thermal conductivity for various widths of zigzag GNRs at 325 K, as per literature [223], (b) Effect of increasing width on thermal conductivity of pristine graphene and GNRs, as per our calculations.

It is observed that there is a decreasing trend of thermal conductivity with increase in width from 1.7 to 6.6 nm for single layer graphene. This is explained from the phenomena that, with increasing widths of GNRs, the total number of phonon modes increases, while the number of edge-localized phonon modes does not change.

Tersoff-Brenner potential has been used in these simulations for describing C-C bonding. Nosé–Hoover thermostat is used for controlling temperature during the simulations. Room temperature (RT) κ_p decreases montonically with number of layers in few layer graphene.

Figure 5.27 (b) shows our simulated results for width dependence of κ_p at room temperature. In our simulations, the length of graphene as well as GNRs is considered as

50 nm in all the cases with variations in width. The reason for decrease in κ_p with increase in width upto 3 nm is attributed to constant number of edge-localized phonon modes and increasing Umklapp scattering effects with higher widths.

Figure 5.28 (a) shows the trends for κ_p for higher widths of zigzag and armchair GNRs as per reference [224]. The increase in κ_p with increase of width is attributed to increase in number of phonon modes. However, κ_p gets saturated with increase of width beyond a certain limit as energy gap between different phonons reduces with increasing width. This leads to higher probability of Umklapp scattering.

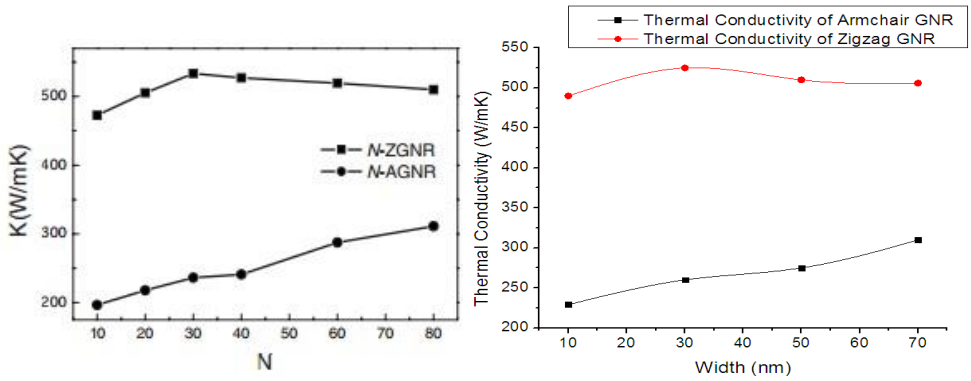

(a) (b)

Figure 5.28 (a) Simulated thermal conductivity of *N* -AGNR and *N* -ZGNR with variation of *N*, where the length of GNRs is fixed to be 11 nm. The ZGNR's thermal conductivity increases first and then decreases with *N* increasing, while, the AGNR's thermal conductivity monotonously increases with *N*, as per literature [224], (b) Simulated thermal conductivity of AGNR and ZGNR as a function of width, as per our calculations.

Figure 5.28 (b) shows our simulated results for thermal conductivity of armchair and zigzag GNRs with widths beyond 10 nm upto 60 nm. The simulation parameters have been kept constant for all the calculations. Length of graphene and GNRs is maintained as 50 nm and width is varied from 10-60 nm. It is observed that similar trends

occur with increase in width of graphene and GNRs. The reason for this behavior has been explained previously and is consistent with the findings in the literature.

Figure 5.29 (a) shows the simulated effect of nitrogen doping on armchair and zigzag GNRs as a function of concentration of nitrogen in the structure, as per reference [199] by Mortazavi et al. All the simulations of thermal conductivity have been performed using NEMD implemented in LAMMPS. Bonding interactions between C-C and C-N atoms have been modeled using optimized Tersoff potentials. The atoms at the corner of graphene structures are fixed during simulation. It is observed that doping of ~ 1% nitrogen in graphene results in considerable decrease in κ_p as well as reduction in chirality dependence of κ_p.

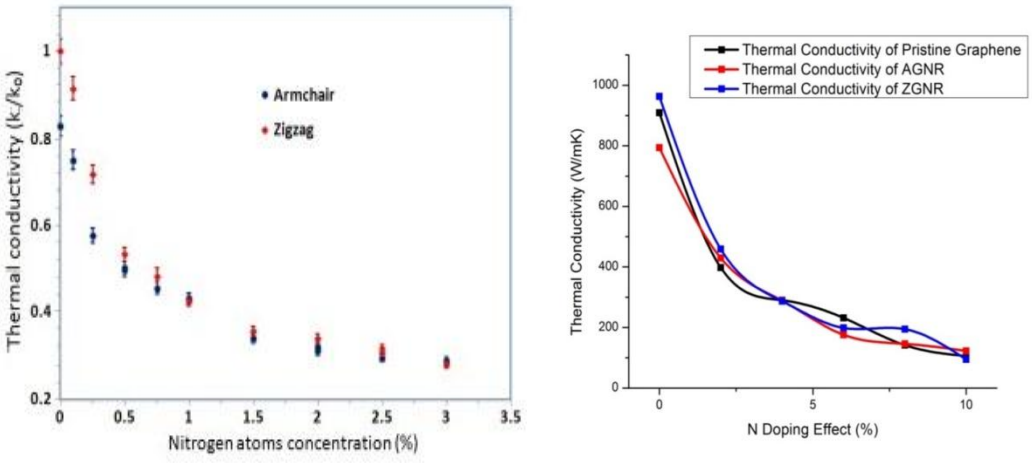

(a) (b)

Figure 5.29 (a) Simulated effect of nitrogen atom concentrations on the normalized thermal conductivity of single-layer graphene along the armchair and zigzag chirality directions, as per literature [224], (b) Simulated thermal conductivity of pristine single layer graphene and armchair/zigzag GNRs, as per our calculations.

Figure 5.29 (b) shows the trends for thermal conductivity as a function of % nitrogen for pristine graphene nanosheets as well as armchair and zigzag GNRs, as per our simulations. NEMD simulations have been performed in LAMMPS at room

temperature (300 K). Length and widths of all the graphene structures are maintained as 50 nm and 2 nm, respectively. Tersoff-Brenner potentials are used to describe C-C and C-N bonds and the cutoff in each case is 0.25 nm. Berendsen thermostat is used for maintaining constant temperature during the simulations. It is observed that there is a drastic reduction in thermal conductivity with about 2.5% nitrogen doping and the values have been found to be consistent with the literature. The reason for this reduction is reduction in lattice symmetry and broadening of peaks in DOS in the frequency range around 50 THz [199]. These phonon modes are considered to be dominant heat-carrying modes and contribute to heat transport in graphene.

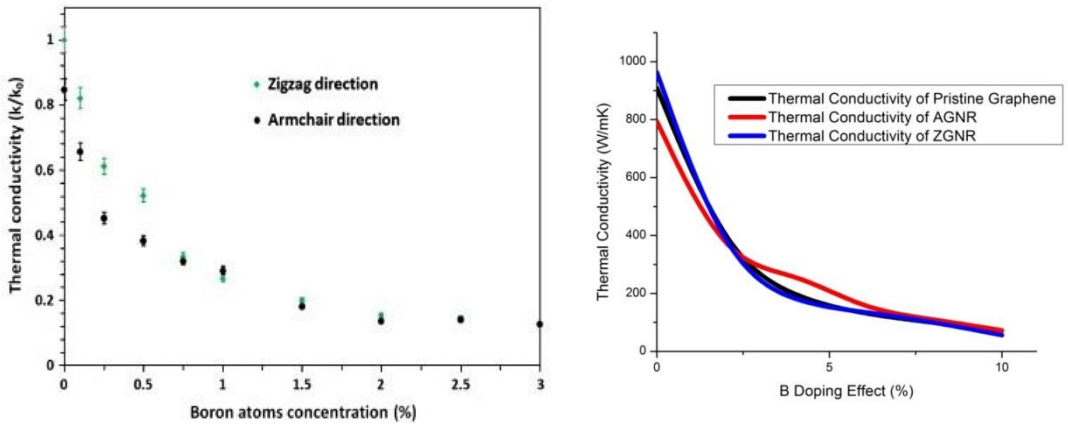

(a) (b)

Figure 5.30 (a) Simulated effect of boron atoms substitutions on the thermal conductivity of single-layer graphene along the armchair and zigzag chirality directions, as per literature [225], (b) Comparison of simulated thermal conductivity of pristine graphene and armchair/zigzag GNRs, as per our calculations.

Mortazavi et al. [225] have presented their studies of boron doping in armchair and zigzag GNRs by NEMD simulations implemented in LAMMPS. Interatomic interactions for C-C and C-B have been modeled using optimized Tersoff potential parameters. As shown in Figure 5.30 (a), it is observed that about 0.75% boron doping

results in a drastic reduction of thermal conductivity. The reasons for the reduction of thermal conductivity with increase in dopant concentration are similar to the ones in case of boron doping.

Figure 5.30 (b) shows our simulated results of thermal conductivity for pristine graphene nanosheets and armchair and zigzag GNRs as a function of % boron doping at room temperature, using NEMD simulations implemented in LAMMPS. It is observed that the trends are similar to the reported literature as in Figure 5.30 (a). The reduction in thermal conductivity of graphene structures is higher with boron doping. There is reduced chirality dependence of thermal conductivity with increase in % boron doping in graphene.

Figure 5.31 (a) shows the trends for thermal conductivity as a function of temperatures upto 700 K. The presented data is a collection of experimental results from various references presenting similar trends in the thermal conductivity calculations [144]. It is observed that increasing temperature shows lower values of thermal conductivity of graphene structures. The higher is the temperature; more are the collision of phonons. This leads to lower values of thermal conductivity with increasing temperature beyond 100 K. The increase of thermal conductivity with increase of temperatures upto 100 K is attributed to increase in mobility of phonons.

Figure 5.31 (b) shows the results of our simulations for thermal conductivity of pristine graphene nanosheets and nanoribbons, using NEMD simulations implemented in LAMMPS. In all the cases, the size of graphene structures is maintained as 50 nm X 2 nm (L X W). It is observed that similar reducing trends occur with increasing temperature

from 100-800 K, as shown in Figure 5.31 (b). Reason for reduction is attributed to higher Umklapp scattering as well as collision of phonons at high temperature.

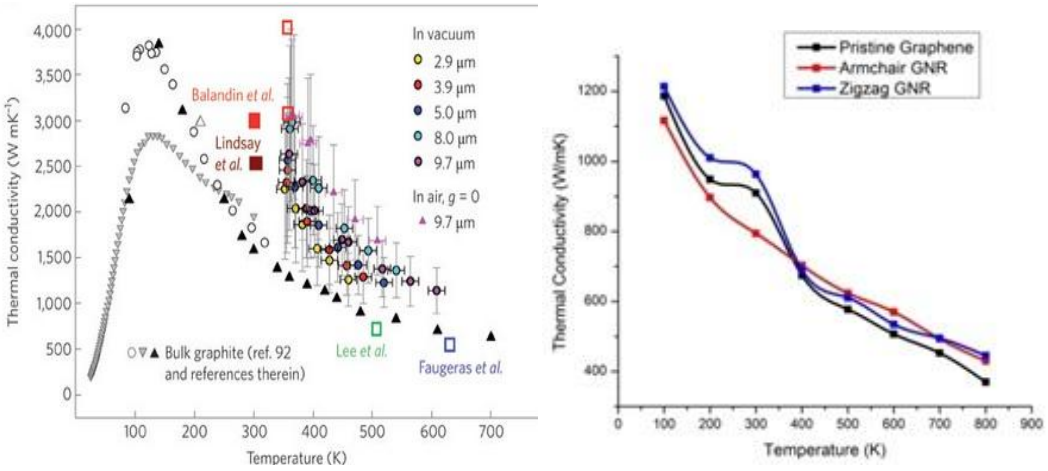

(a) (b)

Figure 5.31 (a) Experimental thermal conductivity of graphene as a function of temperature. Experimental data points are indicated by empty rectangular boxes. The filled red and brown boxes are theoretical data points. These two set of points are for different graphene flake sizes — 3 μm and 5 μm, respectively. Setting L = 3 μm would give K ≈ 2,500 W/mK. The experimental results from different research groups obtained for graphene by the Raman optothermal technique are in agreement within the experimental uncertainty of the method [144], (b) Simulated thermal conductivity as a function of temperature for pristine graphene and armchair/zigzag GNRs, as per our calculations.

Figure 5.32 (a) shows the reduction in simulated thermal conductivity of pristine graphene with varying concentration of vacancies, as per reference [201] by Zhang et al. In these simulations, REBO (Reactive Empirical Bond Order) potentials are used to model C-C interatomic interactions. Green Kubo method is employed in MD simulations. It is based on linear response theory. Green-Kubo method has been known to have an advantage of being devoid of artificial thermostat perturbation. The presence of thermostat could have influence on the thermal conductivity and heat flux. NVE ensemble (microcanonical) has been considered for isolated pristine graphene sheet at

room temperature (300 K). Zhang et al. have observed that even 0.42% vacancy concentration in graphene can cause significant reduction in thermal conductivity. While, at about 8.75% vacancy concentration, thermal conductivity can be reduced to ~ 3.08 ± 0.31 W/mK.

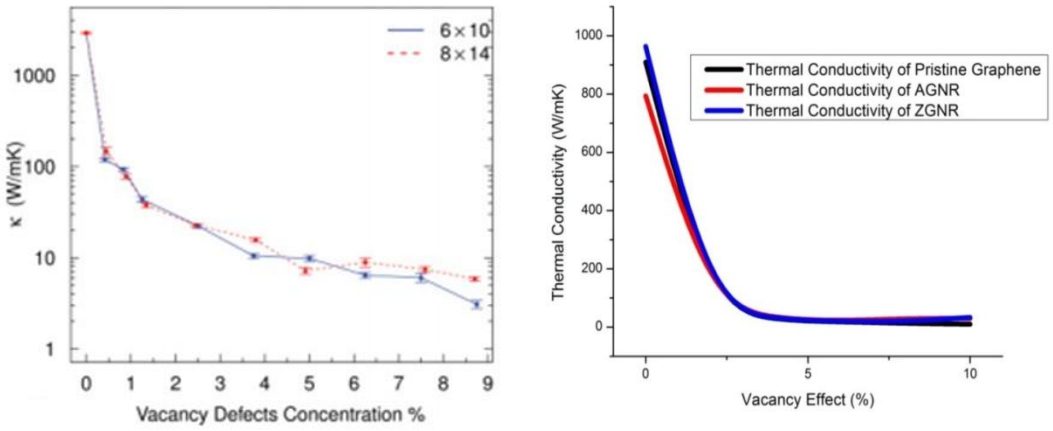

(a) (b)

Figure 5.32 (a) Simulated thermal conductivity of graphene as a function of vacancy defect concentration (at 300 K) using molecular dynamics simulations with the Green-Kubo method. The solid blue (dark gray) line and the dashed red (gray) line correspond to PB sizes of 6 × 10 and 8 × 14, respectively [201], (b) Simulated thermal conductivity of pristine graphene, armchair/zigzag GNR as a function of % vacancies at 300 K using molecular dynamics simulations with NEMD based Müller-Plathe technique, as per our calculations.

The reduction of thermal conductivity has been attributed to two important factors. First one is the broadening of phonon mode peaks around 15 THz, where the valley-shaped curves are almost flattened by broadening of nearby peaks with increasing concentration of vacancies. Broadening of phonon modes shows reduction of lifetime of those modes leading to lower mean free path. Thus, the thermal conductivity reduces. The second is an average increase of DOS for low frequency modes below 15 THz. This leads to reduction in relaxation time and corresponding mean free path which causes lower thermal conductivity values.

Figure 5.32 (b) shows our simulated thermal conductivity values of pristine graphene as well as armchair and zigzag GNRs with varying concentration of vacancies, using NEMD simulations implemented in LAMMPS. Initially, the system is relaxed and equilibration is maintained in the structure for about 50,000 timesteps with NPT ensemble. Timestep is considered to be 1 fs in the simulation. NEMD simulation is performed on NVE ensemble and Müller-Plathe technique is simulated, as explained in Chapter 3. Periodic boundary conditions are considered for each case and size of graphene is 50 nm X 2 nm. Similar trends have been observed and drastic reduction in thermal conductivity is found, which is consistent with the literature.

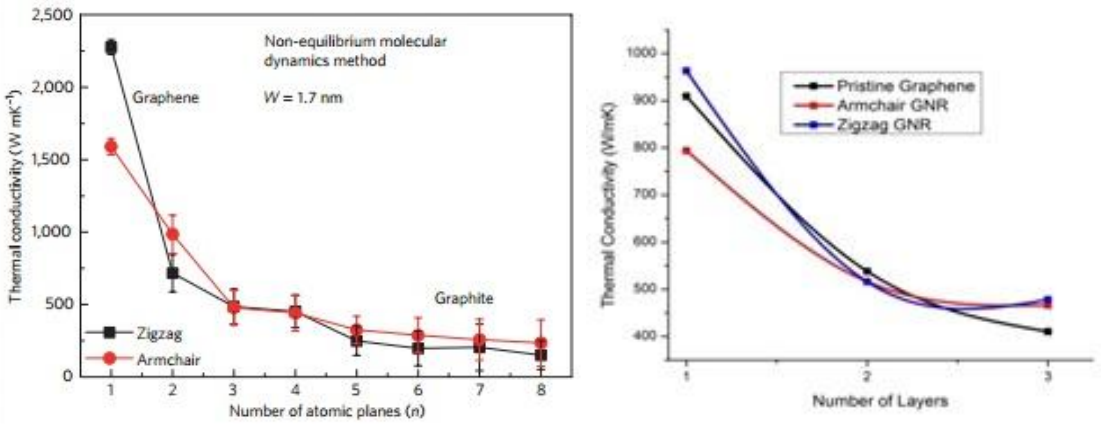

(a) (b)

Figure 5.33 (a) Simulated layer-dependent thermal conductivity of few-layer graphene. The 1-layer nanoribbons refer to graphene and the 5-8 layers nanoribbons are similar to ultra-thin graphite, as per literature [223], (b) Simulated layer-dependent thermal conductivity of pristine graphene and armchair/zigzag GNRs 1-3 layers, as per our simulations.

Figure 5.33 (a) shows the trends of simulated thermal conductivity of graphene as well as armchair and zigzag GNRs, as per reference [223] by Zhong et al. It is observed that there is decrease in thermal conductivity in each case due to cross-plane coupling of low energy phonons. The cross-plane coupling is absent in the case of single layer

graphene. Hence, the mode of thermal transport in single layer graphene is ballistic. In the presence of cross-plane coupling, particles at the interface between the layers are subject to collision leading to phonon scattering. This leads to lower values of thermal conductivity for few layer graphene (FLG).

Figure 5.33 (b) shows our results for NEMD simulation of pristine graphene as well as armchair and zigzag GNRs, as a function of number of layers from 1 to 3 at room temperature. Modeling parameters have been considered to be same as previous cases. Size of graphene in each case is 50 nm X 2 nm. Similar trends are observed as the ones reported in literature. An important observation is reduced chirality dependence of κ_p of GNRs with increasing number of layers.

5.6 Thermoelectric Properties

Shrinking size of electronic devices through integration has led to an acute need for thermal management in graphene systems, which are potential replacement for Si in optoelectronic devices. Application of thermoelectric effect in graphene systems is described in detail in Chapter 2. In this section, comparison to literature for calculation of Seebeck coefficient (S), electronic thermal conductivity (κ_e), and electrical conductivity (σ) is presented for pristine and doped armchair GNRs as a function of chemical potential, temperature and concentration of dopants. Increase in thermoelectric performance of zigzag GNRs with induced vacancies is compared with the literature and variations in models are explained in each case.

ZT (Figure-of-Merit) is the factor to be considered for gauging the performance of a material for thermoelectric applications. The details of calculations of ZT have been presented in Chapter 4. Electronic band structure calculations are performed with

Quantum Espresso. These results are used by a post-processing tool "Boltztrap" (Boltzmann Transport Properties) for calculating the semi-classical transport coefficients in each case. It is essential to include a large mesh of k-points in the Irreducible Brillouin Zone (IBZ) for achieving better accuracy of the thermoelectric parameter results. We have performed non-Self Consistent calculations with dense k-mesh considering atleast 200 k-points in IBZ in each case. Hence, the results in our simulation are found to have consistency in results with respect to published literature.

5.6.1 Seebeck Coefficient and Hall Resistivity as a Function of Chemical Potential

Wei et al. [146] have presented experimentally that thermoelectric transport is sensitive to the bandstructure. Away from the Dirac point, the magnitude of the thermovoltage reduces. Wei et al. have reported measurement of S_{xx} on a device, with V_D ~ 33 V, having electron-hole asymmetry. On the hole side, S_{xx} decreases with reduction in gate voltage V_g, while, on the electron side, S_{xx} remains flat. Seebeck coefficient is found to increase with increase in temperature, as shown in Figure 5.34 (a).

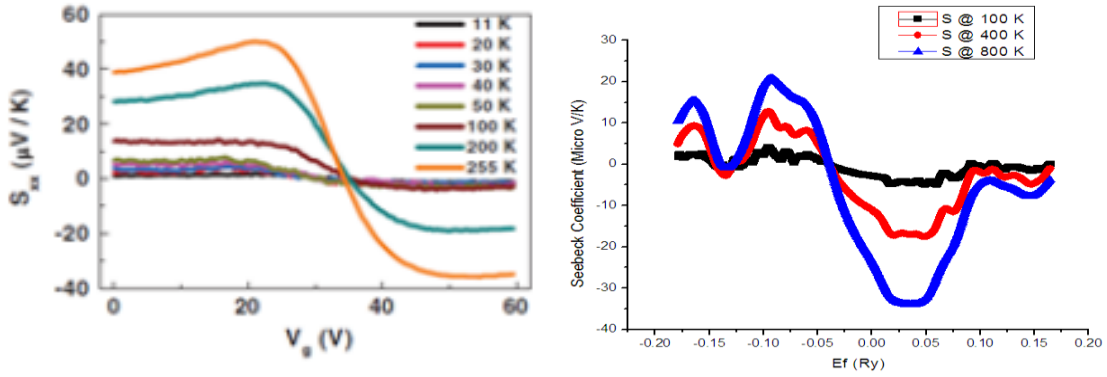

(a) (b)

Figure 5.34 (a) Experimentally measured plot of gate voltage (V_g) dependence of longitudinal Seebeck coefficient S_{xx} at different temperatures (11–255 K) and zero magnetic field, as per literature [149] , (b) Simulated Seebeck coefficient as a function of chemical potential for 100 K, 400 K and 800 K, as per our calculations.

Wei et al. have reported the reason for deviation from linear temperature dependence on electron side to the asymmetric nature of band of impurity states. Impurity states in impurity scattering model are reported to be highly asymmetric near the Dirac point. This anomalous nature of thermoelectric transport in graphene can lead to its potential application as a sensitive probe for impurity bands near the Dirac point.

Figure 5.34 (b) shows our results of the simulated Seebeck coefficient as a function of chemical potential, at 100 K, 400 K, and 800 K. We note the similar behavior of Seebeck coefficient as a function of chemical potential. It is observed that Seebeck coefficient increases with increase in temperature. Electronic bandstructure calculations have been performed in accordance with the method explained in Section 4.1 for graphene with a width of 2 nm and periodic boundary conditions. Monkhorst k-point mesh of 13 X 13 X 1 is found to have least energy of the system and number of k-points in the IBZ is > 200 in each case.

Checkelsky and Ong [147] have reported experimental measurements of TEP, S, and Nernst, S_{yx}, signals in graphene in magnetic fields as well as non-zero magnetic fields. In the absence of magnetic fields, it has been reported that there is a change in sign of S with gate voltage V_G. Also, it is noted that there is a nominally linear temperature dependence of peak value, S_m, from ~ 20 K to 300 K, as shown in Figure 5.35 (a).

Figure 5.35 (b) shows our simulated results for maximum Seebeck coefficient for zigzag GNRs as a function of temperature. It is observed that there is almost linear temperature dependence of Seebeck coefficient. Thus, independent of chirality, there is a linear temperature dependence of Seebeck coefficient upto 800 K.

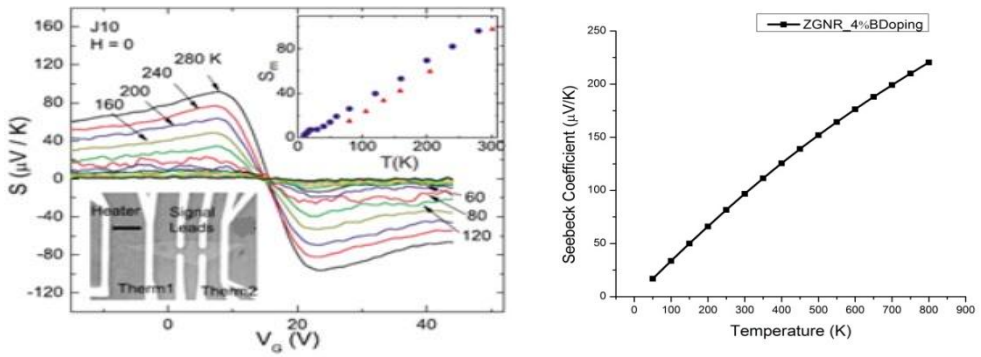

(a) (b)

Figure 5.35 (a) Experimentally obtained curves of TEP, $S=-S_{xx}$ vs V_g in sample J10 (left inset) in zero magnetic field at selected T. The curves are anti-symmetric about the Dirac point which occurs at the offset voltage V_0=15.5 V. The peak value S_m (right inset) is nominally linear in T from 25 to 300 K, as per literature [149], (b) Simulated Seebeck coefficient as a function of temperature, as per our calculations.

As shown in Figure 5.36, it is observed that, in case of doped armchair GNRs, there is an increase of Seebeck coefficient with increase in the concentration of dopant - boron in this case, with the concentration varying from 0 to 12%. The maximum Seebeck coefficient is observed to be ~ 650 μV/K at room temperature (300 K). This is an increase of about 3 times over pristine armchair GNR, with the same set of conditions.

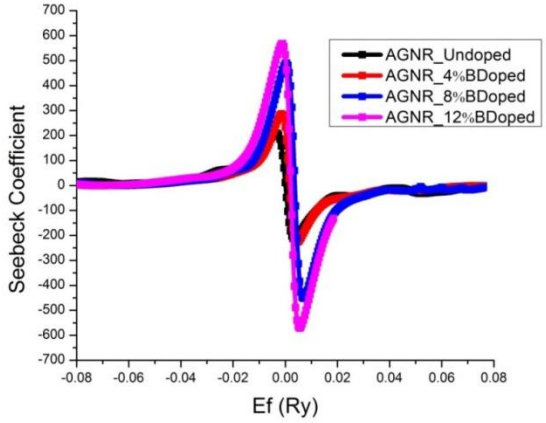

Figure 5.36 Simulated Seebeck coefficient as a function of chemical potential for pristine armchair GNR as well as 4%, 8% and 12% boron doped AGNRs, as per our calculations.

Figure 5.37 shows the trends for Hall resistivity as a function of chemical potential for armchair GNR, as per our simulations. It is observed that there is an increase in the Hall resistivity for increasing boron concentration. These trends are found to be similar to the Seebeck coefficient, as shown in Figure 5.36.

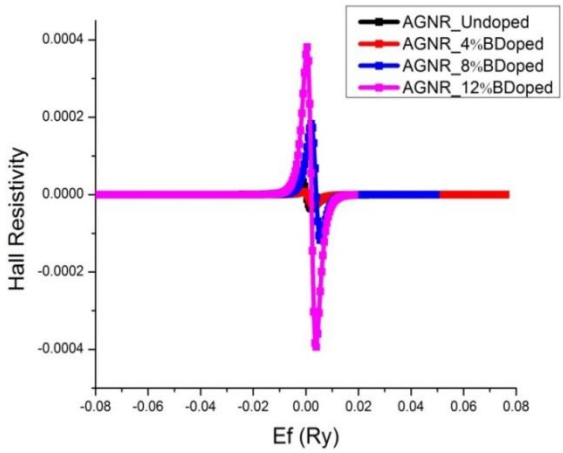

Figure 5.37 Simulated Hall resisitivity (m^3/C) as a function of chemical potential of armchair GNR as well as 4%, 8% and 12% boron doped AGNR, as per our calculations.

5.6.2 Electrical Conductivity and Electronic Thermal Conductivity as a function of Chemical Potential

Figure 5.38 (a) shows the gate voltage dependence of electrical conductivity, σ, of a device A at 150 K for single layer graphene at three different mobilities of electrons in zero and non-zero magnetic fields. In the absence of magnetic field, with increase in mobility, the maximum value of S_{xx} increases, and exhibits an increasingly diverging trend accompanied by a sharper peak- to-dip transition around Dirac point. It is reported that the peak-to-dip width has relation with the width of minimum conductivity plateau. It is broader for low mobility state and is associated with the disorder in graphene. S_{xx} is found to converge to the same value at high gate voltages on either side of charge neutrality point, for all mobility values. Thus, it is noted that, near the Dirac point, the

effective carrier density is much higher than charge density fluctuations induced by the charged impurities.

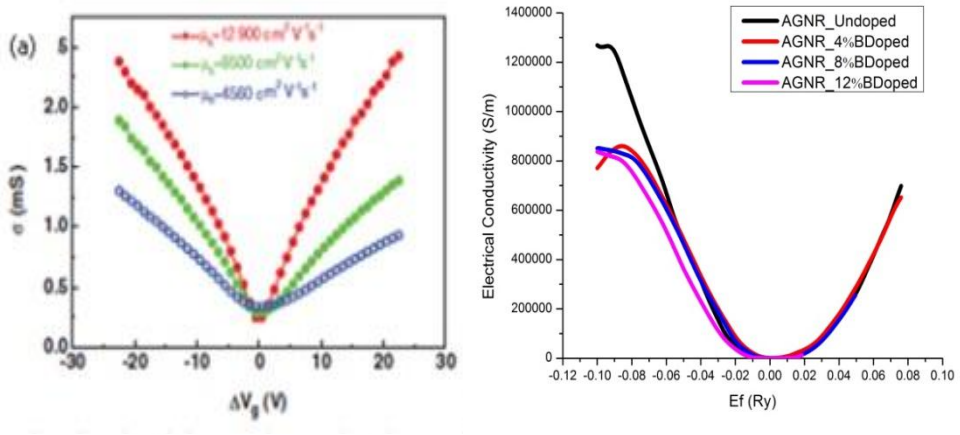

(a) (b)

Figure 5.38 (a) Experimental gate voltage dependence of electrical conductivity, σ, of a device A at 150 K with three hole mobility values 12900, 8500 and 4560 $cm^2V^{-1}s^{-1}$, as per literature [149], (b) Simulated electrical conductivity as a function of chemical potential for armchair GNR and 4%, 8% and 12% boron doped armchair GNRs, as per our calculations.

Figure 5.38 (b) shows our simulation of the electrical conductivity of armchair GNRs doped with 4%, 8% and 12% boron, as a function of chemical potential. It is seen that there is a reduction in the peak electrical conductivity of armchair GNR with increasing concentration of dopants in GNR. This is as a result of reduced electron mobilities in armchair GNRs with increasing doping. Thus, similar trends can be observed in our simulated electrical conductivity of GNRs with the ones in the literature.

Figure 5.39 (a) shows the trends for electronic thermal conductivity of armchair GNRs with varying widths as a function of chemical potential, as per reference [226]. The variations in the trends are attributed to varying band gaps with variations of widths of GNRs.

Figure 5.39 (b) shows our simulated result for the electronic thermal conductivity for armchair GNR as a function of chemical potential. It is observed that the trends for these cases are similar to the ones in the literature. We have considered the doping of armchair GNR, which leads to variation of the band gap. Also, one can observe the reduction in the peak electronic thermal conductivity for GNR with increasing nitrogen doping concentration.

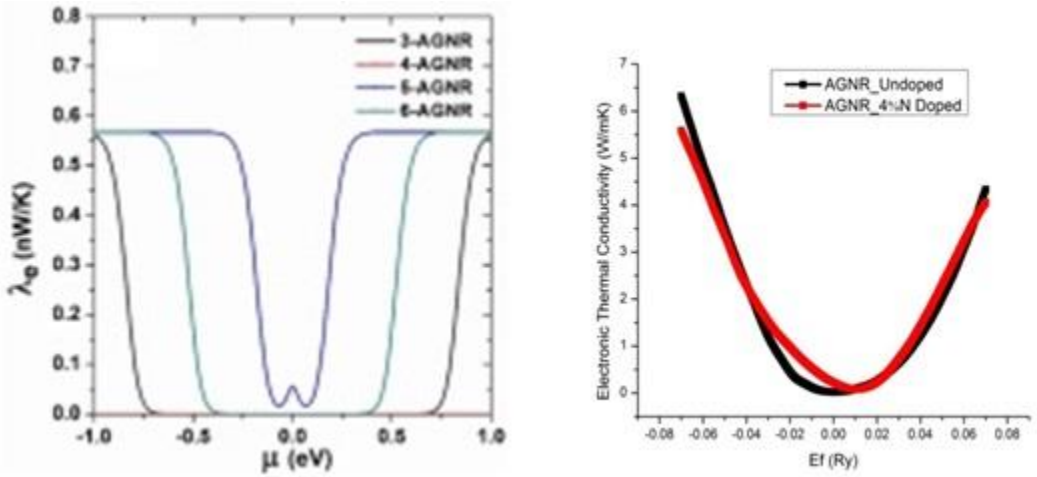

(a) (b)

Figure 5.39 (a) Simulated electronic thermal conductance as a function of chemical potential for a series of armchair GNRs, as per literature [226], (b) Simulated electronic thermal conductivity as a function of chemical potential for armchair GNRs with 0% and 4% nitrogen doping, as per our calculations.

5.6.3 Transport Parameters of Zigzag GNRs with Vacancies

An efficient thermoelectric material must be efficient in effectively separating hot and cold carriers. The quantity determining the ability to filter carriers is the Seebeck coefficient which depends on the asymmetry of the density of states around the Fermi level. In semiconductors, the Seebeck coefficient is large, whereas, in a metal, the DOS is more uniform in energy and the Seebeck coefficient is small. Metallic ZGNRs also have

a small Seebeck coefficient because their transmission is constant around the Fermi level, despite the peak in the DOS at E = 0 eV due to the edge states.

However, it has been reported by Bahamon et al. [208] that, with creation of extended line defects in zigzag GNRs, the electron-hole symmetry breaks and there are additional electron bands around the Fermi level. In this way, asymmetry in DOS and transmission function are attained which results in improvement of the Seeback coefficient. This particular structure has also been reportedly realized experimentally by Jayeeta et al. [227].

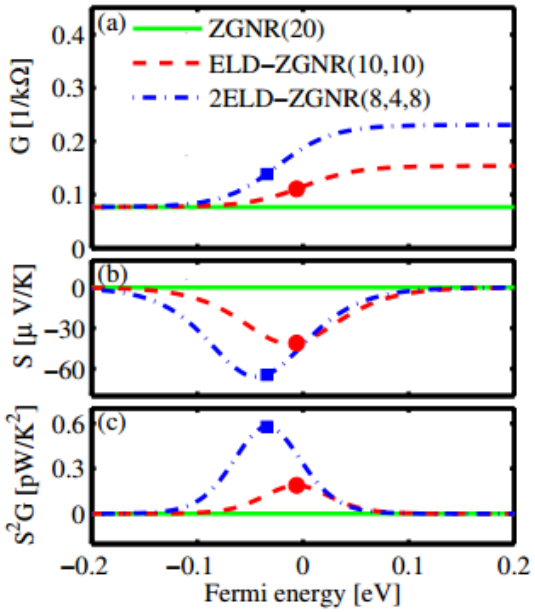

Figure 5.40 (a) Electrical conductance, (b) Seebeck coefficient, and (c) thermoelectric power factor of pristine ZGNR(20), ELD-ZGNR(10,10), and 2ELD-ZGNR(8,4,8) channels with perfect edges . The dots indicate the Fermi energy values at which the peak of the power factor occurs for the ELD and 2ELD channels, as per literature [206].

Figure 5.40 (a) shows the trends for electrical conductance, Seebeck coefficient and power factor of pristine ZGNR, as well as with induced extended line defects (ELDs), by Karamitaheri et al. [206]. It shows the conductance of 2ELD-ZGNR (dashed-

dot-blue), the ELD-ZGNR (dashed-red), and the pristine nanoribbon (green) at room temperature, 300 K. It is observed that the conductance of the channel with two ELDs is the largest, followed by the channel with one ELD. The values of conductance are larger than the pristine channel by ~3 *X* and ~2 *X*, respectively.

Figure 5.40 (b) shows the variations of the Seebeck coefficient after the introduction of the ELDs in the ZGNRs. The pristine channel exhibits zero Seebeck coefficient as it is metallic and it has flat transmission near the Fermi level. Due to the built asymmetry after the introduction of the ELDs, however, the Seebeck coefficient has been found to increase for both the channels. The channel containing two line defects has the largest asymmetry. Therefore, ZGNR with two line defects has the largest Seebeck coefficient (in absolute values).

The power factor trends have been shown in Figure 5.40 (c). It is found to be highly improved in the ELD structures and especially the 2ELD-ZGNR channel.

Figure 5.41 (a) and (b) show our simulated results for electrical conductivity and Seebeck coefficient, respectively. Initially, vacancies are randomly induced in pristine zigzag GNR structure followed by relaxation till the energy is minimized to 1.0E-8 eV. This is followed by non-Self Consistent simulation using Quantum Espresso considering Monkhorst k-point mesh as 20 X 20 X 1, in order to ensure that there are > 200 k-points in the irreducible Brillouin Zone (IBZ). It is observed that, the trends for electrical conductivity are found to be matching with the literature.

However, it is observed that there is a higher degree of asymmetry in the Seebeck coefficient curve in our simulation, as compared with the literature Figure 5.40 (b). This is attributed to the fact that we have considered creation of vacancies randomly in the

zigzag GNR lattice. However, even in this case, there is a significant improvement in the Seebeck coefficient values of zigzag GNRs compared with the pristine zigzag GNRs without vacancies.

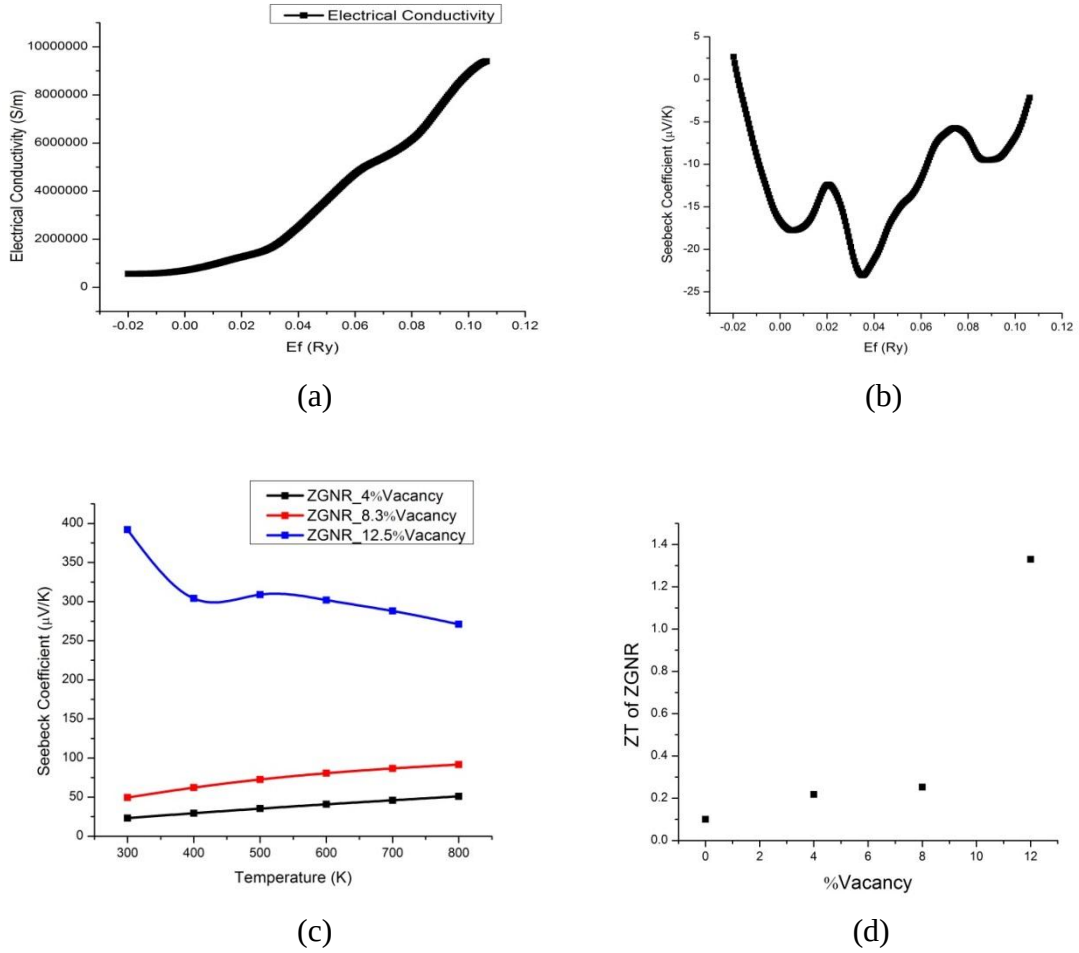

Figure 5.41 (a) Simulated electrical conductivity as a function of chemical potential for zigzag GNR with 4% vacancy, (b) Simulated Seebeck coefficient as a function of chemical potential for zigzag GNR with 4% vacancy, (c) Simulated Seebeck coefficient as a function of temperature for zigzag GNR with 4%, 8.3% and 12.5% vacancies, (d) Figure-of-Merit (ZT) as a function of % vacancy for zigzag GNR with 4%, 8.3% and 12.5% vacancies, as per our calculations.

Figure 5.41 (c) shows the trends for Seebeck coefficient for zigzag GNRs with 0%, 4%, 8.3% and 12.5% in the temperature range of 300 – 800 K. It is observed that, for

the case of 12.5% vacancies, there is a sudden increase in the Seebeck coefficient values compared with 4% and 8.3%. This shows that one can achieve higher thermopower with higher vacancy concentration in zigzag GNRs. Also, it is found that Seebeck coefficient increases slightly for the case of 4% and 8.3% vacancies in zigzag GNRs. However, in the case of 12.5% vacancies, there is a slight reduction in the Seebeck coefficient at higher temperatures. Thus, with higher values of S and electrical conductivity, one can obtain higher power factor in this case. With the evaluation of transport parameters, we calculated ZT for zigzag GNRs as a function of % vacancy. It is observed that the value of ZT increases slowly upto 8.3% vacancy in zigzag GNRs. As expected, ZT value is found to be highest for 12.5% vacancy case. This is attributed to higher Seebeck coefficient, electrical conductivity and lower thermal conductivity in the presence of vacancies as compared with pristine zigzag GNRs. Thus, it can be concluded that one can achieve higher ZT by effectively creating vacancies and attain better thermoelectric performance with application of such a structure in optoelectronic devices.

CHAPTER 6

CONCLUSIONS

Graphene is found to be an excellent material for applications in optoelectronic in view of its extraordinary electronic, optical, mechanical and thermoelectric properties.

Graphene is shown to be a zero bandgap material. Modification of electronic band structure of graphene has been shown to be possible by means of chemical doping. Boron and nitrogen have been shown to be effective p- and n- type dopants, respectively, in graphene. The bandstructure analysis shows that n- and p- type of dopants shift the Dirac point of graphene on the negative or positive side of energy, respectively. The armchair graphene nanoribbons are shown to have negligible band gaps depending on their size while, zigzag graphene nanoribbons are known to exhibit metallic nature. The metallic character of zigzag nanoribbons is attributed to the high density of edge states at the Fermi energy. The chirality dependence of electronic properties of graphene, leading to its metallic or semiconducting properties for zigzag and armchair nanoribbons, could present a possibility of full carbon based electronic devices, where semiconducting tubes could be used as channels and metallic ones as interconnects. However, the lack of control on chirality is found to be a challenging aspect in engineering their electronic properties and industrial applications. Introducing impurities and functional groups has been shown to be effective way for controlling the properties of graphene nanoribbons.

Graphene is shown to be optically transparent in the visible range. Both the real and imaginary parts of dielectric constants of graphene are found to be varying with the number of layers. It is noted that there is an increase in the peak intensity of the dielectric functions with increase in number of layers of graphene. Variations in the static dielectric

constant are found to be dependent on the concentration of p- or n- type dopants in graphene and GNRs.

A comparison of the wavelength and thickness dependent optical properties, mainly emissivity and transmittance has been presented for various multilayered configurations with graphene as one of the component layers. Such structures have been found to be useful as hot electron bolometers. Graphite is found to have emissivity that is independent of thickness. Emissivity of graphene remains low and increases with increase in number of layers. For BN based hot-electron bolometer, the emissivity is found to increase with increase in BN layer thickness. The effect of graphene is to increase the emissivity of the bolometer structure. A comparison of the emissivity of graphite and graphene show that graphite exhibits higher emissivity.

Graphene has been reported to have an extremely high elastic modulus of the order of 1 TPa. The values of elastic modulus are found to be varying slightly depending on the indenter diameter i.e., the Young's modulus increases with increase in diameter. The values of indentation force depend on the type of interatomic potential considered in the simulation. Airebo potential has values of indentation force ~ 1.5 times higher than the Tersoff potential, for the same indentation depth. The higher is the indentation velocity, the greater is the indentation force recorded at the same indentation depth. Bilayer graphene is found to provide higher resistance to the indentation. Hence, bilayer graphene has higher values of indentation force at the same values of indentation depth. Load versus indentation depth curves are found to be useful tools in the evaluation of mechanical properties. Atomistic simulations are successful in predicting the mechanical properties which are comparable to the experimental findings.

Single layer graphene and GNRs are found to exhibit increase in the phonon-induced lattice thermal conductivity (κ_p) with increase in length, while κ_p is found to increase with decrease in width. Sudden drop in κ_p is observed with increase in width from 0.5 nm to 1.5 nm. κ_p is noted to remain constant for higher widths in case of AGNRs. In case of ZGNRs, κ_p increases upto about 30 nm but decreases further. Transport is found to become more ballistic with increasing widths of GNRs. Thus, the role of edges reduces with increasing width. κ_p is found to reduce drastically ~50% with doping of B or N. Increasing dopant concentration also marks reducing chirality dependence of thermal conductivity values. Boron doping leads to higher reduction in κ_p as compared to nitrogen doping. Higher temperatures cause reduction in κ_p for temperatures in the range of 100 to 800K. At about 400K, all the graphene nanostructures i.e., pristine graphene and GNRs are found to have similar values of κ_p. The presence of vacancies, to the extent of ~4%, causes about ~70% reduction in thermal conductivity with increasing number of layers of graphene and GNRs indicating interlayer interactions. Room temperature κ_p of ZGNR is found to be higher than AGNR, while AGNR is reported to have higher κ_p at higher temperatures. Electronic thermal conductivity (κ_e) is found to increase with temperature. The rate of increase of κ_e is faster in bilayer graphene as compared to single layer graphene. High thermal conductivity of graphene leads to its potential application as ballistic field effect transistors (FETs).

Graphene is found to have extremely high electrical conductivities ~ 10^6 to 10^8 S/m depending on the potentials applied and temperature. Electrical conductivity of GNRs is also a function of its chirality i.e., armchair and zigzag. Peak electrical conductivity of graphene and GNRs decreases with increasing concentration of doping.

This is attributed to the corresponding changes in the electronic band structures upon doping. Seebeck coefficients are found to be symmetrical around the charge neutrality point. Peak Seebeck coefficients are found to reduce with increase in temperatures, mostly linearly at higher temperatures. For a given chemical potential, away from the Fermi energy, it is found that Seebeck coefficients increase linearly with temperature. This shows the diffusive thermoelectric generation mechanism in the absence of phonon drag components. Band gaps reduce with increasing widths for AGNRs and hence Seebeck coefficients reduce. Similar effects have been observed in case of ZGNRs. Seebeck coefficients (TEP) are observed to be higher for AGNRs with respect to ZGNRs. TEP for AGNRs are symmetrical about the charge neutrality point (CNP) with the change in majority charge carriers from electrons to holes. Seebeck coefficient is found to increase with increase in concentration of B or N dopants. Peak values of TEP for AGNR are observed at 12% p-doping while, for ZGNR, it is observed at about 4% doping of p-type and at 8% n-type doping. Hall resistivity is observed to follow similar trends as the Seebeck coefficient for graphene on a given substrate.

Power factor is found to increase with temperature in the range of 100-500 K. $\sigma_{graphene}$ is highest at +/- k_BT, while it reduces to nil at Fermi level.

The Figure-of-Merit (ZT) is found to increase with decreasing length of graphene in the range of 200 nm to 25 nm with constant width of 2 nm. The highest values observed are ~ 1.4 for graphene at about 25 nm length. The reason for this improvement is the decrease in lattice induced thermal conductivity for lower lengths of graphene. Effect of doping p- or n-type dopants in AGNR and ZGNR is to improve ZT values. It is found that ZT increases at a higher rate in AGNR than ZGNR with increasing

concentration of dopants. The values of ZT are found to be higher for AGNR than ZGNR. Thus, AGNR is more suitable for thermoelectric device applications. The ZT values for modified geometries or doped graphene nanostructures are noted to be higher than conventional thermoelectrics such as Bi_2Te_3. The thermopower is found to improve with increase in concentration of vacancies in ZGNRs. This improvement is attributed to breaking of electron-hole energy symmetry with induced defects. Asymmetry in DOS leads to increased thermopower. This also leads to improved Figure-of-Merit (ZT) in ZGNR with respect to the corresponding pristine ZGNR (without vacancies). The reason for this improvement is attributed to reduced thermal conductivities and a minimal reduction in power factor.

REFERENCES

1. A. K. Geim and K. S. Novoselov, *The rise of graphene, Nat Mater,*6 (3) (2007), pp. 183-191.

2. C. Talbot, *Fullerene and nanotube chemistry: an update, School science review,*81 (1999), pp. 37-48.

3. P. R. Birkett, A. G. Avent, A. D. Darwish, H. W. Kroto, R. Taylor and D. R. Walton, *Holey fullerenes! a bis-lactone derivative of fullerene with an eleven-atom orifice, J. Chem. Soc., Chem. Commun.,*(18) (1995), pp. 1869-1870.

4. M. S. Dresselhaus, G. Dresselhaus and P. C. Eklund, In *Science of Fullerenes and Carbon Nanotubes*, ed. M. S. Eklund, Dresselhaus G. and Dresselhaus P. C. (Academic Press: San Diego, 1996), pp. 15-59.

5. K. S. Novoselov, A. K. Geim, S. V. Morozov, D. Jiang, Y. Zhang, S. V. Dubonos, I. V. Grigorieva and A. A. Firsov, *Electric Field Effect in Atomically Thin Carbon Films*, *Science,*306 (5696) (2004), pp. 666-669.

6. A. K. Geim and K. S. Novoselov, *The rise of graphene, Nature Materials,*6 (3) (2007), pp. 183-191.

7. H. Luo, G. Xiong, Z. Yang, S. R. Raman, Q. Li, C. Ma, D. Li, Z. Wang and Y. Wan, *Preparation of three-dimensional braided carbon fiber-reinforced PEEK composites for potential load-bearing bone fixations. Part I. Mechanical properties and cytocompatibility*, *Journal of the Mechanical Behavior of Biomedical Materials,*29 (2014), pp. 103-113.

8. D. D. L. Chung, *Thermal analysis of carbon fiber polymer-matrix composites by electrical resistance measurement*, *Thermochimica Acta,*364 (1–2) (2000), pp. 121-132.

9. B. Yakobson and P. Avouris, In *Carbon Nanotubes*, ed. M. Dresselhaus, Dresselhaus G. and Avouris P. (Springer Berlin Heidelberg: 2001), pp. 287-327.

10. A. R. Ranjbartoreh, B. Wang, X. Shen and G. Wang, *Advanced mechanical properties of graphene paper*, *Journal of Applied Physics,*109 (1) (2011), p. 014306 (6 pages).

11. P. R. Wallace, *The Band Theory of Graphite*, *Physical Review,*71 (9) (1947), pp. 622-634.

12. K. S. Novoselov, D. Jiang, F. Schedin, T. J. Booth, V. V. Khotkevich, S. V. Morozov and A. K. Geim, *Two-dimensional atomic crystals*, *Proceedings of the National Academy of Sciences of the United States of America,*102 (30) (2005), pp. 10451-10453.

13. G. Ed, *Nobel Prize 2010: Andre Geim & Konstantin Novoselov*, *Nat Phys*,6 (11) (2010), pp. 836-836.

14. L. D. Landau, *Zur Theorie der phasenumwandlungen II*, *Phys. Z. Sowjetunion*,11 (1937), pp. 26-35.

15. R. W. Cahn and B. Harris, *Newer Forms of Carbon and their Uses*, *Nature*,221 (5176) (1969), pp. 132-141.

16. "Intriguing state of matter previously predicted in graphene-like materials might not exist after all" (2013), http://phys.org/news/2013-05-intriguing-state-previously-graphene-like-materials.html (Accessed 11/13/2014).

17. B. Partoens and F. M. Peeters, *From graphene to graphite: Electronic structure around the K point*, *Physical Review B*,74 (7) (2006), p. 075404.

18. R. R. Nair, P. Blake, A. N. Grigorenko, K. S. Novoselov, T. J. Booth, T. Stauber, N. M. R. Peres and A. K. Geim, *Fine Structure Constant Defines Visual Transparency of Graphene*, *Science*,320 (5881) (2008), pp. 1308-1308.

19. S. V. Muley and N. M. Ravindra, In *Nanotechnology for Water Treatment and Purification*, ed. A. Hu and Apblett A. (Springer International Publishing: 2014), pp. 159-224.

20. P. T. Yin, T.-H. Kim, J.-W. Choi and K.-B. Lee, *Prospects for graphene-nanoparticle-based hybrid sensors*, *Physical Chemistry Chemical Physics*,15 (31) (2013), pp. 12785-12799.

21. J. T.-W. Wang, J. M. Ball, E. M. Barea, A. Abate, J. A. Alexander-Webber, J. Huang, M. Saliba, I. Mora-Sero, J. Bisquert, H. J. Snaith and R. J. Nicholas, *Low-Temperature Processed Electron Collection Layers of Graphene/TiO2 Nanocomposites in Thin Film Perovskite Solar Cells*, *Nano Letters*,14 (2) (2013), pp. 724-730.

22. M. F. El-Kady, V. Strong, S. Dubin and R. B. Kaner, *Laser Scribing of High-Performance and Flexible Graphene-Based Electrochemical Capacitors*, *Science*,335 (6074) (2012), pp. 1326-1330.

23. S. Stankovich, D. A. Dikin, G. H. B. Dommett, K. M. Kohlhaas, E. J. Zimney, E. A. Stach, R. D. Piner, S. T. Nguyen and R. S. Ruoff, *Graphene-based composite materials*, *Nature*,442 (7100) (2006), pp. 282-286.

24. K. S. Kim, Y. Zhao, H. Jang, S. Y. Lee, J. M. Kim, K. S. Kim, J.-H. Ahn, P. Kim, J.-Y. Choi and B. H. Hong, *Large-scale pattern growth of graphene films for stretchable transparent electrodes*, *Nature*,457 (7230) (2009), pp. 706-710.

25. Q. Liu, Z. Liu, X. Zhang, L. Yang, N. Zhang, G. Pan, S. Yin, Y. Chen and J. Wei, *Polymer Photovoltaic Cells Based on Solution-Processable Graphene and P3HT*, *Advanced Functional Materials*,19 (6) (2009), pp. 894-904.

26. S. Bae, H. Kim, Y. Lee, X. Xu, J.-S. Park, Y. Zheng, J. Balakrishnan, T. Lei, H. Ri Kim, Y. I. Song, Y.-J. Kim, K. S. Kim, B. Ozyilmaz, J.-H. Ahn, B. H. Hong and S. Iijima, *Roll-to-roll production of 30-inch graphene films for transparent electrodes*, *Nat Nano*,5 (8) (2010), pp. 574-578.

27. A. Tzalenchuk, S. Lara-Avila, A. Kalaboukhov, S. Paolillo, M. Syvajarvi, R. Yakimova, O. Kazakova, T. J. B. M. Janssen, V. Fal'ko and S. Kubatkin, *Towards a quantum resistance standard based on epitaxial graphene*, *Nat Nano*,5 (3) (2010), pp. 186-189.

28. X. Li, W. Cai, J. An, S. Kim, J. Nah, D. Yang, R. Piner, A. Velamakanni, I. Jung, E. Tutuc, S. K. Banerjee, L. Colombo and R. S. Ruoff, *Large-Area Synthesis of High-Quality and Uniform Graphene Films on Copper Foils*, *Science*,324 (5932) (2009), pp. 1312-1314.

29. M. I. Katsnelson and K. S. Novoselov, *Graphene: New bridge between condensed matter physics and quantum electrodynamics*, *Solid State Communications*,143 (1–2) (2007), pp. 3-13.

30. J. Simon and M. Greiner, *Condensed-matter physics: A duo of graphene mimics*, *Nature*,483 (7389) (2012), pp. 282-284.

31. J. B. Chahardeh, *A Review on Graphene Transistors*, *International Journal of Advanced Research in Computer and Communication Engineering*,1 (4) (2012).

32. K. S. Novoselov, A. K. Geim, S. V. Morozov, D. Jiang, M. I. Katsnelson, I. V. Grigorieva, S. V. Dubonos and A. A. Firsov, *Two-dimensional gas of massless Dirac fermions in graphene*, *Nature*,438 (7065) (2005), pp. 197-200.

33. S. Pisana, M. Lazzeri, C. Casiraghi, K. S. Novoselov, A. K. Geim, A. C. Ferrari and F. Mauri, *Breakdown of the adiabatic Born-Oppenheimer approximation in graphene*, *Nat Mater*,6 (3) (2007), pp. 198-201.

34. K. Novoselov, A. Geim, S. Morozov, D. Jiang, Y. Zhang, S. Dubonos, I. Grigorieva and A. Firsov, *Electric Field Effect in Atomically Thin Carbon Films*, *Science*,306 (5696) (2004), pp. 666-669.

35. D. Zhang, L. Fu, L. Liao, N. Liu, B. Dai and C. Zhang, *Preparation, characterization, and application of electrochemically functional graphene nanocomposites by one-step liquid-phase exfoliation of natural flake graphite with methylene blue*, *Nano Res.*,5 (12) (2012), pp. 875-887.

36. T. L. Yoon, T. L. Lim, T. K. Min, S. H. Hung, N. Jakse and S. K. Lai, *Epitaxial growth of graphene on 6H-silicon carbide substrate by simulated annealing method*, *The Journal of Chemical Physics*,139 (20) (2013), p. 204702.

37. Y. Yao, Z. Li, Z. Lin, K.-S. Moon, J. Agar and C. Wong, *Controlled Growth of Multilayer, Few-Layer, and Single-Layer Graphene on Metal Substrates*, *The Journal of Physical Chemistry C*,115 (13) (2011), pp. 5232-5238.

38. S. Lizzit, R. Larciprete, P. Lacovig, M. Dalmiglio, F. Orlando, A. Baraldi, L. Gammelgaard, L. Barreto, M. Bianchi, E. Perkins and P. Hofmann, *Transfer-Free Electrical Insulation of Epitaxial Graphene from its Metal Substrate*, *Nano Letters*,12 (9) (2012), pp. 4503-4507.

39. E. Voloshina and Y. Dedkov, *Graphene on metallic surfaces: problems and perspectives*, *Physical Chemistry Chemical Physics*,14 (39) (2012), pp. 13502-13514.

40. Y. Zhang, L. Zhang and C. Zhou, *Review of Chemical Vapor Deposition of Graphene and Related Applications*, *Accounts of Chemical Research*,46 (10) (2013), pp. 2329-2339.

41. A. Dato, V. Radmilovic, Z. Lee, J. Phillips and M. Frenklach, *Substrate-Free Gas-Phase Synthesis of Graphene Sheets*, *Nano Letters*,8 (7) (2008), pp. 2012-2016.

42. Y. Koo, B. Collins, J. Sankar and Y. Yun, *Photocatalyst Nanomaterials for Environmental Challenges and Opportunities*, *Nature*,238 (1972), pp. 37-38.

43. M. F. Hawthorne and D. A. Owen, *Chelated biscarborane transition metal derivatives formed through carbon-metal sigma bonds*, *Journal of the American Chemical Society*,93 (4) (1971), pp. 873-880.

44. J. M. Blakely, J. S. Kim and H. C. Potter, *Segregation of Carbon to the (100) Surface of Nickel*, *Journal of Applied Physics*,41 (6) (1970), pp. 2693-2697.

45. L. B. Ebert, *Intercalation Compounds of Graphite*, *Annual Review of Materials Science*,6 (1) (1976), pp. 181-211.

46. N. I. Kovtyukhova, Y. Wang, A. Berkdemir, R. Cruz-Silva, M. Terrones, V. H. Crespi and T. E. Mallouk, *Non-oxidative intercalation and exfoliation of graphite by Brønsted acids*, *Nat Chem*,advance online publication (2014).

47. H. P. Boehm, R. Setton and E. Stumpp, In *Pure and Applied Chemistry*, (1994), p. 1893.

48. S. V. Morozov, K. S. Novoselov, M. I. Katsnelson, F. Schedin, D. C. Elias, J. A. Jaszczak and A. K. Geim, *Giant Intrinsic Carrier Mobilities in Graphene and Its Bilayer*, *Phys. Rev. Lett.*,100 (1) (2008), p. 016602.

49. R. R. Nair, M. Sepioni, I.-L. Tsai, O. Lehtinen, J. Keinonen, A. V. Krasheninnikov, T. Thomson, A. K. Geim and I. V. Grigorieva, *Spin-half paramagnetism in graphene induced by point defects*, *Nature Physics* 8 (2011), pp. 199-202.

50. R. R. Nair, I.-L. Tsai, M. Sepioni, O. Lehtinen, J. Keinonen, A. V. Krasheninnikov, A. H. C. Neto, M. I. Katsnelson, A. K. Geim and I. V. Grigoriev, *Dual origin of defect magnetism in graphene and its reversible switching by molecular doping*, *Nature Communications*,4 (2013), pp. 1-6.

51. C. Berger, Z. Song, X. Li, X. Wu, N. Brown, C. Naud, D. Mayou, T. Li, J. Hass, A. N. Marchenkov, E. H. Conrad, P. N. First and W. A. de Heer, *Electronic Confinement and Coherence in Patterned Epitaxial Graphene*, *Science*,312 (5777) (2006), pp. 1191-1196.

52. X. Tan, H. Liu, Y. Wen, H. Lv, L. Pan, J. Shi and X. Tang, *Optimizing the thermoelectric performance of zigzag and chiral carbon nanotubes*, *Nanoscale Research Letters*,7 (2012), p. 116.

53. C. Lee, X. Wei, J. W. Kysar and J. Hone, *Measurement of the Elastic Properties and Intrinsic Strength of Monolayer Graphene*, *Science*,321 (5887) (2008), pp. 385-388.

54. J.-H. Chen, C. Jang, S. Xiao, M. Ishigami and M. S. Fuhrer, *Intrinsic and extrinsic performance limits of graphene devices on SiO2*, *Nat Nano*,3 (4) (2008), pp. 206-209.

55. S. Ghosh, W. Bao, D. L. Nika, S. Subrina, E. P. Pokatilov, C. N. Lau and A. A. Balandin, *Dimensional crossover of thermal transport in few-layer graphene*, *Nat Mater*,9 (7) (2010), pp. 555-558.

56. R. Murali, Y. Yang, K. Brenner, T. Beck and J. D. Meindl, *Breakdown current density of graphene nanoribbons*, *Applied Physics Letters*,94 (24) (2009), p. 243114.

57. G. Xu, C. M. Torres, E. B. Song, J. Tang, J. Bai, X. Duan, Y. Zhang and K. L. Wang, *Enhanced Conductance Fluctuation by Quantum Confinement Effect in Graphene Nanoribbons*, *Nano Letters*,10 (11) (2010), pp. 4590-4594.

58. Y.-W. Son, M. L. Cohen and S. G. Louie, *Energy Gaps in Graphene Nanoribbons*, *Physical Review Letters*,97 (21) (2006), p. 216803.

59. X. Jia, J. Campos-Delgado, M. Terrones, V. Meunier and M. S. Dresselhaus, *Graphene edges: a review of their fabrication and characterization*, *Nanoscale*,3 (1) (2011), pp. 86-95.

60. G. Giavaras and F. Nori, *Graphene quantum dots formed by a spatial modulation of the Dirac gap*, *Applied Physics Letters*,97 (24) (2010), p. 243106.

61. F. Guinea, M. I. Katsnelson and A. K. Geim, *Energy gaps and a zero-field quantum Hall effect in graphene by strain engineering*, *Nat Phys*,6 (1) (2010), pp. 30-33.

62. M. T. Allen, J. Martin and A. Yacoby, *Gate-defined quantum confinement in suspended bilayer graphene*, *Nat Commun*,3 (2012), p. 934.

63. D. P. Żebrowski, E. Wach and B. Szafran, *Confined states in quantum dots defined within finite flakes of bilayer graphene: Coupling to the edge, ionization threshold, and valley degeneracy*, *Physical Review B*,88 (16) (2013), p. 165405.

64. Y.-C. Chen, D. G. de Oteyza, Z. Pedramrazi, C. Chen, F. R. Fischer and M. F. Crommie, *Tuning the Band Gap of Graphene Nanoribbons Synthesized from Molecular Precursors, ACS Nano*,7 (7) (2013), pp. 6123-6128.

65. S.-L. Chang, S.-Y. Lin, S.-K. Lin, C.-H. Lee and M.-F. Lin, *Geometric and Electronic Properties of Edge-decorated Graphene Nanoribbons, Sci. Rep.*,4 (2014).

66. A. G. Cano-Márquez, F. J. Rodríguez-Macías, J. Campos-Delgado, C. G. Espinosa-González, F. Tristán-López, D. Ramírez-González, D. A. Cullen, D. J. Smith, M. Terrones and Y. I. Vega-Cantú, *Ex-MWNTs: Graphene Sheets and Ribbons Produced by Lithium Intercalation and Exfoliation of Carbon Nanotubes, Nano Letters*,9 (4) (2009), pp. 1527-1533.

67. K. F. Mak, C. H. Lui, J. Shan and T. F. Heinz, *Observation of an Electric-Field-Induced Band Gap in Bilayer Graphene by Infrared Spectroscopy, Physical Review Letters*,102 (25) (2009), p. 256405.

68. X. Xu, W. Yao, D. Xiao and T. F. Heinz, *Spin and pseudospins in layered transition metal dichalcogenides, Nat Phys*,10 (5) (2014), pp. 343-350.

69. "Massless Dirac Carriers in Graphene" (Max Planck Institute for the Structure and Dynamics of Matter, 2014), http://www.mpsd.mpg.de/mpsd/en/research/cmdd/ohg-ued/research/graphene (Accessed 05/09/2014).

70. W. Bao, F. Miao, Z. Chen, H. Zhang, W. Jang, C. Dames and C. N. Lau, *Controlled ripple texturing of suspended graphene and ultrathin graphite membranes, Nat Nano*,4 (9) (2009), pp. 562-566.

71. D.-H. Cho, L. Wang, J.-S. Kim, G.-H. Lee, E. S. Kim, S. Lee, S. Y. Lee, J. Hone and C. Lee, *Effect of surface morphology on friction of graphene on various substrates, Nanoscale*,5 (7) (2013), pp. 3063-3069.

72. M. Chattopadhyaya, M. M. Alam and S. Chakrabarti, *On the microscopic origin of bending of graphene nanoribbons in the presence of a perpendicular electric field, Physical Chemistry Chemical Physics*,14 (26) (2012), pp. 9439-9443.

73. A. H. Castro Neto, F. Guinea, N. M. R. Peres, K. S. Novoselov and A. K. Geim, *The electronic properties of graphene, Reviews of Modern Physics*,81 (1) (2009), pp. 109-162.

74. T. Ando, *The electronic properties of graphene and carbon nanotubes, NPG Asia Materials*,1 (2009), pp. 17-21.

75. P. Rani and V. K. Jindal, *Designing band gap of graphene by B and N dopant atoms, RSC Advances*,3 (3) (2013), pp. 802-812.

76. P. Preuss, "Surprising Graphene: Honing in on Graphene Electronics with Infrared Synchrotron Radiation" (2008), http://www.lbl.gov/publicinfo/newscenter/pr/2008/ALS-graphene-electrons.html.

77. H. J. Li, W. G. Lu, J. J. Li, X. D. Bai and C. Z. Gu, *Multichannel Ballistic Transport in Multiwall Carbon Nanotubes*, *Physical Review Letters*,95 (8) (2005), p. 086601.

78. J. d. L. Fuenta, "Properties of Graphene" (2013), http://www.graphenea.com/pages/graphene-properties#.UpkBPGSxPnU.

79. X. Li, H. Wang, J. T. Robinson, H. Sanchez, G. Diankov and H. Dai, *Simultaneous Nitrogen-Doping and Reduction of Graphene Oxide Science*,324 (2009), pp. 768-771.

80. T. B. Martins, R. H. Miwa, A. J. R. da Silva and A. Fazzio, *Electronic and Transport Properties of Boron-Doped Graphene Nanoribbons*, *Physical Review Letters*,98 (19) (2007), p. 196803.

81. L. Ci, L. Song, C. Jin, D. Jariwala, D. Wu, Y. Li, A. Srivastava, Z. F. Wang, K. Storr, L. Balicas, F. Liu and P. M. Ajayan, *Atomic layers of hybridized boron nitride and graphene domains*, *Nat Mater*,9 (5) (2010), pp. 430-435.

82. L. S. Panchakarla, K. S. Subrahmanyam, S. K. Saha, A. Govindaraj, H. R. Krishnamurthy, U. V. Waghmare and C. N. R. Rao, *Synthesis, Structure, and Properties of Boron- and Nitrogen-Doped Graphene*, *Advanced Materials*,21 (46) (2009), pp. 4726-4730.

83. S. S. Yu, W. T. Zheng, Q. B. Wen, B. Zheng, H. W. Tian and Q. Jiang, *Nature of Substitutional Impurity Atom B/N in Zigzag Single-Wall Carbon Nanotubes Revealed by First-Principle Calculations*, *IEEE Trans. Nanotechnol.*,5 (5) (2006), pp. 595-598.

84. T. P. Kaloni, Y. C. Cheng, R. Faccio and U. Schwingenschlogl, *Oxidation of monovacancies in graphene by oxygen molecules*, *Journal of Materials Chemistry*,21 (45) (2011), pp. 18284-18288.

85. Y. Fan, M. Zhao, Z. Wang, X. Zhang and H. Zhang, *Tunable electronic structures of graphene/boron nitride heterobilayers*, *Applied Physics Letters*,98 (8) (2011), p. 083103.

86. T. P. Kaloni, Y. C. Cheng and U. Schwingenschlogl, *Electronic structure of superlattices of graphene and hexagonal boron nitride*, *Journal of Materials Chemistry*,22 (3) (2012), pp. 919-922.

87. Y. C. Cheng, T. P. Kaloni, G. S. Huang and U. Schwingenschlögl, *Origin of the high p-doping in F intercalated graphene on SiC*, *Applied Physics Letters*,99 (5) (2011), p. 053117.

88. A. Ramasubramaniam, D. Naveh and E. Towe, *Tunable Band Gaps in Bilayer Graphene−BN Heterostructures*, *Nano Letters*,11 (3) (2011), pp. 1070-1075.

89. X. Wei, M.-S. Wang, Y. Bando and D. Golberg, *Electron-Beam-Induced Substitutional Carbon Doping of Boron Nitride Nanosheets, Nanoribbons, and Nanotubes*, *ACS Nano*,5 (4) (2011), pp. 2916-2922.

90. E. McCann, D. S. Abergel and V. I. Fal'ko, *The low energy electronic band structure of bilayer graphene*, *The European Physical Journal Special Topics*,148 (1) (2007), pp. 91-103.

91. S. Fujii, M. Ziatdinov, M. Ohtsuka, K. Kusakabe, M. Kiguchi and T. Enoki, *Role of edge geometry and chemistry in the electronic properties of graphene nanostructures*, *Faraday Discussions*,(2014).

92. P. Y. Huang, C. S. Ruiz-Vargas, A. M. van der Zande, W. S. Whitney, M. P. Levendorf, J. W. Kevek, S. Garg, J. S. Alden, C. J. Hustedt, Y. Zhu, J. Park, P. L. McEuen and D. A. Muller, *Grains and grain boundaries in single-layer graphene atomic patchwork quilts*, *Nature*,469 (7330) (2011), pp. 389-392.

93. A. Ayuela, W. Jaskólski, H. Santos and L. Chico, *Electronic properties of graphene grain boundaries*, *New J. Phys.*,16 (2014), p. 083018.

94. A. A. Pacheco Sanjuan, Z. Wang, H. P. Imani, M. Vanević and S. Barraza-Lopez, *Graphene's morphology and electronic properties from discrete differential geometry*, *Physical Review B*,89 (12) (2014), p. 121403.

95. K. Chen, X. Wang, J.-B. Xu, L. Pan, X. Wang and Y. Shi, *Electronic Properties of Graphene Altered by Substrate Surface Chemistry and Externally Applied Electric Field*, *The Journal of Physical Chemistry C*,116 (10) (2012), pp. 6259-6267.

96. A. V. Kretinin, Y. Cao, J. S. Tu, G. L. Yu, R. Jalil, K. S. Novoselov, S. J. Haigh, A. Gholinia, A. Mishchenko, M. Lozada, T. Georgiou, C. R. Woods, F. Withers, P. Blake, G. Eda, A. Wirsig, C. Hucho, K. Watanabe, T. Taniguchi, A. K. Geim and R. V. Gorbachev, *Electronic Properties of Graphene Encapsulated with Different Two-Dimensional Atomic Crystals*, *Nano Letters*,14 (6) (2014), pp. 3270-3276.

97. F. Bonaccorso, Z. Sun, T. Hasan and A. C. Ferrari, *Graphene photonics and optoelectronics*, *Nat Photon*,4 (9) (2010), pp. 611-622.

98. F. Xia, T. Mueller, Y.-m. Lin, A. Valdes-Garcia and P. Avouris, *Ultrafast graphene photodetector*, *Nat Nano*,4 (12) (2009), pp. 839-843.

99. F. Wang, Y. Zhang, C. Tian, C. Girit, A. Zettl, M. Crommie and Y. R. Shen, *Gate-Variable Optical Transitions in Graphene*, *Science*,320 (5873) (2008), pp. 206-209.

100. P. Rani, G. S. Dubey and V. K. Jindal, *DFT study of optical properties of pure and doped graphene*, *Physica E: Low-dimensional Systems and Nanostructures*,62 (2014), pp. 28-35.

101. L. A. Falkovsky, *Optical properties of graphene*, *Journal of Physics: Conference Series*,129 (1) (2008), p. 012004.

102. J. L. Cheng, C. Salazar and J. E. Sipe, *Optical properties of functionalized graphene*, *Physical Review B*,88 (4) (2013), p. 045438.

103. T. Eberlein, U. Bangert, R. R. Nair, R. Jones, M. Gass, A. L. Bleloch, K. S. Novoselov, A. Geim and P. R. Briddon, *Plasmon spectroscopy of free-standing graphene films*, *Physical Review B*,77 (23) (2008), p. 233406.

104. A. Marini, C. Hogan, M. Grüning and D. Varsano, *yambo: An ab initio tool for excited state calculations*, *Computer Physics Communications*,180 (8) (2009), pp. 1392-1403.

105. O. V. Sedelnikova, L. G. Bulusheva and A. V. Okotrub, *Ab initio study of dielectric response of rippled graphene*, *The Journal of Chemical Physics*,134 (24) (2011), p. 244707.

106. A. G. Marinopoulos, L. Reining, A. Rubio and V. Olevano, *Ab initio study of the optical absorption and wave-vector-dependent dielectric response of graphite*, *Physical Review B*,69 (24) (2004), p. 245419.

107. A. G. Marinopoulos, L. Wirtz, A. Marini, V. Olevano, A. Rubio and L. Reining, *Optical absorption and electron energy loss spectra of carbon and boron nitride nanotubes: a first-principles approach*, *Applied Physics A*,78 (8) (2004), pp. 1157-1167.

108. M. De Corato, C. Cocchi, D. Prezzi, M. J. Caldas, E. Molinari and A. Ruini, *Optical Properties of Bilayer Graphene Nanoflakes*, *The Journal of Physical Chemistry C*,(2014).

109. A. I. Chernov, P. V. Fedotov, A. V. Talyzin, I. Suarez Lopez, I. V. Anoshkin, A. G. Nasibulin, E. I. Kauppinen and E. D. Obraztsova, *Optical Properties of Graphene Nanoribbons Encapsulated in Single-Walled Carbon Nanotubes*, *ACS Nano*,7 (7) (2013), pp. 6346-6353.

110. T. Hong, Y. Cao, D. Ying and Y.-Q. Xu, *Thermal and optical properties of freestanding flat and stacked single-layer graphene in aqueous media*, *Applied Physics Letters*,104 (22) (2014), pp. -.

111. K. Yang, S. Arezoomandan and B. Sensale-Rodriguez, *The linear and non-linear THz properties of graphene*, *International Journal of Terahertz Science and Technology*,6 (4) (2013), pp. 223-233.

112. S. Wolf and R. N. Tauber, In *Silicon Processing for the VLSI Era, Volume 1 – Process Technology*, ed. S. Wolf and Tauber R. N. (Lattice Press: Sunset Beach, CA, 1986), pp. 36-72.

113. T. Borca-Tascuic, D. A. Achimov and G. Chen, *Difference Between Wafer Temperature and Thermocouple Reading During Rapid Thermal Processing, Mat. Res. Soc. Symp. Proc.* ,525 (1998), pp. 103-108.

114. J. Wagner and F. G. Boebel, *Temperature Measurement at RTP Facilities – An Overview, Mater. Res. Soc. Symp. P.* ,429 (1996), pp. 303-308.

115. S. V. Muley and N. M. Ravindra, *Emissivity of Electronic Materials, Coatings, and Structures, JOM,*(2014), pp. 616-636.

116. N. M. Ravindra, B. Sopori, O. H. Gokce, S. X. Cheng, A. Shenoy, L. Jin, S. Abedrabbo, W. Chen and Y. Zhang, *Emissivity Measurements and Modeling of Silicon-Related Materials: An Overview, International Journal of Thermophysics,*22 (5) (2001), pp. 1593-1611.

117. W. F. Kosonocky, M. B. Kaplinsky, N. J. McCaffrey, E. S. H. Hou, C. N. Manikopoulos, N. M. Ravindra, S. Belikov, J. Li and V. Patel, *Multiwavelength imaging pyrometer, Infrared Detectors and Focal Plane Arrays III, Proc. SPIE,*2225 (1994), pp. 26-43.

118. M. B. Kaplinsky, J. Li, N. J. McCaffrey, V. Patel, E. S. H. Hou, N. M. Ravindra, C. N. Manikopoulos and W. F. Kosonocky, *Recent advances in the development of a multiwavelength imaging pyrometer, Optice,*36 (11) (1997), pp. 3176-3187.

119. Q. Han, T. Gao, R. Zhang, Y. Chen, J. Chen, G. Liu, Y. Zhang, Z. Liu, X. Wu and D. Yu, *Highly sensitive hot electron bolometer based on disordered graphene, Scientific Reports,*3 (3 : 3533) (2013), p. 6.

120. D. Gu, In *Electrical Engineering*, (University of Massachusetts Amherst: Ann Arbor, 2007), p. 174.

121. S. S. Kubakaddi, *Interaction of massless Dirac electrons with acoustic phonons in graphene at low temperatures, Physical Review B,*79 (7) (2009), p. 075417.

122. W. C. Oliver and G. M. Pharr, *Measurement of hardness and elastic modulus by instrumented indentation: Advances in understanding and refinements to methodology, Journal of Materials Research,*19 (01) (2004), pp. 3-20.

123. M. F. Doerner and W. D. Nix, *A method for interpreting the data from depth-sensing indentation instruments, Journal of Materials Research,*1 (04) (1986), pp. 601-609.

124. W. C. Oliver and G. M. Pharr, *An improved technique for determining hardness and elastic modulus using load and displacement sensing indentation experiments, Journal of Materials Research,*7 (06) (1992), pp. 1564-1583.

125. G. Cao, *Atomistic Studies of Mechanical Properties of Graphene*, *Polymers*,6 (9) (2014), pp. 2404-2432.

126. I. W. Frank, D. M. Tanenbaum, A. M. van der Zande and P. L. McEuen, *Mechanical properties of suspended graphene sheets*, *Journal of Vacuum Science & Technology B*,25 (6) (2007), pp. 2558-2561.

127. Y. Zhang and C. Pan, *Measurements of mechanical properties and number of layers of graphene from nano-indentation*, *Diamond and Related Materials*,24 (0) (2012), pp. 1-5.

128. J.-U. Lee, D. Yoon and H. Cheong, *Estimation of Young's Modulus of Graphene by Raman Spectroscopy*, *Nano Letters*,12 (9) (2012), pp. 4444-4448.

129. C. Lee, X. Wei, Q. Li, R. Carpick, J. W. Kysar and J. Hone, *Elastic and frictional properties of graphene*, *physica status solidi (b)*,246 (11-12) (2009), pp. 2562-2567.

130. H. Lee, N. Lee, Y. Seo, J. Eom and S. Lee, *Comparison of frictional forces on graphene and graphite*, *Nanotechnology*,20 (32) (2009), p. 325701 (6 pages).

131. C. Lee, Q. Li, W. Kalb, X.-Z. Liu, H. Berger, R. W. Carpick and J. Hone, *Frictional Characteristics of Atomically Thin Sheets*, *Science*,328 (5974) (2010), pp. 76-80.

132. S. Scharfenberg, D. Z. Rocklin, C. Chialvo, R. L. Weaver, P. M. Goldbart and N. Mason, *Probing the mechanical properties of graphene using a corrugated elastic substrate*, *Applied Physics Letters*,98 (9) (2011), p. 091908.

133. F. Sansoz and T. Gang, *A force-matching method for quantitative hardness measurements by atomic force microscopy with diamond-tipped sapphire cantilevers*, *Ultramicroscopy*,111 (1) (2010), pp. 11-19.

134. F. Liu, P. Ming and J. Li, *Ab initio calculation of ideal strength and phonon instability of graphene under tension*, *Physical Review B*,76 (6) (2007), p. 064120.

135. X. Wei, B. Fragneaud, C. A. Marianetti and J. W. Kysar, *Nonlinear elastic behavior of graphene: Ab initio calculations to continuum description*, *Physical Review B*,80 (20) (2009), p. 205407.

136. M. Smith, (2014), http://edge.rit.edu/. (Accessed 05/11/2014).

137. D. M. Rowe: *Thermoelectrics Handbook: Macro to Nano*. (CRC Press, Taylor & Francis Group, Florida, USA, 2006).

138. T. M. Tritt: *Recent Trends in Thermoelectric Materials Research III*. (Academic Press, 2001).

139. S. Das Sarma, S. Adam, E. H. Hwang and E. Rossi, *Electronic transport in two-dimensional graphene*, *Reviews of Modern Physics*,83 (2) (2011), pp. 407-470.

140. H. Sevinçli and G. Cuniberti, *Enhanced thermoelectric figure of merit in edge-disordered zigzag graphene nanoribbons*, *Physical Review B*,81 (11) (2010), p. 113401.

141. R. D. Barnard: *Thermoelectricity in metals and alloys*. (Taylor & Francis, 1972).

142. F. J. Blatt: *Thermoelectric Power of Metals*. (Plenum Press, 1976).

143. R. Fletcher, *Magnetothermoelectric effects in semiconductor systems*, *Semiconductor Science and Technology*,14 (4) (1999).

144. A. A. Balandin, *Thermal properties of graphene and nanostructured carbon materials*, *Nat Mater*,10 (8) (2011), pp. 569-581.

145. Y. M. Zuev, W. Chang and P. Kim, *Thermoelectric and Magnetothermoelectric Transport Measurements of Graphene*, *Physical Review Letters*,102 (9) (2009), p. 096807.

146. P. Wei, W. Bao, Y. Pu, C. N. Lau and J. Shi, *Anomalous Thermoelectric Transport of Dirac Particles in Graphene*, *Physical Review Letters*,102 (16) (2009), p. 166808.

147. J. G. Checkelsky and N. P. Ong, *Thermopower and Nernst effect in graphene in a magnetic field*, *Physical Review B*,80 (8) (2009), p. 081413.

148. K. S. Novoselov, V. I. Falko, L. Colombo, P. R. Gellert, M. G. Schwab and K. Kim, *A roadmap for graphene*, *Nature*,490 (7419) (2012), pp. 192-200.

149. N. S. Sankeshwar, S. S. Kubakaddi and B. G. Mulimani, In *Advances in Graphene Science*, ed. D. M. Aliofkhazraei (InTech: 2013), pp. 217-271.

150. J. H. Seol, I. Jo, A. L. Moore, L. Lindsay, Z. H. Aitken, M. T. Pettes, X. Li, Z. Yao, R. Huang, D. Broido, N. Mingo, R. S. Ruoff and L. Shi, *Two-Dimensional Phonon Transport in Supported Graphene*, *Science*,328 (5975) (2010), pp. 213-216.

151. X. Liu, D. Wang, P. Wei, L. Zhu and J. Shi, *Effect of carrier mobility on magnetothermoelectric transport properties of graphene*, *Physical Review B*,86 (15) (2012), p. 155414.

152. X. Wu, Y. Hu, M. Ruan, N. K. Madiomanana, C. Berger and W. A. de Heer, *Thermoelectric effect in high mobility single layer epitaxial graphene*, *Applied Physics Letters*,99 (13) (2011), p. 133102.

153. E. H. Hwang, E. Rossi and S. Das Sarma, *Theory of thermopower in two-dimensional graphene*, *Physical Review B*,80 (23) (2009), p. 235415.

154. F. Ghahari, Y. Zuev, K. Watanabe, T. Taniguchi and P. Kim, *Effect of electron-electron interactions in thermoelectric power in graphene*, *Bull. American Phys Soc*,57 (1) (2012).

155. F. Bonaccorso, A. Lombardo, T. Hasan, Z. Sun, L. Colombo and A. C. Ferrari, *Production and processing of graphene and 2d crystals*, *Materials Today*,15 (12) (2012), pp. 564-589.

156. A. V. Babichev, V. E. Gasumyants and V. Y. Butko, *Resistivity and thermopower of graphene made by chemical vapor deposition technique*, *Journal of Applied Physics*,113 (7) (2013), p. 076101.

157. A. N. Sidorov, A. Sherehiy, R. Jayasinghe, R. Stallard, D. K. Benjamin, Q. Yu, Z. Liu, W. Wu, H. Cao, Y. P. Chen, Z. Jiang and G. U. Sumanasekera, *Thermoelectric power of graphene as surface charge doping indicator*, *Applied Physics Letters*,99 (1) (2011), p. 013115.

158. S.-G. Nam, D.-K. Ki and H.-J. Lee, *Thermoelectric transport of massive Dirac fermions in bilayer graphene*, *Physical Review B*,82 (24) (2010), p. 245416.

159. F. Mazzamuto, V. Hung Nguyen, Y. Apertet, C. Caër, C. Chassat, J. Saint-Martin and P. Dollfus, *Enhanced thermoelectric properties in graphene nanoribbons by resonant tunneling of electrons*, *Physical Review B*,83 (23) (2011), p. 235426.

160. Y. Chen, T. Jayasekera, A. Calzolari, K. W. Kim and M. B. Nardelli, *Thermoelectric properties of graphene nanoribbons, junctions and superlattices*, *Journal of physics. Condensed matter : an Institute of Physics journal*,22 (37) (2010), p. 372202.

161. J. Morgan Iii, In *Springer Handbook of Atomic, Molecular, and Optical Physics*, ed. G. Drake (Springer New York: 2006), pp. 295-306.

162. H. Adachi, T. Mukoyama and J. Kawai: *Hartree-Fock-Slater Method for Materials Science: The DV-X Alpha Method for Design and Characterization of Materials*. (Springer, 2006).

163. P. M. Dinh: *Condensed Matter Theories*. (Nova Science Publishers, 2005).

164. P. Hohenberg and W. Kohn, *Inhomogeneous Electron Gas*, *Physical Review*,136 (3B) (1964), pp. B864-B871.

165. S. Kotochigova, Z. H. Levine, E. L. Shirley, M. D. Stiles and C. W. Clark, (NIST: Physical Measurement Laboratory, NIST, 2014).

166. W. Kohn and L. J. Sham, *Self-Consistent Equations Including Exchange and Correlation Effects*, *Physical Review*,140 (4A) (1965), pp. A1133-A1138.

167. S. Narasimhan, *"The Self Consistent Field "(SCF) loop and some Relevant Parameters for Quantum -ESPRESSO*, 2221 (5) (2011).

168. J. P. Perdew and A. Zunger, *Self-interaction correction to density-functional approximations for many-electron systems*, *Physical Review B*,23 (10) (1981), pp. 5048-5079.

169. G. B. Bachelet, D. R. Hamann and M. Schlüter, *Pseudopotentials that work: From H to Pu*, *Physical Review B*,26 (8) (1982), pp. 4199-4228.

170. N. M. Ravindra, K. Ravindra, S. Mahendra, B. Sopori and A. T. Fiory, *Modeling and Simulation of Emissivity of Silicon-Related Materials and Structures*, *J. Electron. Mater.*,32 (10) (2003), pp. 1052-1058.

171. E. D. Palik, ed. E. D. Palik (Academic Press, Waltham: MA, 1998), pp. 275-798.

172. A. M. Zaitsev, In *Optical Properties of Diamond: A Data Handbook*, ed. A. M. Zaitsev (Springer: Berlin, Heidelberg, 2001), pp. 1-9.

173. J. W. Weber, V. E. Calado and M. C. M. van de Sanden, *Optical constants of graphene measured by spectroscopic ellipsometry*, *Appl. Phys. Lett.*,97 (9) (2010), p. 091904 (4 pages).

174. J. P. Hebb and K. F. Jensen, *Journal of Electrochemical Society*,143 (3) (1996), pp. 1142-1151.

175. M. P. Allen and D. J. Tildesley: *Computer Simulation of Liquids*. (Clarendon Press, Oxford, 1987).

176. J. M. Haile: *Molecular Dynamics Simulation: Elementary Methods*. (John Wiley & Sons, Inc., Clemson, USA, 1992).

177. W. Greiner, L. Neise and H. Stöcker: *Thermodynamics and Statistical Mechanics*. (Springer New York, New York, 1995).

178. S. Plimpton, *Fast parallel algorithms for short-range molecular dynamics*, *Journal of Computational Physics*,117 (1) (1995), pp. 1-19.

179. W. C. Swope, H. C. Andersen, P. H. Berens and K. R. Wilson, *A computer simulation method for the calculation of equilibrium constants for the formation of physical clusters of molecules: Application to small water clusters*, *The Journal of Chemical Physics*,76 (1) (1982), pp. 637-649.

180. H. C. Andersen, *Molecular dynamics simulations at constant pressure and/or temperature*, *The Journal of Chemical Physics*,72 (4) (1980), pp. 2384-2393.

181. D. L. Nika, E. P. Pokatilov, A. S. Askerov and A. A. Balandin, *Phonon thermal conduction in graphene: Role of Umklapp and edge roughness scattering*, *Physical Review B*,79 (15) (2009), p. 155413.

182. J. Lan, J.-S. Wang, C. K. Gan and S. K. Chin, *Edge effects on quantum thermal transport in graphene nanoribbons: Tight-binding calculations*, *Physical Review B*,79 (11) (2009), p. 115401.

183. A. A. Balandin, S. Ghosh, W. Bao, I. Calizo, D. Teweldebrhan, F. Miao and C. N. Lau, *Superior Thermal Conductivity of Single-Layer Graphene*, *Nano Letters*,8 (3) (2008), pp. 902-907.

184. F. Müller-Plathe, *A simple nonequilibrium molecular dynamics method for calculating the thermal conductivity*, *The Journal of Chemical Physics*,106 (14) (1997), pp. 6082-6085.

185. D. D. Koelling and J. H. Wood, *On the interpolation of eigenvalues and a resultant integration scheme*, *J. Comput. Phys.*,67 (2) (1986), pp. 253-262.

186. G. K. Madsen and D. J. Singh, *BoltzTraP. A code for calculating band-structure dependent quantities*, *Computer Physics Communications*,175 (1) (2006), pp. 67-71.

187. W. Humphrey, A. Dalke and K. Schulten, *VMD - Visual Molecular Dynamics*, *J. Molec. Graphics*,14.1 (1996), pp. 33-38.

188. Q. Kan, W. Yan, G. Kang and Q. Sun, *Oliver–Pharr indentation method in determining elastic moduli of shape memory alloys—A phase transformable material*, *Journal of the Mechanics and Physics of Solids*,61 (10) (2013), pp. 2015-2033.

189. R. B. King, *Elastic analysis of some punch problems for a layered medium*, *Internation Journal of Solid Structures*,23 (12) (1987), pp. 1657-1664.

190. W. Wang, S. Li, J. Min, C. Yi, Y. Zhan and M. Li, *Nanoindentation experiments for single-layer rectangular graphene films: a molecular dynamics study*, *Nanoscale Res Lett*,9 (41) (2014), pp. 1-8.

191. S. P. Kiselev and E. V. Zhirov, *Molecular dynamics simulation of deformation and fracture of graphene under uniaxial tension*, *Phys Mesomech*,16 (2) (2013), pp. 125-132.

192. H. Zhao, K. Min and N. R. Aluru, *Size and Chirality Dependent Elastic Properties of Graphene Nanoribbons under Uniaxial Tension*, *Nano Letters*,9 (8) (2009), pp. 3012-3015.

193. A. Carpio and L. L. Bonilla, *Periodized discrete elasticity models for defects in graphene*, *Physical Review B*,78 (8) (2008), p. 085406.

194. S. Ghosh, I. Calizo, D. Teweldebrhan, E. P. Pokatilov, D. L. Nika, A. A. Balandin, W. Bao, F. Miao and C. N. Lau, *Extremely high thermal conductivity of graphene: Prospects for thermal management applications in nanoelectronic circuits*, *Applied Physics Letters*,92 (15) (2008), p. 151911.

195. J. Hu, X. Ruan, Z. Jiang and Y. P. Chen, In *AIP Conf. Proc. No. 1173*, (AIP, New York, 2009), p. 135.

196. X. Xu, L. F. C. Pereira, Y. Wang, J. Wu, K. Zhang, X. Zhao, S. Bae, C. Tinh Bui, R. Xie, J. T. L. Thong, B. H. Hong, K. P. Loh, D. Donadio, B. Li and B. Özyilmaz, *Length-dependent thermal conductivity in suspended single-layer graphene*, *Nat Commun*,5 (2014).

197. T. Yamamoto, K. Watanabe and K. Mii, *Empirical-potential study of phonon transport in graphitic ribbons*, *Physical Review B*,70 (24) (2004), p. 245402.

198. N. Yang, G. Zhang and B. Li, *Thermal rectification in asymmetric graphene ribbons*, *Applied Physics Letters*,95 (3) (2009), p. 033107.

199. B. Mortazavi, A. Rajabpour, S. Ahzi, Y. Rémond and S. Mehdi Vaez Allaei, *Nitrogen doping and curvature effects on thermal conductivity of graphene: A non-equilibrium molecular dynamics study*, *Solid State Communications*,152 (4) (2012), pp. 261-264.

200. J. C. Carrero-Sánchez, A. L. Elías, R. Mancilla, G. Arrellín, H. Terrones, J. P. Laclette and M. Terrones, *Biocompatibility and toxicological studies of carbon nanotubes doped with nitrogen*, *Nano Letters*,6 (8) (2006), pp. 1609-1616.

201. H. Zhang, G. Lee and K. Cho, *Thermal transport in graphene and effects of vacancy defects*, *Physical Review B*,84 (11) (2011), p. 115460.

202. P. G. Klemens and D. F. Pedraza, *Thermal conductivity of graphite in the basal plane*, *Carbon*,32 (4) (1994), pp. 735-741.

203. S. Subrina and D. Kotchetkov, *Simulation of Heat Conduction in Suspended Graphene Flakes of Variable Shapes*, *Journal of Nanoelectronics and Optoelectronics*,3 (2008), pp. 1-21.

204. D. A. Areshkin, D. Gunlycke and C. T. White, *Ballistic Transport in Graphene Nanostrips in the Presence of Disorder: Importance of Edge Effects*, *Nano Letters*,7 (1) (2006), pp. 204-210.

205. Y. Ouyang and J. Guo, *A theoretical study on thermoelectric properties of graphene nanoribbons*, *Applied Physics Letters*,94 (26) (2009), p. 093104.

206. H. Karamitaheri, N. Neophytou, M. Pourfath, R. Faez and H. Kosina, *Engineering enhanced thermoelectric properties in zigzag graphene nanoribbons*, *Journal of Applied Physics*,111 (5) (2012), p. 093104.

207. H. Mousavi and R. Moradian, *Nitrogen and boron doping effects on the electrical conductivity of graphene and nanotube*, *Solid State Sciences*,13 (8) (2011), pp. 1459-1464.

208. D. Bahamon, A. Pereira and P. Schulz, *Third Edge for a Graphene Nanoribbon: A Tight-Binding Model Calculation*, *Phys. Rev. B*,83 (7) (2011).

209. L. D. Carr and M. T. Lusk, *Defect engineering: Graphene gets designer defects*, *Nat Nano*,5 (5) (2010), pp. 316-317.

210. P. Avouris, *Graphene: Electronic and Photonic Properties and Devices*, *Nano Letters,*10 (11) (2010), pp. 4285-4294.

211. Y. Jun, H. Kimm, J. A. Elle, B. Sushkova, G. S. Jenkins, H. Milchberg, M. S. Fuhrer and H. D. Drew, *Dual-gated bilayer graphene hot-electron bolometer*, *Nat. Nanotechnol.,*7 (7) (2012), pp. 472-478.

212. "Resistivity, Conductivity and Temperature Coefficients for some Common Materials" (The Engineering ToolBox, 2014), http://www.engineeringtoolbox.com/ (Accessed 01/06/2014).

213. M. Wang, S. K. Jang, W.-J. Jang, M. Kim, S.-Y. Park, S.-W. Kim, S.-J. Kahng, J.-Y. Choi, R. S. Ruoff, Y. J. Song and S. Lee, *A Platform for Large-Scale Graphene Electronics – CVD Growth of Single-Layer Graphene on CVD-Grown Hexagonal Boron Nitride*, *Adv. Mater.,*25 (19) (2013), pp. 2746-2752.

214. G. Kresse and J. Furthmüller, *Efficient iterative schemes for ab initio total energy calculations using a plane-wave basis set*, *Physical Review B,*54 (16) (1996), pp. 11169-11186.

215. J. P. Perdew, K. Burke and M. Ernzerhof, *Generalized Gradient Approximation Made Simple*, *Physical Review Letters,*77 (18) (1996), pp. 3865-3868.

216. E. McCann, D. S. L. Abergel and V. I. Fal'ko, *Electrons in bilayer graphene*, *Solid State Communications,*143 (1–2) (2007), pp. 110-115.

217. V. G. Kravets, A. N. Grigorenko, R. R. Nair, P. Blake, S. Anissimova, K. S. Novoselov and A. K. Geim, *Spectroscopic ellipsometry of graphene and an exciton-shifted van Hove peak in absorption*, *Physical Review B,*81 (15) (2010), p. 155413.

218. L. Yang, J. Deslippe, C.-H. Park, M. L. Cohen and S. G. Louie, *Excitonic Effects on the Optical Response of Graphene and Bilayer Graphene*, *Physical Review Letters,*103 (18) (2009), p. 186802.

219. L. Wu, H. S. Chu, W. S. Koh and E. P. Li, *Highly sensitive graphene biosensors based on surface plasmon resonance*, *Opt. Express,*18 (14) (2010), pp. 14395-14400.

220. G. Neuer, In *Quantitative Infrared Thermography (QIRT) 92*, ed. EETI (QIRT Archives: Paris, 1992).

221. A. Zandiatashbar, G.-H. Lee, S. J. An, S. Lee, N. Mathew, M. Terrones, T. Hayashi, C. R. Picu, J. Hone and N. Koratkar, *Effect of defects on the intrinsic strength and stiffness of graphene*, *Nat Commun,*5 (2014).

222. J. Chen, G. Zhang and B. Li, *Substrate coupling suppresses size dependence of thermal conductivity in supported graphene*, *Nanoscale,*5 (2) (2013), pp. 532-536.

223. W.-R. Zhong, M.-P. Zhang, B.-Q. Ai and D.-Q. Zheng, *Chirality and thickness-dependent thermal conductivity of few-layer graphene: A molecular dynamics study, Applied Physics Letters,*98 (11) (2011), p. 113107.

224. Z. Guo, D. Zhang and X.-G. Gong, *Thermal conductivity of graphene nanoribbons, Applied Physics Letters,*95 (16) (2009), p. 163103.

225. B. Mortazavi and S. Ahzi, *Molecular dynamics study on the thermal conductivity and mechanical properties of boron doped graphene, Solid State Communications,*152 (15) (2012), pp. 1503-1507.

226. H. Zheng, H. J. Liu, X. J. Tan, H. Y. Lv, L. Pan, J. Shi and X. F. Tang, *Enhanced thermoelectric performance of graphene nanoribbons, Applied Physics Letters,*100 (9) (2012), p. 093104.

227. J. Lahiri, Y. Lin, P. Bozkurt, I. I. Oleynik and M. Batzill, *An extended defect in graphene as a metallic wire, Nat Nano,*5 (5) (2010), pp. 326-329.